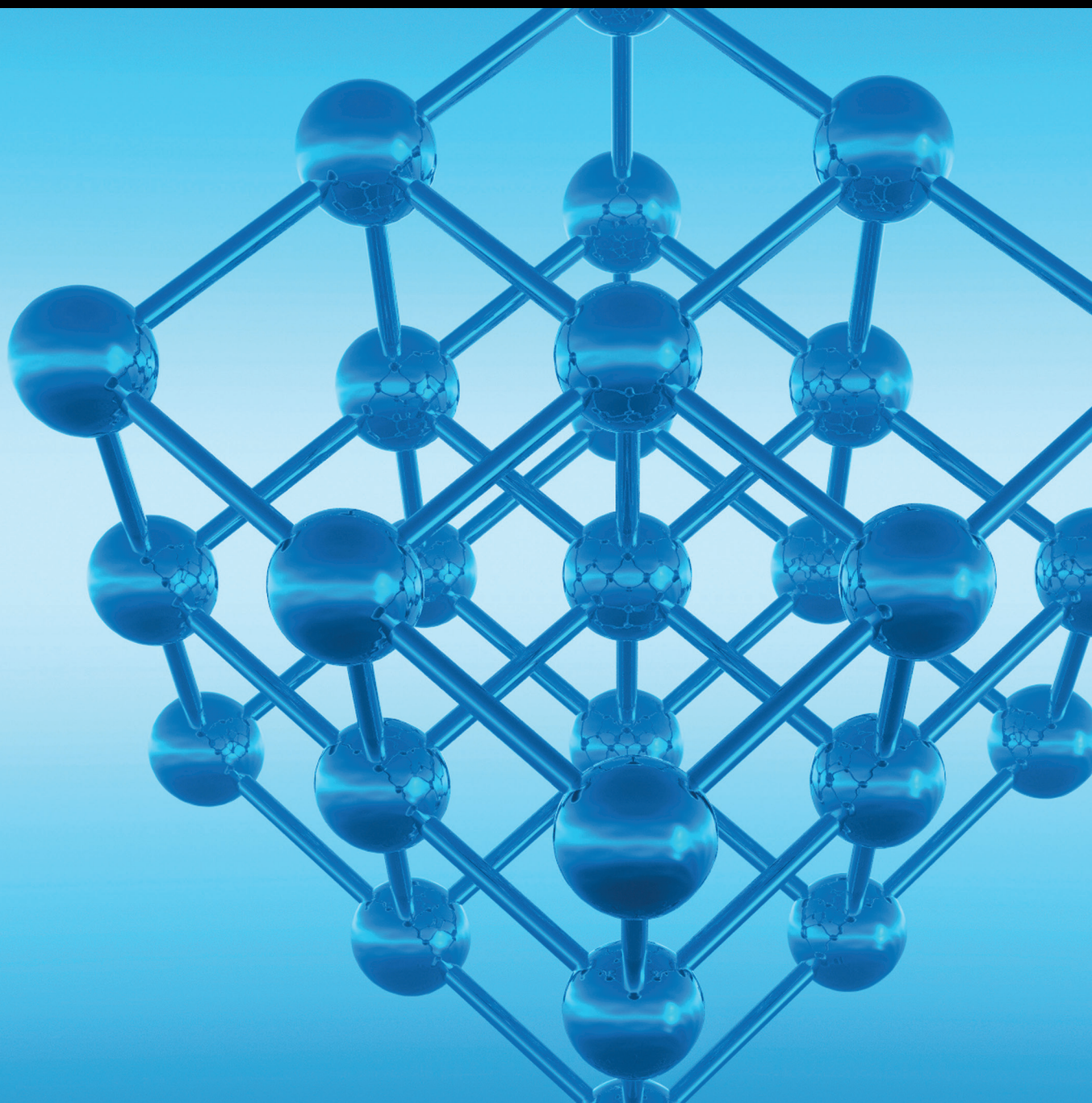


Advances in Condensed Matter Physics

Spin Transport and Magnetism in Low-Dimensional Materials

Guest Editors: Xiaohong Xu, Jingsheng Chen, Gillian A. Gehring, Xiangshui Miao, and Hao Zeng





Spin Transport and Magnetism in Low-Dimensional Materials

Advances in Condensed Matter Physics

Spin Transport and Magnetism in Low-Dimensional Materials

Guest Editors: Xiaohong Xu, Jingsheng Chen, Gillian A. Gehring,
Xiangshui Miao, and Hao Zeng



Copyright © 2017 Hindawi Publishing Corporation. All rights reserved.

This is a special issue published in “Advances in Condensed Matter Physics.” All articles are open access articles distributed under the Creative Commons Attribution License, which permits unrestricted use, distribution, and reproduction in any medium, provided the original work is properly cited.

Editorial Board

Dario Alfe, UK
Bohdan Andraka, USA
Daniel Arovas, USA
Veer P. S. Awana, India
Arun Bansil, USA
Ward Beyermann, USA
Golam M. Bhuiyan, Bangladesh
Rudro R. Biswas, USA
Luis L. Bonilla, Spain
Gang Cao, USA
Ashok Chatterjee, India
Ram N. P. Choudhary, India
Kim Chow, Canada
Oleg Derzhko, Ukraine
Hiromi Kitahara Eba, Japan

Gayanath Fernando, USA
Jörg Fink, Germany
Yuri Galperin, Norway
Russell Giannetta, USA
James L. Gole, USA
Prasenjit Guptasarma, USA
Da-Ren Hang, Taiwan
Yurij Holovatch, Ukraine
Chia-Ren Hu, USA
David Huber, USA
Jan A. Jung, Canada
Feo V. Kusmartsev, UK
Rosa Lukaszew, USA
Vladimir A. Osipov, Russia
Rolfe Petschek, USA

Joseph S. Poon, USA
Leonid Pryadko, USA
Charles Rosenblatt, USA
Omid Saremi, Canada
Mohindar S. Seehra, USA
Sergei Sergeenkov, Brazil
Daniel L. Stein, USA
Michael C. Tringides, USA
Sergio E. Ulloa, USA
Attila Virosztek, Hungary
Markus R. Wagner, Germany
Gary Wysin, USA
Kiyokazu Yasuda, Japan
Fajun Zhang, Germany

Contents

Spin Transport and Magnetism in Low-Dimensional Materials

Xiaohong Xu, Jingsheng Chen, Gillian A. Gehring, Xiangshui Miao, and Hao Zeng
Volume 2017, Article ID 6568979, 2 pages

Magnetoresistance Effect in NiFe/BP/NiFe Vertical Spin Valve Devices

Leilei Xu, Jiafeng Feng, Kangkang Zhao, Weiming Lv, Xiufeng Han, Zhongyuan Liu, Xiaohong Xu, He Huang, and Zhongming Zeng
Volume 2017, Article ID 9042823, 6 pages

Microstructure and Magnetic Properties of NdFeB Films through Nd Surface Diffusion Process

Wenfeng Liu, Mingang Zhang, Kewei Zhang, and Yuesheng Chai
Volume 2017, Article ID 4296243, 5 pages

Perpendicular Giant Magnetoresistance and Magnetic Properties of Co/Cu Nanowire Arrays Affected by Period Number and Copper Layer Thickness

Juan Han, Xiufang Qin, Zhiyong Quan, Lanfang Wang, and Xiaohong Xu
Volume 2016, Article ID 9019806, 9 pages

Ultrasensitive Anomalous Hall Effect in Ta/CoFe/Oxide/Ta Multilayers

Guang Yang, Yongye Li, Xi Chen, Jingyan Zhang, and Guanghua Yu
Volume 2016, Article ID 9734610, 7 pages

High Field Linear Magnetoresistance Sensors with Perpendicular Anisotropy LI_0 -FePt Reference Layer

X. Liu, Z. L. Song, R. Wang, and Z. Y. Quan
Volume 2016, Article ID 8528617, 6 pages

Micromagnetic Simulation of Strain-Assisted Current-Induced Magnetization Switching

H. B. Huang, C. P. Zhao, and X. Q. Ma
Volume 2016, Article ID 9271407, 6 pages

Editorial

Spin Transport and Magnetism in Low-Dimensional Materials

Xiaohong Xu,^{1,2} Jingsheng Chen,³ Gillian A. Gehring,⁴ Xiangshui Miao,⁵ and Hao Zeng⁶

¹Key Laboratory of Magnetic Molecules and Magnetic Information Materials of Ministry of Education and School of Chemistry and Materials Science, Shanxi Normal University, Linfen 041004, China

²Research Institute of Materials Science, Shanxi Normal University, Linfen 041004, China

³Department of Materials Science and Engineering, National University of Singapore, Singapore 117576

⁴Department of Physics and Astronomy, University of Sheffield, Sheffield S3 7RH, UK

⁵School of Optical and Electronic Information, Huazhong University of Science and Technology, Wuhan 430074, China

⁶Department of Physics, University at Buffalo, State University of New York, Buffalo, NY 14260, USA

Correspondence should be addressed to Xiaohong Xu; xuxh@sxnu.edu.cn

Received 22 January 2017; Accepted 23 January 2017; Published 28 February 2017

Copyright © 2017 Xiaohong Xu et al. This is an open access article distributed under the Creative Commons Attribution License, which permits unrestricted use, distribution, and reproduction in any medium, provided the original work is properly cited.

Spin generation, manipulation, and detection in low-dimensional materials have entered a dynamic new phase. The continued miniaturization of magnetic storage and the integration of magnetic devices into current IC chip present new challenges for materials and device scientists, which require continued innovation in material structures as well as in device and system concepts for spin-dependent transport and magnetism. Recent advances in this field include the magnetoresistance effect, diluted magnetic semiconductors, Hall effect, field-free magnetization switching, improved hard magnetic materials, and the exploration of low-dimensional materials with controlled spin states.

The purpose of this special issue is to shed light on some of the current works being done on novel synthesis methods and the physical phenomena occurring in nanoscale magnetic materials that will be used in next-generation spintronic devices. Among the submissions, six papers were selected for publication in this special issue. The theoretical paper by H. B. Huang et al. reported the strain-assisted spin transfer torque (STT) induced magnetization switching in CoFeB-based magnetic tunnel junctions by combining phase-field method with micromagnetic simulations. This work indicates a new aspect of free field magnetization switching and compares it to the previously reported methods such as spin orbital torque combined with exchange bias and broken lateral inversion symmetry. G. Yang et al. reported the ultrasensitive anomalous Hall effect (AHE) in Ta/CoFe/oxide (MgO and HfO₂)/Ta multilayers and discussed the effect

of the annealing process on sensitivity. AHE sensitivity as high as 18792 Ω/T in the as-deposited Ta/CoFe/MgO/Ta was obtained. This work gives a new insight that both the selection of the oxide material and the postannealing treatment play an important role in determining the sensitivity of AHE. The microstructure and magnetic properties of NdFeB films through Nd surface diffusion process were investigated by W. Liu et al., showing that the microstructure and magnetic properties of Ta/Nd/NdFeB/Nd/Ta films are strongly dependent on the NdFeB layer thickness.

The other three papers focused on the magnetoresistance effect of the multilayers and nanowire arrays. X. Liu et al. reported linear magnetoresistance in L1₀-FePt/ZnO/Fe multilayers, in which linear response is observed in a large range from +5 kOe to -5 kOe. This type of linear magnetoresistance is significant for high field linear magnetic sensors. L. Xu et al. reported the magnetoresistance properties of black phosphorus (BP) spin-valve devices consisting of thin BP flakes contacted by NiFe ferromagnetic electrodes. The devices show spin-valve effect from room temperature to low temperature with magnetoresistance of 0.57% at 4 K. Highly ordered arrays of Co/Cu multilayered nanowires were investigated by J. Han et al. using porous anodic alumina (PAA) templates. They discussed the effects of repeat period number and the thickness of the copper layer on the magnetic and magnetoresistance. The editors are sure that this group of papers will be a useful reference for future workers seeking further developments of magnetic nanodevices.

Acknowledgments

We would like to thank all the authors and coauthors who submitted their papers to the special issue. We hope that the publications of this special issue will be of reference value for readers.

Xiaohong Xu
Jingsheng Chen
Gillian A. Gehring
Xiangshui Miao
Hao Zeng

Research Article

Magnetoresistance Effect in NiFe/BP/NiFe Vertical Spin Valve Devices

Leilei Xu,^{1,2} Jiafeng Feng,³ Kangkang Zhao,² Weiming Lv,⁴ Xiufeng Han,³ Zhongyuan Liu,⁴ Xiaohong Xu,¹ He Huang,² and Zhongming Zeng²

¹School of Chemistry and Materials Science, Key Laboratory of Magnetic Molecules and Magnetic Information Materials, Ministry of Education, Shanxi Normal University, Linfen 41004, China

²Key Laboratory of Nanodevices and Applications, Suzhou Institute of Nano-Tech and Nano-Bionics, Chinese Academy of Sciences, Ruoshui Road 398, Suzhou 215123, China

³Beijing National Laboratory for Condensed Matter Physics, Institute of Physics, Chinese Academy of Sciences, Beijing 100190, China

⁴State Key Laboratory of Metastable Materials Science and Technology, Yanshan University, Qinhuangdao 066004, China

Correspondence should be addressed to Xiaohong Xu; xuxiaohong_ly@163.com and Zhongming Zeng; zmzeng2012@sinano.ac.cn

Received 6 October 2016; Accepted 4 December 2016; Published 26 February 2017

Academic Editor: Veer P. S. Awana

Copyright © 2017 Leilei Xu et al. This is an open access article distributed under the Creative Commons Attribution License, which permits unrestricted use, distribution, and reproduction in any medium, provided the original work is properly cited.

Two-dimensional (2D) layered materials such as graphene and transition metal dichalcogenides are emerging candidates for spintronic applications. Here, we report magnetoresistance (MR) properties of a black phosphorus (BP) spin valve devices consisting of thin BP flakes contacted by NiFe ferromagnetic (FM) electrodes. The spin valve effect has been observed from room temperature to 4 K, with MR magnitudes of 0.57% at 4 K and 0.23% at 300 K. In addition, the spin valve resistance is found to decrease monotonically as temperature is decreased, indicating that the BP thin film works as a conductive interlayer between the NiFe electrodes.

1. Introduction

Two-dimensional (2D) nanomaterials such as single-layer graphene and transition metal dichalcogenides (TMDs) have attracted great attention as building blocks for future (opto)electronic technologies due to their specific layered structures and novel physical properties [1–3]. Recently, the 2D nanomaterials have also been demonstrated to have potential for application in the field of spintronics [4–11]. The 2D materials have been largely researched as nonmagnetic interlayer of spin valve, which is similar to traditional magnetic tunneling junctions consisting of two ferromagnetic (FM) layers separated by a nonmagnetic insulating spacer, usually Al_2O_3 and MgO , and the resistance depends on the magnetization orientation of two ferromagnetic electrodes [12, 13]. The first experimental work for realization of spin-transport phenomenon is reported by Tombros et al. in graphene-based planar spin valve structure [4]. Later on, magnetoresistance (MR) was measured at room temperature in graphene vertical spin valve [7, 8]. Subsequent works

reported spin-dependent transport in h-BN and transition metal dichalcogenides (TMDs), such as MoS_2 and WS_2 [9–11]. These studies suggest that the 2D nanomaterials may be promising for spintronic applications. Recently, a few-layer black phosphorus (BP), a newly identified 2D nanomaterial, has been demonstrated to be an appealing candidate material owing to its exotic physical properties such as thickness-dependent tunable band gap and high carrier mobility [14–18]. Interestingly, theoretical study predicted a relatively large MR ratio in the BP-based spin valve structure [19–21]. However, so far, there have been no reports of MR effect in BP-based spin valve.

In this work, we report on the fabrication and spin valve effect in the BP-based device. 2D BP is sandwiched by two permalloy electrodes (Py and $\text{Ni}_{81}\text{Fe}_{19}$) and the BP layer serves as nonmagnetic spacer layer as shown in Figure 1(a). The devices show spin valve effect from room temperature to low temperature with a MR of 0.57% at 4 K. The temperature dependence of the device resistance reveals that the BP layer works as a metallic layer between two FM electrodes.

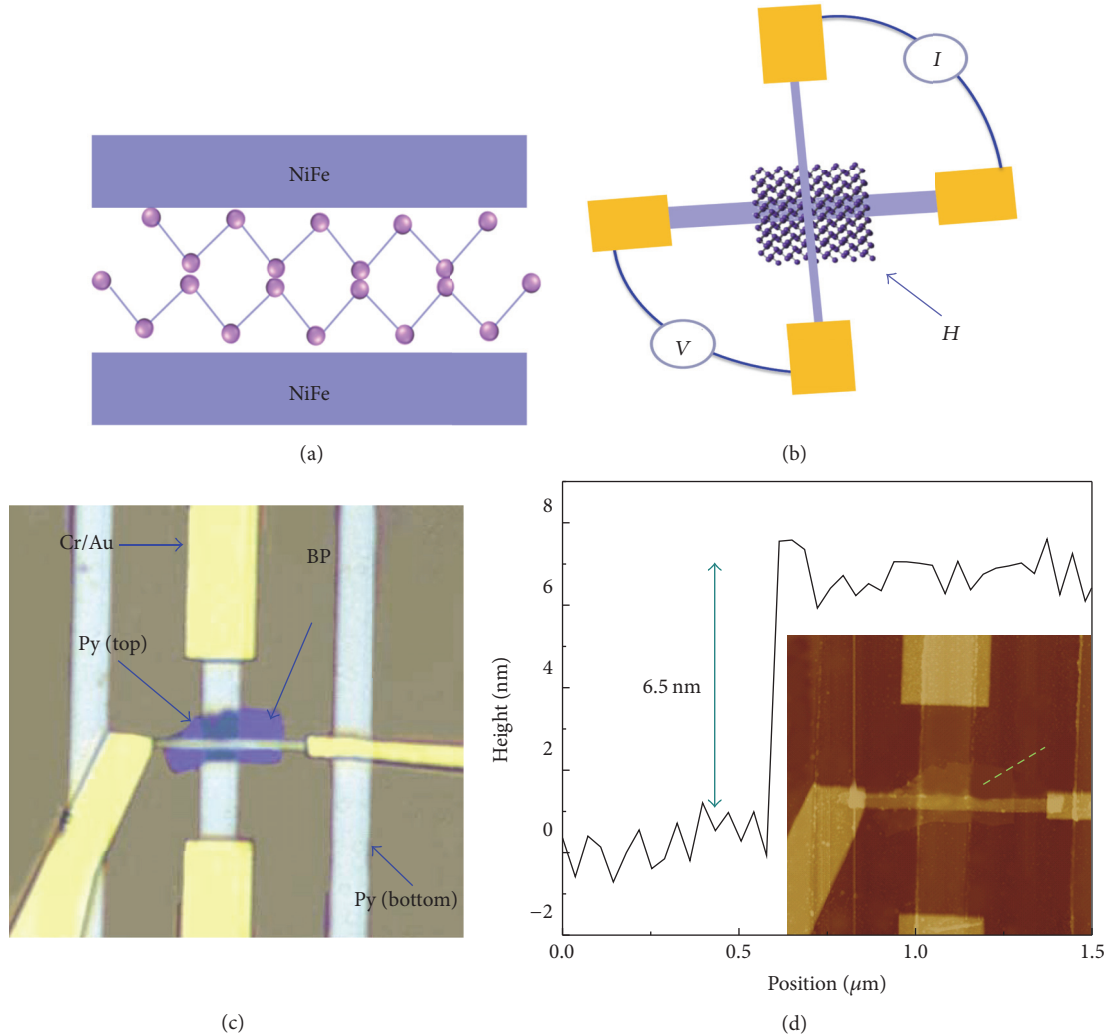


FIGURE 1: ((a) and (b)) Structure and measurement structure of BP-based vertical spin valve device, consisting of bottom NiFe electrode, 2D-BP spacer, and top NiFe electrode. (c) Optical micrograph of NiFe/BP/NiFe spin valve device. (d) AFM graph of device.

2. Methods

2.1. Material and Device Fabrication. The BP crystals were synthesized from red phosphorus under high temperature of 1000°C and high pressure of 2 GPa. Thin BP flake was obtained by mechanically exfoliating BP crystal using adhesive tape (scotch tape), and then the flake was transferred onto the prepatterned Py (bottom) electrodes on SiO_2/Si substrate. The bottom electrodes were fabricated by e-beam lithography (EBL) and a lift-off procedure after e-beam evaporating Py with thickness of ~ 30 nm. In the subsequent process, top Py electrodes with thickness of ~ 50 nm were fabricated by another run of EBL, metal deposition and lift-off process. Finally, the bottom and top FM electrodes were connected with large electrodes by EBL and Cr (5 nm)/Au (60 nm) deposition.

2.2. Device Characterization and Measurement Setup. The devices were measured with a four-terminal setup, where the

bias currents flow perpendicular to the device plane of the spin valve. The magnetic field was applied in-plane at 45° to the direction of the Py ferromagnetic electrodes as shown in Figure 1(b). The BP flake was initially identified by optical microscopy in Figure 1(c) and then further confirmed by atomic force microscopy (AFM). Figure 1(d) shows an atomic force microscope (AFM) image of one device, revealing that the thickness of BP for the device is ~ 6.5 nm. The transport measurements for the BP-based spin valve devices were performed using Physical Properties Measurements System (PPMS) made by Quantum Design.

3. Results and Discussion

3.1. Current-Voltage Characteristics and Spin Valve Effect. Figure 2(a) displays the current-voltage (I - V) curves of one typical device for various temperatures. The linear I - V curves indicate the Ohmic contact characteristics of the BP flake and FM electrodes. At room temperature, the resistance-area

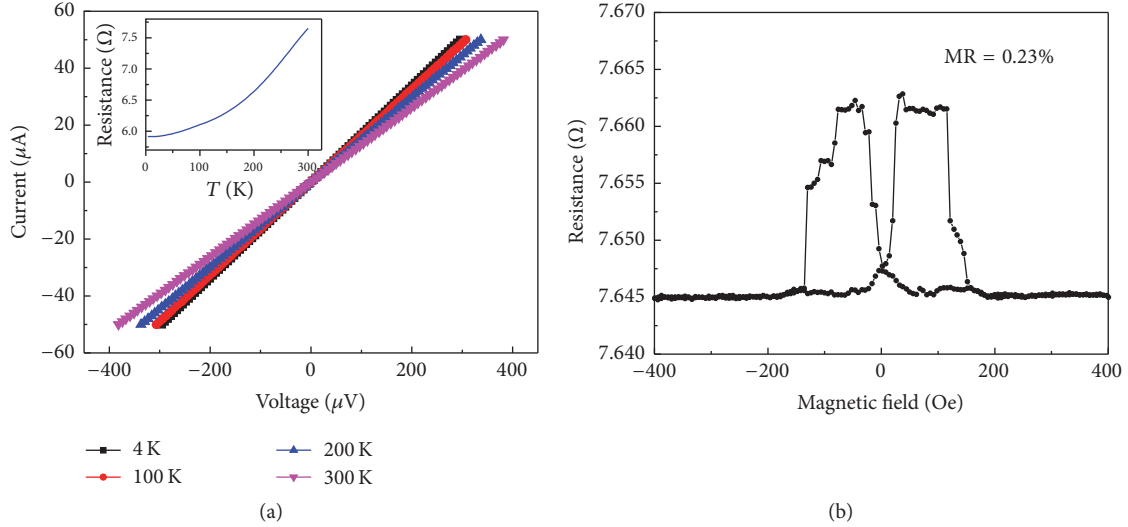


FIGURE 2: Characterizations of NiFe/BP/NiFe spin valve device. (a) The current-voltage curves of device at different temperature from 4 K to 300 K and resistance curve as a function of temperature at zero magnetic field in inset figure (a). (b) Resistance curves of device when external magnetic field is applied at 300 K and the value of MR is 0.23% for the structure of Py/BP/Py spin valve.

(RA) product of the device is on the order of $\sim 10^{-11} \Omega \cdot \text{m}^2$, which is smaller than that in the monolayer MoS_2 device ($\sim 10^{-10} \Omega \cdot \text{m}^2$ [10]). This difference may be related to the different band gaps (~ 0.5 eV in our device while ~ 1.87 eV in [10]). Note that the resistance decreases with reducing temperature, indicating that the BP behaves as a metal in the spin valve structure as shown in inset of Figure 2(a). The results suggest that the thin BP flake behaves as a conducting thin film rather than a tunnel barrier between the two FM electrodes, which is consistent with the previous works in MoS_2 and WS_2 based spin valve [10, 11].

Spin valve effect is characterized by measuring the resistance as a function of magnetic field. By sweeping the magnetic field, the resistance can be tuned into the high-resistance (R_{AP}) state and low-resistance (R_{P}) state since it depends on the orientation of the magnetization of the FM electrodes. The magnetoresistance is defined as $\text{MR} = 100 \times (R_{\text{AP}} - R_{\text{P}})/R_{\text{P}}$, where R_{AP} and R_{P} are the resistances when the magnetization vectors of two Py electrodes are antiparallel and parallel to each other, respectively. Note that the widths of the top and bottom electrodes were designed to be 500 nm and $2 \mu\text{m}$ as shown in Figure 1(c), respectively. This yields a large difference in coercivity between two FM electrodes. Thus the bottom electrode is easier to magnetize than the top one under the application of magnetic field owing to weaker shape anisotropy. The resistance as a function of magnetic field for a representative Py/BP/Py spin valve at room temperature is shown in Figure 2(b). As the magnetic field scan from -400 Oe to 400 Oe, the top and bottom electrodes switch in sequence, resulting in the observation of a resistance plateau. The MR value of the device is determined to be 0.23% at RT.

3.2. Temperature Dependence of the Spin Valve Effect. Figure 3(a) shows a series of MR curves for a representative

Py/BP/Py spin valve at various temperatures ranging from 4.2 K to 300 K. The maximum MR value is 0.57% at 4 K. A simple relation between the MR and the polarization of the FM electrodes for a junction can be approximated as $\text{MR} = 2P_1P_2/(1 - P_1P_2)$, where P_1 and P_2 are the electron spin polarization of the two FM metals, respectively [10]. Assuming that two FM electrodes have the same composition, then the polarization ($P_1 \approx P_2 = P$) of the two Py electrode is estimated to be $\sim 5\%$, which is comparable to the other values reported previously [10], but smaller than that ($P \sim 0.3$) in the Py/ Al_2O_3 interface. A possible reason for this reduced polarization is the exposure to air of the Py surface prior to the application of the BP layer. Some contaminants are inevitably adsorbed on the surface and air exposure of Py may produce antiferromagnetic NiO, significantly decreasing the spin polarization [22]. Future well-controlled fabrication process in situ without air exposure of the interfaces may improve the interface quality, maximizing the MR effect.

The magnitude of the MR monotonically decreases as the temperature is increased, as shown in Figure 3(b). The decrease in MR amplitude at higher temperature may be attributed to the inelastic scattering with phonons, magnetic impurity scattering, surface states, and thermal smearing of electron energy distribution in the FM metals [23]. The data are found to follow Bloch's law, where the spin polarization is described by $P(T) = P(0)(1 - \alpha T^{3/2})$. By fitting the data with MR relation by considering the temperature dependence of spin polarization, the material-dependent constant α can be estimated to be $5.9 \times 10^{-5} \text{ K}^{-3/2}$. This value is comparable to that of $3\sim 5 \times 10^{-5} \text{ K}^{-3/2}$ reported in the literature [24]. Temperature-dependent relation of parallel and antiparallel resistance are showed in Figure 3(c), which further indicated BP not as insulating barrier layer in the MTJ, but as metallic layer in vertical spin valve.

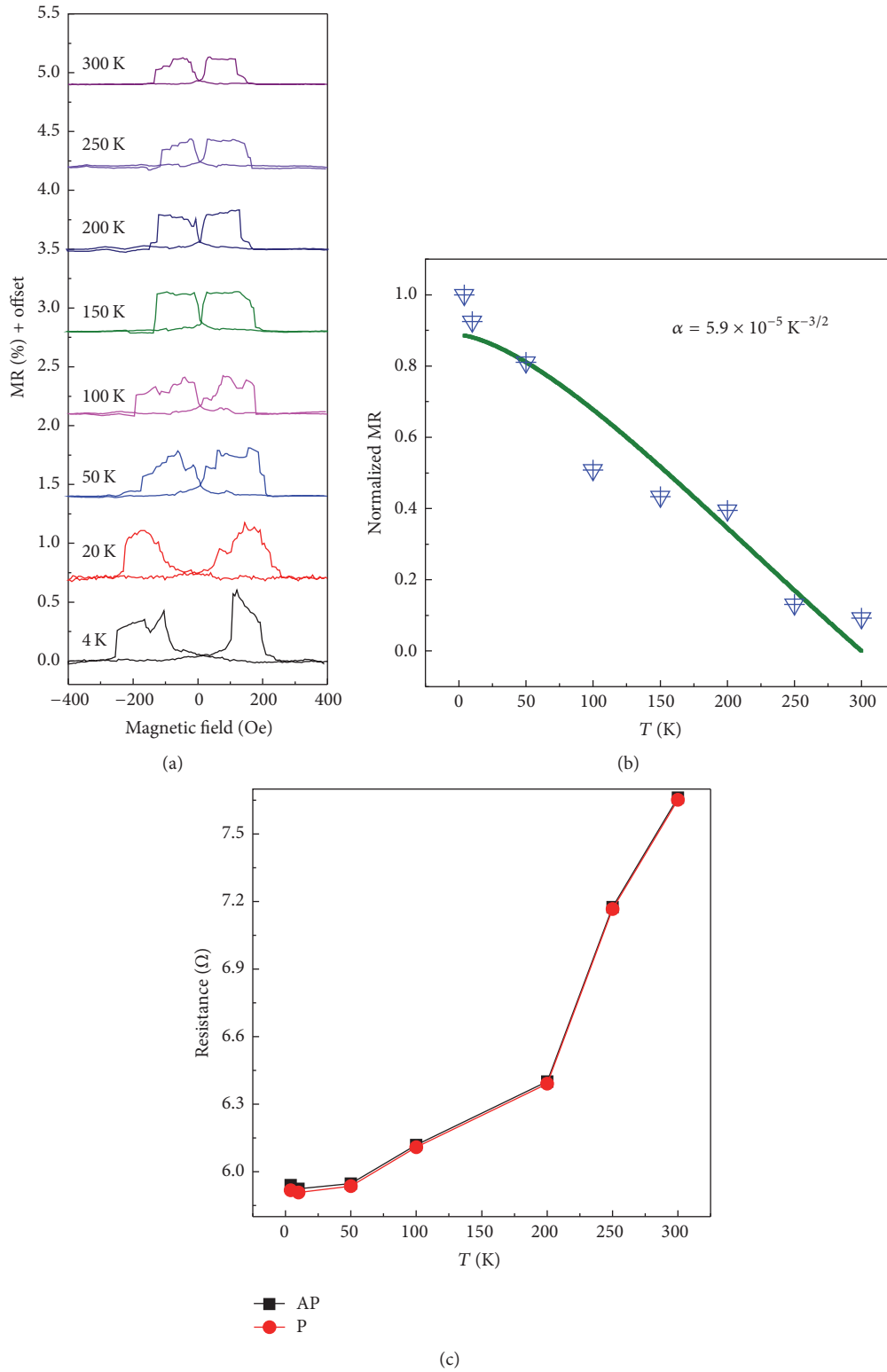


FIGURE 3: Temperature dependence of spin valve effect in NiFe/BP/NiFe device. (b) Normalized MR ratio as a function of temperature and the solid line is the fitting to Bloch's law. (c) Resistance of device, corresponding to low resistance (R_P) and high resistance (R_{AP}).

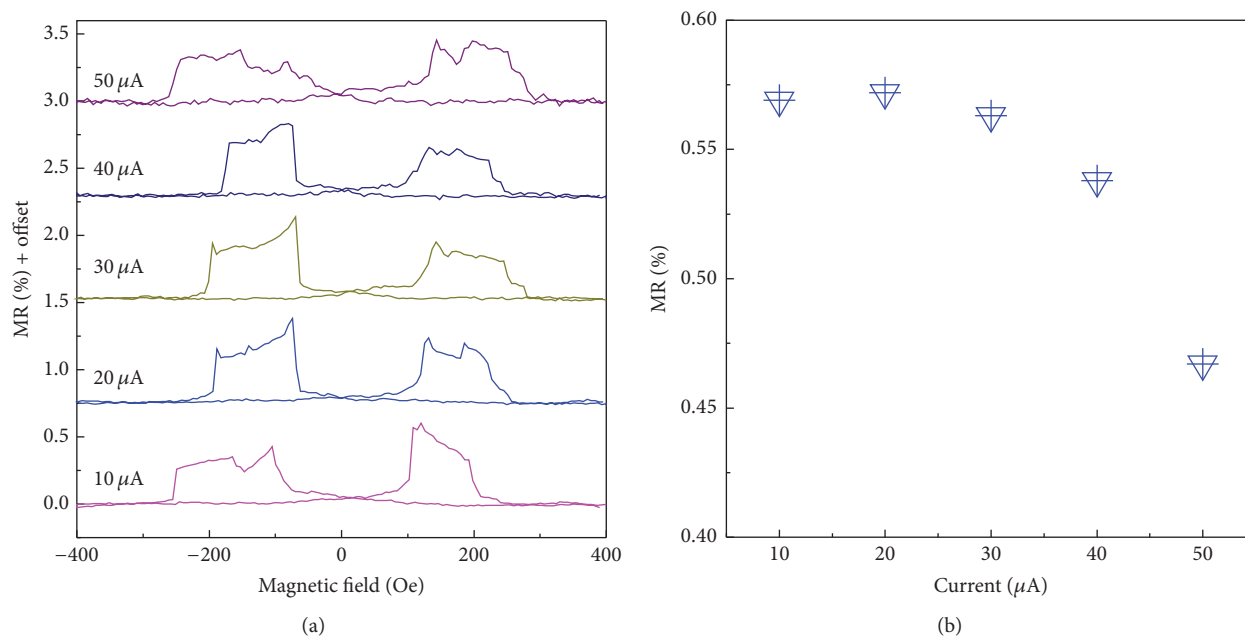


FIGURE 4: (a) Magnetoresistance curve at various bias currents. (b) MR ratio as a function of bias current.

3.3. Bias Current Dependence of the Spin Valve Effect. Finally, we investigated the bias current dependence of the spin valve effect. Figure 4(a) shows the resistance as a function of magnetic field at various bias currents from 10 μA to 50 μA at 4 K. The amplitude of MR value is found to be decreased as the bias current increases as shown in Figure 4(b). We attribute the decrease in MR value at larger bias current to the spin excitations localized at the interfaces between the FM electrodes and the BP interlayer [25] as well as the localized trap states in the BP interlayer [26] at the BP interlayer played a metallic property role in vertical spin valve. The results provide a possible approach to use the emerging BP nanomaterials for future spintronics applications such as magnetic memory and logic devices.

Competing Interests

The authors declare that they have no competing interests.

Acknowledgments

The work was supported by the National Natural Science Foundation of China (Grants nos. 11274343 and 91222110), National Science Fund for Distinguished Young Scholars (Grant no. 51025103), and Program for New Century Excellent Talents in University (NCET-13-0993).

References

- [1] M. Osada and T. Sasaki, "Two-dimensional dielectric nanosheets: novel nanoelectronics from nanocrystal building blocks," *Advanced Materials*, vol. 24, no. 2, pp. 210–228, 2012.
- [2] K. S. Novoselov, A. K. Geim, S. V. Morozov et al., "Electric field in atomically thin carbon films," *Science*, vol. 306, no. 5696, pp. 666–669, 2004.
- [3] B. Radisavljevic, A. Radenovic, J. Brivio, V. Giacometti, and A. Kis, "Single-layer MoS₂ transistors," *Nature Nanotechnology*, vol. 6, no. 3, pp. 147–150, 2011.
- [4] N. Tombros, C. Jozsa, M. Popinciuc, H. T. Jonkman, and B. J. Van Wees, "Electronic spin transport and spin precession in single graphene layers at room temperature," *Nature*, vol. 448, no. 7153, pp. 571–574, 2007.
- [5] W. Han, W. H. Wang, K. Pi et al., "Electron-hole asymmetry of spin injection and transport in single-layer graphene," *Physical Review Letters*, vol. 102, no. 13, Article ID 137205, 2009.
- [6] W. Han, K. Pi, W. Bao et al., "Electrical detection of spin precession in single layer graphene spin valves with transparent contacts," *Applied Physics Letters*, vol. 94, no. 22, Article ID 222109, 2009.
- [7] E. Cobas, A. L. Friedman, O. M. J. Van't Erve, J. T. Robinson, and B. T. Jonker, "Graphene as a tunnel barrier: graphene-based magnetic tunnel junctions," *Nano Letters*, vol. 12, no. 6, pp. 3000–3004, 2012.
- [8] M. Z. Iqbal, M. W. Iqbal, J. H. Lee, Y. S. Kim, S.-H. Chun, and J. Eom, "Spin valve effect of NiFe/graphene/NiFe junctions," *Nano Research*, vol. 6, no. 5, pp. 373–380, 2013.
- [9] A. Dankert, M. Venkata Kamalakar, A. Wajid, R. S. Patel, and S. P. Dash, "Tunnel magnetoresistance with atomically thin two-dimensional hexagonal boron nitride barriers," *Nano Research*, vol. 8, no. 4, pp. 1357–1364, 2015.
- [10] W. Wang, A. Narayan, L. Tang et al., "Spin-valve effect in NiFe/MoS₂/NiFe junctions," *Nano Letters*, vol. 15, no. 8, pp. 5261–5267, 2015.
- [11] M. Z. Iqbal, M. W. Iqbal, S. Siddique, M. F. Khan, and S. M. Ramay, "Room temperature spin valve effect in NiFe/WS₂/Co junctions," *Scientific Reports*, vol. 6, Article ID 21038, 2016.

- [12] H. X. Wei, Q. H. Qin, M. Ma, R. Sharif, and X. F. Han, "80% tunneling magnetoresistance at room temperature for thin Al-O barrier magnetic tunnel junction with CoFeB as free and reference layers," *Journal of Applied Physics*, vol. 101, no. 9, Article ID 09B501, 2007.
- [13] S. Yuasa, T. Nagahama, A. Fukushima, Y. Suzuki, and K. Ando, "Giant room-temperature magnetoresistance in single-crystal Fe/MgO/Fe magnetic tunnel junctions," *Nature Materials*, vol. 3, no. 12, pp. 868–871, 2004.
- [14] L. Li, Y. Yu, G. J. Ye et al., "Black phosphorus field-effect transistors," *Nature Nanotechnology*, vol. 9, no. 5, pp. 372–377, 2014.
- [15] F. Xia, H. Wang, and Y. Jia, "Rediscovering black phosphorus as an anisotropic layered material for optoelectronics and electronics," *Nature Communications*, vol. 5, article 4458, 2014.
- [16] A. Castellanos-Gomez, L. Vicarelli, E. Prada et al., "Isolation and characterization of few-layer black phosphorus," *2D Materials*, vol. 1, no. 2, Article ID 025001, 2014.
- [17] A. Castellanos-Gomez, M. Buscema, R. Molenaar et al., "Deterministic transfer of two-dimensional materials by all-dry viscoelastic stamping," *2D Materials*, vol. 1, no. 1, Article ID 011002, 2014.
- [18] B. Wan, B. Yang, Y. Wang et al., "Enhanced stability of black phosphorus field-effect transistors with SiO₂ passivation," *Nanotechnology*, vol. 26, no. 43, Article ID 435702, 2015.
- [19] M. Chen, Z. Yu, Y. Wang, Y. Xie, J. Wang, and H. Guo, "Nonequilibrium spin injection in monolayer black phosphorus," *Physical Chemistry Chemical Physics*, vol. 18, no. 3, pp. 1601–1606, 2016.
- [20] Y. Anugrah, M. C. Robbins, P. A. Crowell, and S. J. Koester, "Determination of the Schottky barrier height of ferromagnetic contacts to few-layer phosphorene," *Applied Physics Letters*, vol. 106, no. 10, Article ID 103108, 2015.
- [21] M. Venkata Kamalakar, B. N. Madhushankar, A. Dankert, and S. P. Dash, "Low schottky barrier black phosphorus field-effect devices with ferromagnetic tunnel contacts," *Small*, vol. 11, no. 18, pp. 2209–2216, 2015.
- [22] M. R. Fitzsimmons, T. J. Silva, and T. M. Crawford, "Surface oxidation of Permalloy thin films," *Physical Review B*, vol. 73, no. 1, Article ID 014420, 2006.
- [23] J. J. Åkerman, I. V. Roshchin, J. M. Slaughter, R. W. Dave, and I. K. Schuller, "Origin of temperature dependence in tunneling magnetoresistance," *Europhysics Letters*, vol. 63, no. 1, pp. 104–110, 2003.
- [24] C. H. Shang, J. Nowak, R. Jansen, and J. S. Moodera, "Temperature dependence of magnetoresistance and surface magnetization in ferromagnetic tunnel junctions," *Physical Review B*, vol. 58, no. 6, pp. R2917–R2920, 1998.
- [25] S. Zhang, P. M. Levy, A. C. Marley, and S. S. P. Parkin, "Quenching of magnetoresistance by hot electrons in magnetic tunnel junctions," *Physical Review Letters*, vol. 79, no. 19, pp. 3744–3747, 1997.
- [26] E. Y. Tsymbal, O. N. Mryasov, and P. R. LeClair, "Spin-dependent tunnelling in magnetic tunnel junctions," *Journal of Physics Condensed Matter*, vol. 15, no. 4, pp. R109–R142, 2003.

Research Article

Microstructure and Magnetic Properties of NdFeB Films through Nd Surface Diffusion Process

Wenfeng Liu, Mingang Zhang, Kewei Zhang, and Yuesheng Chai

School of Materials Science and Engineering, Institute of Advanced Materials, Taiyuan University of Science and Technology, Taiyuan 030024, China

Correspondence should be addressed to Mingang Zhang; mgzhang@163.com

Received 4 October 2016; Revised 5 December 2016; Accepted 19 December 2016; Published 18 January 2017

Academic Editor: Jingsheng Chen

Copyright © 2017 Wenfeng Liu et al. This is an open access article distributed under the Creative Commons Attribution License, which permits unrestricted use, distribution, and reproduction in any medium, provided the original work is properly cited.

Ta/Nd/NdFeB/Nd/Ta films were deposited by magnetron sputtering on Si (100) substrates and subsequently annealed for 30 min at 923 K in vacuum. It was found that the microstructure and magnetic properties of Ta/Nd/NdFeB/Nd/Ta films strongly depend on the NdFeB layer thickness. With NdFeB layer thickness increasing, both the grain size and the strain firstly reduce and then increase. When NdFeB layer thickness is 750 nm, the strain reaches the minimum value. Meanwhile, both the in-plane and perpendicular coercivities firstly drastically increase and then slowly decrease with NdFeB layer thickness increasing. The highest in-plane and perpendicular coercivities can be obtained at NdFeB layer thickness of 750 nm, which are 21.2 kOe and 19.5 kOe, respectively. In addition, the high remanence ratio (remanent magnetization/saturation magnetization) of 0.87 can also be achieved in Ta/Nd/NdFeB (750 nm)/Nd/Ta film.

1. Introduction

NdFeB permanent magnetic films have drawn extensive attention due to their excellent hard magnetic properties and potential applications in microelectromechanical system (MEMS), micromagnetic devices, and magnetic recording media [1–6]. The relatively low coercivity and poor thermal stability are the practical obstacle for applications of NdFeB films. One major approach to improve the properties is to increase the coercivity at the room temperature, which can suppress demagnetization at a higher operating temperature.

To increase the coercivity of NdFeB films, many researches have been reported. Fukagawa et al. reported that after sputtering Nd metal to the surface of NdFeB magnet and subsequent annealing an fcc interfacial phase was formed between the surface grains and the Nd layer, resulting in the recovery of surface coercivity [7]. Kim et al. reported that by Nd element diffusing from Nd layer into NdFeB layer high coercivity was achieved at the thickness ratio of Nd/NdFeB ≥ 1 . However, a rather low content of NdFeB hard magnetic phase existed in the films [8]. Li et al. reported that the coercivity of [NdFeB/Nd]₄ films was fairly increased because that Nd element effectively diffused [9].

In this work, Ta/Nd/NdFeB/Nd/Ta films were prepared on Si (100) substrates by magnetron sputtering. The effect of the NdFeB layer thickness on the microstructure and magnetic properties of Ta/Nd/NdFeB/Nd/Ta films was systematically investigated. The high in-plane and perpendicular coercivities can be obtained in Ta/Nd/NdFeB (750 nm)/Nd/Ta film, which are 21.2 kOe and 19.5 kOe, respectively. The high remanence ratio of 0.87 can also be achieved in the film.

2. Experimental Procedure

Ta/Nd/NdFeB/Nd/Ta films were prepared by FJL560II ultra-high vacuum magnetron sputtering system on Si (100) substrates. Here, Nd layer thickness was fixed at 250 nm. A Ta underlayer of 60 nm and Ta coverlayer of 60 nm were used to suppress the oxidation of NdFeB films. Pure Nd (99.9%) and Ta (99.95%) targets were used. The target for NdFeB layer was a commercial N33H NdFeB sintered target attached to B-chips. The base pressure of the deposition chamber was 2.0×10^{-4} Pa and high purity Ar gas was introduced during sputtering. The composition of NdFeB layer was determined to be Nd_{10.73}Fe_{84.01}B_{5.26} by a Thermo System 7 energy dispersive spectrometer (EDS). The as-deposited

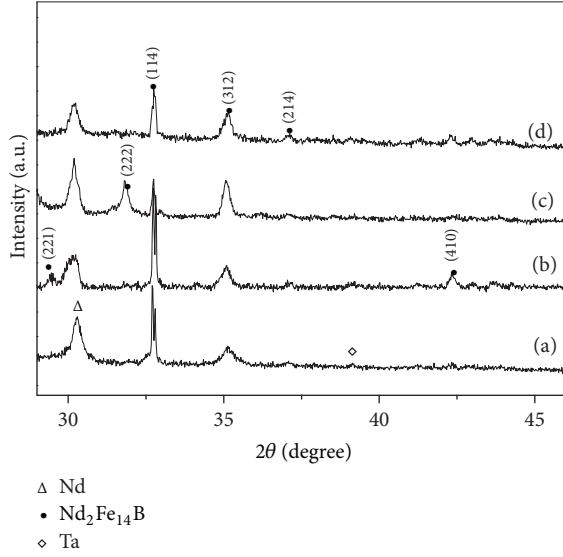


FIGURE 1: XRD patterns of Ta/Nd/NdFeB (x nm)/Nd/Ta ((a) $x = 450$; (b) $x = 600$; (c) $x = 750$; (d) $x = 900$) films.

films were subsequently annealed for 30 min at 923 K in vacuum.

The structure of the films was analyzed by Bruker-D8 X-ray diffraction (XRD) with Cu $K\alpha$ radiation. The thickness was characterized by a JSM-7001F field emission scanning electron microscope (FE-SEM). The magnetic properties were measured by a Quantum Design vibrating sample magnetometer (VSM) with a maximum applied field of 30 kOe.

3. Results and Discussion

Figure 1 shows the XRD patterns of Ta/Nd/NdFeB (x nm)/Nd/Ta ($x = 450, 600, 750, 900$) films. The prominent characterization peaks of (222), (114), (312), and (410) can be obviously seen in the XRD patterns, indicating the formation of tetragonal $\text{Nd}_2\text{Fe}_{14}\text{B}$ phase. In addition to the above-mentioned peaks, Nd peaks are also clearly observed in the XRD patterns, due to the existence of Nd layer.

XRD can be utilized to evaluate peak broadening with crystallite size and lattice strain due to dislocation [10]. Williamson-Hall (W-H) analysis [11] considers that the contributions to line broadening of the crystallite size and lattice strain are independent of each other and both have a Cauchy-like profile; the final line breadth is the sum

$$\beta_{hkl} = \beta_S + \beta_D, \quad (1)$$

$$\beta_{hkl} = \left(\frac{k\lambda}{D \cos \theta} \right) + (4\varepsilon \tan \theta). \quad (2)$$

Rearranging (2), we get

$$\beta_{hkl} \cos \theta = \left(\frac{k\lambda}{D} \right) + (4\varepsilon \sin \theta), \quad (3)$$

where D is the average grain size, K is the shape factor (0.9), λ is the wavelength of $\text{Cu}K_\alpha$ radiation, and ε is

the strain. The strain was assumed to be uniform in all crystallographic directions. As shown in Figure 2, $\beta \cos \theta$ was plotted with respect to $\sin \theta$ for the $\text{Nd}_2\text{Fe}_{14}\text{B}$ peaks of Ta/Nd/NdFeB/Nd/Ta films. The grain size and strain were calculated from the y -intercept and slope of the fitted line, respectively. Figure 3 shows the variation of the grain size and strain with NdFeB layer thickness in Ta/Nd/NdFeB/Nd/Ta films. With NdFeB layer thickness increasing from 450 nm to 900 nm, both the grain size and the strain firstly reduce and then increase. When the NdFeB layer thickness is 750 nm, the strain reaches the minimum value, which is equal to 0.0016.

Figure 4 shows the dependence of the coercivity on the NdFeB layer thickness in Ta/Nd/NdFeB/Nd/Ta films. With NdFeB layer thickness increasing from 450 nm to 750 nm, both the in-plane and perpendicular coercivities drastically increase. However, when NdFeB layer thickness further increases to 900 nm, both the in-plane and perpendicular coercivities slowly decrease. When NdFeB layer thickness is 750 nm, both the in-plane and perpendicular coercivities reach the maximum, which are 21.2 kOe and 19.5 kOe, respectively. It can be interpreted that the strain is minimized at the NdFeB layer of 750 nm, which is favorable for the crystallization of NdFeB.

Figure 5 shows the in-plane and out-of-plane hysteresis loops of Ta/Nd/NdFeB (750 nm)/Nd/Ta film. As seen in Figure 5, the in-plane and out-of-plane coercivities reach 21.2 kOe and 19.5 kOe, respectively. The high remanence ratio of 0.87 can also be noticed in the in-plane hysteresis loop, which is also important for the application of NdFeB film. It is very interesting that the out-of-plane hysteresis loop shows a kink near the original point, implying the existence of uncoupled soft magnetic grains, which becomes more significant while the external field is applied along the out-of-plane direction [12]. Moreover, the out-of-plane hysteresis loop shows two stage types of initial magnetization behavior with the first magnetization of high susceptibility followed by the second one of low susceptibility, which also suggests the independent magnetization of the uncoupled soft magnetic grains. Zhao et al. proposed that Fe is very likely to occur in $\text{Nd}_2\text{Fe}_{14}\text{B}$ so that many single-phased materials are in fact the two-phased ones [13].

The micromagnetic model was applied to clarify the coercivity mechanisms in permanent and composite materials. Coercivity is a linear function of H_A [14]:

$$H_{Ci}(T) = \alpha H_A(T) - N_{\text{eff}} M_s(T). \quad (4)$$

Here, H_A is the anisotropy field, $H_A = 2K_1/M_s$, which is the ideal coercivity for the coherent rotation of magnetically isolated single domain particles. M_s is the saturation magnetization. α and N_{eff} are the microstructure-dependent parameters. The parameter α describes the reduction in the anisotropy field due to the presence of crystallographic defects in the magnetically inhomogeneous region on the grain surface and misalignment of the grains. The parameter N_{eff} describes the local demagnetization field, which assists nucleation of the reversed domain under the action of the applied inverse field. The temperature dependence of K_1 is obtained from Durst and Kronmüller [15]. Figure 6 shows

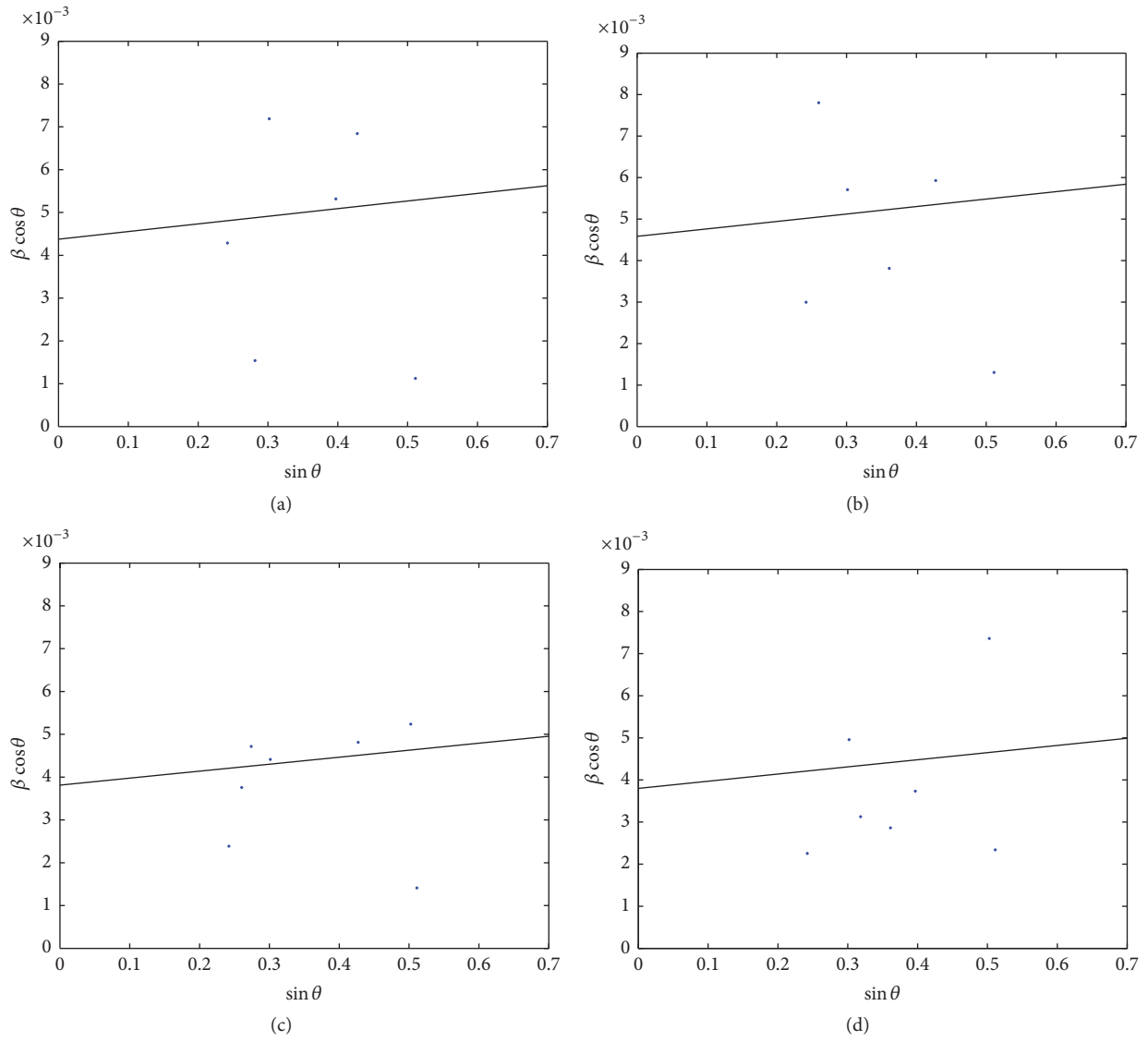


FIGURE 2: Plot of $\beta \cos \theta$ versus $\sin \theta$ of Ta/Nd/NdFeB (x nm)/Nd/Ta ((a) $x = 450$; (b) $x = 600$; (c) $x = 750$; (d) $x = 900$) films.

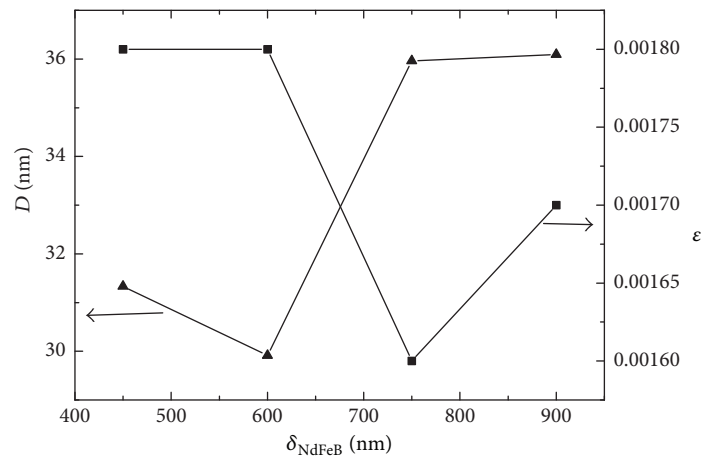


FIGURE 3: Variation of the grain size and strain with NdFeB layer thickness in Ta/Nd/NdFeB/Nd/Ta films.

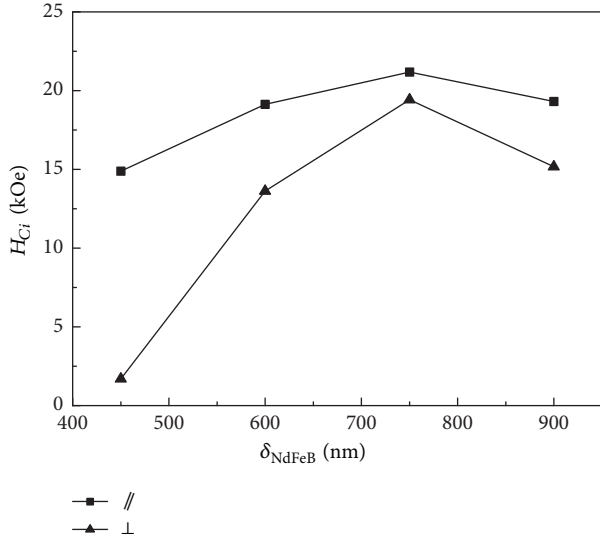


FIGURE 4: Dependence of the coercivity on the NdFeB layer thickness in Ta/Nd/NdFeB/Nd/Ta films.

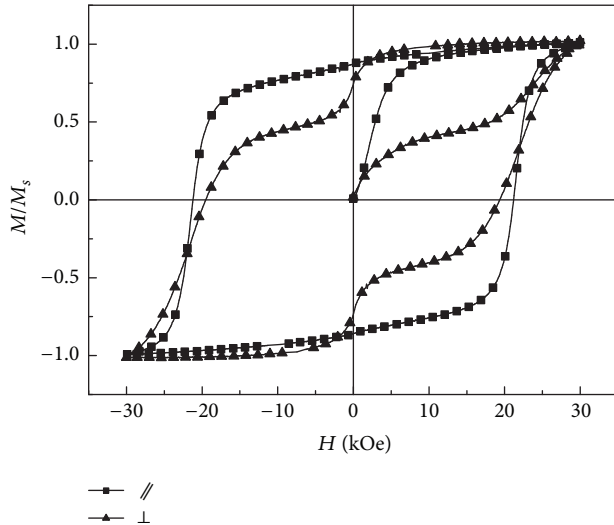


FIGURE 5: Hysteresis loops of Ta/Nd/NdFeB (750 nm)/Nd/Ta film.

the dependence of H_{Ci}/M_s on H_A/M_s for Ta/Nd/NdFeB (x nm)/Nd/Ta ($x = 450, 600, 750, 900$) films. The micromagnetic parameters α and N_{eff} were fitted by the least squares method and are shown in Figure 6. It can be noticed that α for Ta/Nd/NdFeB (750 nm)/Nd/Ta film is 0.257, which is larger than those of other Ta/Nd/NdFeB/Nd/Ta films. It suggests a decrease in the size of the distorted region and/or a considerable release of interfacial misfit at the NdFeB layer of 750 nm [16]. Zhao et al. proposed a self-pinning coercivity mechanism, incorporating elements of both initial local nucleation process and subsequent propagation of the domain wall to the main phase [13, 17]. Such a mechanism was firstly proposed in hard-soft multilayers and then extended to composite and permanent nanomagnets. The defects in the so-called single-phased permanent magnets act as the nucleation and pinning centers, which plays a role similar to the soft phase in hard-soft composite systems. Such

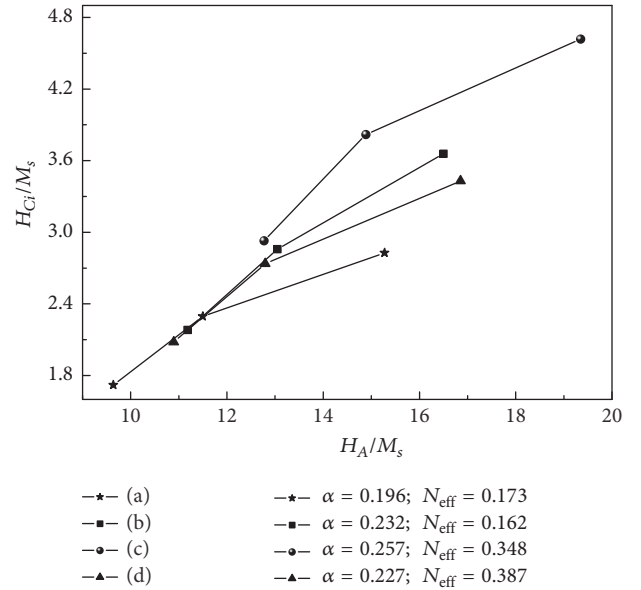


FIGURE 6: Dependence of H_{Ci}/M_s on H_A/M_s for Ta/Nd/NdFeB (x nm)/Nd/Ta ((a) $x = 450$; (b) $x = 600$; (c) $x = 750$; (d) $x = 900$) films.

self-pinning is attributed to the change of the intrinsic parameters associated with the phase change at the interface. In particular, for sufficiently large soft grains/defects, the pinning field can be expressed as $H_P = \alpha H_K$, where $H_K = 2k/M_s$ is the anisotropy field and α depends on the material parameters and micromagnetic structures. The coefficient α decreases as the volume occupation of the soft phase increases. For an exchange-coupled $\text{Nd}_2\text{Fe}_{14}\text{B}-\alpha\text{Fe}$ system with abrupt change of parameters in the interface, $\alpha = 0.1$. For the permanent magnets in which small amount of soft grains exists, $\alpha = 0.2-0.3$. As is shown in Figure 6, the α value is between 0.196 and 0.257, which is consistent with the theoretical value of the permanent magnets, indicating the existence of soft grains. It is accordant with the results concluded from Figure 5.

4. Conclusions

In summary, the microstructure and magnetic properties of Ta/Nd/NdFeB/Nd/Ta films are strongly dependent on the NdFeB layer thickness. When NdFeB layer thickness is 750 nm, the strain reaches the minimum value. Meanwhile, the highest in-plane and perpendicular coercivities can be obtained at NdFeB layer thickness of 750 nm, which are, respectively, 21.2 kOe and 19.5 kOe, because the strain is minimized. The high remanence ratio of 0.87 can also be achieved in Ta/Nd/NdFeB (750 nm)/Nd/Ta film. Altogether, the results suggest that Ta/Nd/NdFeB/Nd/Ta film may have a significant potential as a magnetic material with excellent performance.

Competing Interests

The authors declare that there is no conflict of interests regarding the publication of this paper.

Acknowledgments

This work was supported by the National Natural Science Foundation of China (no. 51305290), the Higher Education Technical Innovation Project of Shanxi Province, China (no. 2013133), the Fund Program for the Scientific Activities of Selected Returned Overseas Professionals of Shanxi Province, China (no. 2015003), the Research Project Supported by Shanxi Scholarship Council, China (no. 2013-098), and the Graduate Student Joint Training Project of Shanxi Province, China (no. 2016JD36).

References

- [1] J. J. Croat, J. F. Herbst, R. W. Lee, and F. E. Pinkerton, "Pr-Fe and Nd-Fe-based materials: a new class of high-performance permanent magnets (invited)," *Journal of Applied Physics*, vol. 55, no. 6, pp. 2078–2082, 1984.
- [2] Y. Kaneko, K. Tokuhara, and N. Ishigaki, "Research on high performance Nd-Fe-B sintered magnets," *Vacuum*, vol. 47, no. 6-8, pp. 907–910, 1996.
- [3] M. Nakano, R. Katoh, H. Fukunaga, S. Tutumi, and F. Yamashita, "Fabrication of Nd-Fe-B Thick-Film Magnets by High-Speed PLD Method," *IEEE Transactions on Magnetics*, vol. 39, no. 5, pp. 2863–2865, 2003.
- [4] W. Szmaja, J. Grobelny, M. Cichomski, and K. Makita, "Application of MFM for studying Nd-Fe-B magnets," *Vacuum*, vol. 74, no. 2, pp. 297–300, 2004.
- [5] C. Constantinescu, N. Scarisoreanu, A. Moldovan, M. Dinescu, L. Petrescu, and G. Epureanu, "Thin films of NdFeB deposited by PLD technique," *Applied Surface Science*, vol. 253, no. 19, pp. 8192–8196, 2007.
- [6] S. Sinnema, R. J. Radwanski, J. J. M. Franse, D. B. de Mooij, and K. H. J. Buschow, "Magnetic properties of ternary rare-earth compounds of the type R₂Fe₁₄B," *Journal of Magnetism and Magnetic Materials*, vol. 44, no. 3, pp. 333–341, 1984.
- [7] T. Fukagawa, T. Ohkubo, S. Hirose, and K. Hono, "Nano-sized disorders in hard magnetic grains and their influence on magnetization reversal at artificial Nd/Nd₂Fe₁₄B interfaces," *Journal of Magnetism and Magnetic Materials*, vol. 322, no. 21, pp. 3346–3350, 2010.
- [8] M.-J. Kim, Y. Li, Y.-B. Kim et al., "Magnetic properties of NdFeB thin film obtained by diffusion annealing," *IEEE Transactions on Magnetics*, vol. 36, no. 5, pp. 3370–3372, 2000.
- [9] D. Li, S. Suzuki, T. Horikawa, M. Itoh, and K.-I. Machida, "Grain boundary phase formation and magnetic properties of NdFeB/Nd multilayered films," *Japanese Journal of Applied Physics*, vol. 48, no. 3, p. 033002, 2009.
- [10] R. Yogamalar, R. Srinivasan, A. Vinu, K. Ariga, and A. C. Bose, "X-ray peak broadening analysis in ZnO nanoparticles," *Solid State Communications*, vol. 149, no. 43-44, pp. 1919–1923, 2009.
- [11] W. H. Hall, "X-ray line broadening in metals," *Proceedings of the Physical Society A*, vol. 62, no. 11, pp. 741–743, 1949.
- [12] N. Tian, Y. F. Li, F. Hong, and C. Y. You, "Fabrication of high coercive Nd-Fe-B based thin films through annealing Nd-Fe-B/Nd-Fe multilayers," *Physica B: Condensed Matter*, vol. 477, pp. 129–132, 2015.
- [13] G. P. Zhao, H. W. Zhang, Y. P. Feng, C. Yang, and C. W. Huang, "Nucleation or pinning: dominant coercivity mechanism in exchange-coupled permanent/composite magnets," *Computational Materials Science*, vol. 44, no. 1, pp. 122–126, 2008.
- [14] H. Kronmüller, "The nucleation fields of uniaxial ferromagnetic crystals," *Physica Status Solidi (B)*, vol. 130, no. 1, pp. 197–203, 1985.
- [15] K.-D. Durst and H. Kronmüller, "Determination of intrinsic magnetic material parameters of Nd₂Fe₁₄B from magnetic measurements of sintered Nd₁₅Fe₇₇B₈ magnets," *Journal of Magnetism and Magnetic Materials*, vol. 59, no. 1-2, pp. 86–94, 1986.
- [16] W. B. Cui, Y. K. Takahashi, and K. Hono, "Microstructure optimization to achieve high coercivity in anisotropic Nd-Fe-B thin films," *Acta Materialia*, vol. 59, no. 20, pp. 7768–7775, 2011.
- [17] G. P. Zhao, L. Chen, C. W. Huang, N. L. Guo, and Y. P. Feng, "Micromagnetic calculation of hysteresis loops in exchange-coupled nanolayers," *Solid State Communications*, vol. 150, no. 31-32, pp. 1486–1488, 2010.

Research Article

Perpendicular Giant Magnetoresistance and Magnetic Properties of Co/Cu Nanowire Arrays Affected by Period Number and Copper Layer Thickness

Juan Han, Xiufang Qin, Zhiyong Quan, Lanfang Wang, and Xiaohong Xu

School of Chemistry and Materials Science, Key Laboratory of Magnetic Molecules and Magnetic Information Materials, Ministry of Education, Shanxi Normal University, Linfen 041004, China

Correspondence should be addressed to Xiaohong Xu; xuxh@sxnu.edu.cn

Received 20 September 2016; Accepted 15 November 2016

Academic Editor: Mohindar S. Seehra

Copyright © 2016 Juan Han et al. This is an open access article distributed under the Creative Commons Attribution License, which permits unrestricted use, distribution, and reproduction in any medium, provided the original work is properly cited.

One-dimensional magnetic nanowires have attracted much attention in the last decades due to their unique physical properties and potential applications in magnetic recording and spintronics. In this work, ordered arrays of Co/Cu multilayered nanowires which can be exploited to develop magnetoresistive sensors were successfully prepared using porous anodic alumina (PAA) templates. The structure and morphology of the multilayered nanowire arrays were characterized by transmission electron microscopy and scanning electron microscopy. The nanowire arrays are highly ordered and the average diameter is about 50 nm, which is controlled by the pore diameter of the PAA templates. The influences of period number and Cu layer thickness on the magnetic and the giant magnetoresistance (GMR) properties were investigated. The coercivity and remanence ratio increase first and then gradually tend to be stable with the increase of period number and the Cu layer thickness, while the GMR ratio increases first and then decreases with the increase of the period number accompanied by an oscillatory behavior of GMR as the Cu layer thickness changes, which are ascribed to the spin dependence electron scattering in the multilayers. The optimum GMR of -13% appears at Co (50 nm)/Cu (5 nm) with 200 deposition cycles in our experimental conditions.

1. Introduction

Giant magnetoresistance (GMR) effect is a phenomenon where the resistivity of the material will be affected significantly with the application of an external magnetic field. Since the discovery of the GMR effect in 1988 [1–3], GMR multilayered structures consisting of ferromagnetic layers separated by a nonmagnetic spacer layer have been focused on due to their unique potential in technological applications, such as high-density data storage, GMR sensors, and magnetic random access memory. Particularly, multilayered nanowires consisting of alternating magnetic and nonmagnetic layers are an ideal system to investigate GMR effect in the current perpendicular to the plane (CPP) geometry as it has been shown to exhibit a more significant GMR effect and high aspect ratio (length/diameter) of the multilayered nanowires leading to larger resistance that enables high accuracy in the measurements [4]. One of the frequently used fabrication

methods of the high-aspect-ratio multilayered nanowires is the electrodeposition technique due to its simplicity, convenience, and cost-effectiveness compared to the other preparation techniques that have been employed such as chemical vapor deposition, molecular beam epitaxy, and magnetron sputtering [5–8]. So far, great efforts have been devoted to the research on the CPP-GMR of CoNi/Cu [9–11], NiFe/Cu [12–14], and Co/Cu [7, 15–17] multilayered nanowires and it has been shown that the GMR and the magnetic properties of multilayer nanowire arrays are affected by a variety of factors, including the structure of the materials, wire diameter, wire total length, composition, layer thickness, and other factors. However, only few studies have systematically investigated the effects of the period number and copper layer thickness on the magnetic properties and the CPP-GMR [5–7].

In this study, the Co/Cu multilayered nanowire arrays are considered to be an attractive system for gaining insights into the CPP-GMR and magnetic properties due to the nanowires'

perfect band matching and lattice matching [17, 18]. Co/Cu multilayered nanowire arrays were prepared in PAA templates via single bath by electrochemical method and the effects of repeat period number and copper layer thickness on magnetic properties and CPP-GMR of Co/Cu nanowire arrays were studied. It is evident from the experiment that the periodicity of the multilayered nanowires and the non-magnetic layer thickness play a crucial role in deciding the magnetic and CPP-GMR of the multilayered nanowire arrays.

2. Experimental Details

High purity aluminum foil (99.999%, 0.2 mm thickness) was first degreased in acetone and ethanol for 10 min and then annealed at 500°C under vacuum for 3 h to remove the mechanical stress. Afterwards, the aluminum foil was electropolished in a mixture of HClO₄ and C₂H₅OH (1:4 volume ratio) and then rinsed carefully with distilled water. The first anodization was carried out in 0.3 M oxalic acid at 5°C for 5 h under a constant voltage of 40 V. After the anodized layer was dissolved in a mixture of phosphoric acid (6.0 wt%) and chromic acid (1.8 wt%) at 60°C for 3 h, the second anodization was done under the same conditions as the first one. A mixed solution of 0.1 M CuCl₂ and 20% HCl was employed to etch away the aluminum, resulting in free-standing PAA. In addition, a subsequent etching treatment was performed in a 5 wt% H₃PO₄ solution at 30°C for 50 min to remove the barrier layer and slightly widen the pores of the PAA template.

The electrodeposition of the multilayered nanowires was performed at 25°C using single bath by electrochemical method. Ag/AgCl (in 4 M KCl) served as the reference electrode and a Pt wire served as the counter electrode. The electrolytic solution contains 84.3 g/L CoSO₄·7H₂O, 0.57 g/L CuSO₄, and 50 g/L H₃BO₃ with the pH value kept around 3.7. The multilayered nanowires were electrodeposited using an electrochemical workstation technique in a standard three-electrode mode by periodically switching the deposition potential between -1.0 V and -0.52 V for the deposition of the Co and Cu layers, respectively, and the thickness of each layer was controlled conveniently by the pulse duration because the thickness is proportional to the electrodeposition time under the same experimental condition.

The morphology and structural analysis of nanowires were measured by scanning electron microscopy (SEM) and transmission electron microscopy (TEM). For SEM and TEM observation, the PAA template was dissolved in 1 M NaOH solution and the residual NaOH solution absorbed on the surface of the PAA template was removed by rinsing the nanowires carefully with deionized water. The magnetic properties were measured by vibrating sample magnetometer (VSM) and the GMR measurements were performed by physical property measurement system (PPMS, Quantum Design PPMS-9) at room temperature and the GMR percentage was calculated according to the definition:

$$\text{GMR} = \frac{(R_H - R_0)}{R_0}, \quad (1)$$

where R_H is the resistance in the applied magnetic field H and R_0 is the resistance of the sample in zero magnetic field. Since the room temperature GMR is more appealing for industrial applications, this current work presents only room temperature GMR.

The model to carry out the GMR measurements is shown in Figure 1. After the electrodeposition of the nanowires, the sample was attached on a glass sheet by silver conductive epoxy and the top side of the unfilled PAA is etched away by NaOH through controlling appropriate reactive time so that the nanowires can emerge from the template to contact with a tiny drop of silver epoxy for GMR measurement. Using this method, the CPP-GMR of the nanowires at the desired position on the sample can be measured so that it is possible to perform a number of measurements at different positions on the same sample by dropping the silver epoxy at different positions.

3. Results and Discussion

Figure 2(a) is the potential-time ($E-t$) profile during the Co/Cu nanowires electrodeposition process. When a low negative potential is applied, only Cu can be deposited, while at higher negative potential Co can be deposited to form a ferromagnetic layer. The current was recorded in the process as can be seen from Figure 2(b). The current of each cycle is basically the same and no significant increase of the recorded current was observed during the electrodeposition process, indicating that the quantity of the electric charge of each period is equal, which is a prerequisite to ensure the bilayer thickness constancy of each layer. As described above, the thickness of the Co layers and the Cu layers can be conveniently controlled by changing the time strictly in the deposition process.

The Co/Cu nanowires were liberated from the PAA template by dissolving the PAA template in 1 M NaOH solution and washing it several times with deionized water. Figure 3(a) shows the SEM image of the Co/Cu nanowires prepared at $t_{\text{Co}} = 21$ s and $t_{\text{Cu}} = 17$ s after removing the PAA template. By removing the PAA template, the nanowires are bundled together. The typical TEM images of Co/Cu prepared at $t_{\text{Co}} = 21$ s and $t_{\text{Cu}} = 17$ s are shown in Figure 3(b). It reveals that the nanowires are smooth and uniform along the length. The Co/Cu multilayered nanowires show a clear bamboo-like structure. The average thickness of Co layer is around 50 nm and the Cu layer is 5 nm, which corresponds to 2.38 nm/s for the Co rate of growth and 0.3 nm/s for Cu. The XRD pattern corresponding to the multilayered nanowires array is shown in Figure 3(c). The hcp (100), (110), and (200) diffraction peaks of Co are observed at $2\theta = 41.73^\circ$, 75.93° , and 90.61° , respectively. The diffraction peak at 2θ value of 43.29° corresponds to the face centered cubic (fcc) (111) crystalline plane of Cu.

In order to study the effect of Cu layer thickness on the magnetic and CPP-GMR properties, Co/Cu multilayered nanowires with different lengths of Cu layers were fabricated while the Co length was fixed at 50 nm in each Co/Cu unit. The selected Cu layer lengths are 3 nm, 5 nm, 10 nm, 18 nm, and 30 nm and the magnetic hysteresis loops were measured with the applied magnetic field parallel to the nanowires. The

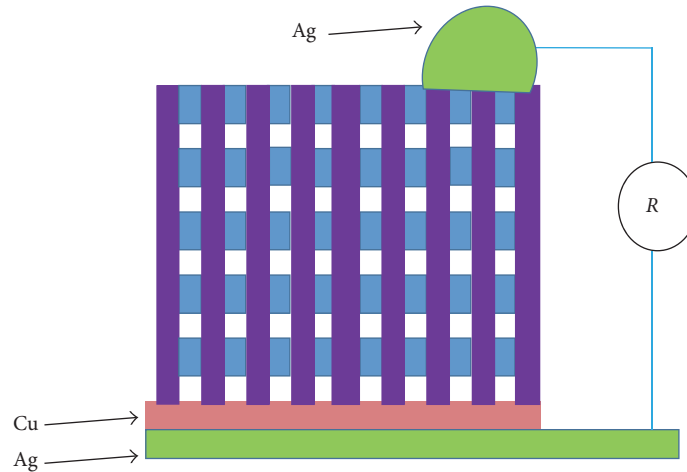


FIGURE 1: Schematic structure of the GMR measurements.

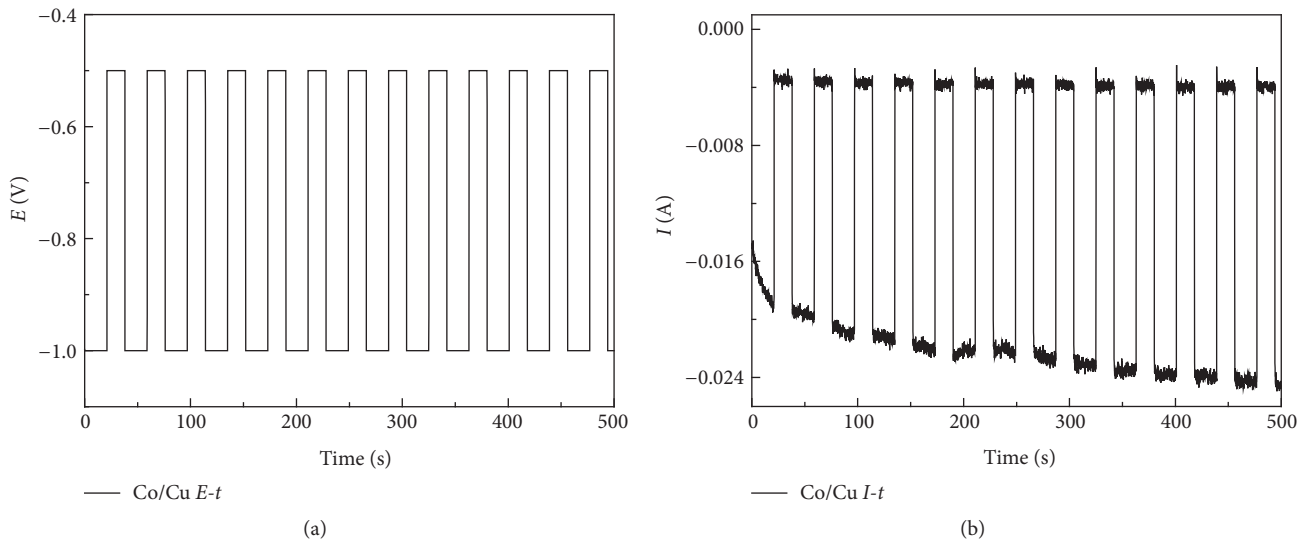


FIGURE 2: (a) Typical $E-t$ curve recorded during the Co/Cu nanowires electrodeposition process. (b) The dependence of the observed current and time during the nanowire electrodeposition process.

dependence of magnetic properties on Cu layer thickness is shown in Figure 4. The coercivity and remanence ratio both increase with the increase of the length of the Cu, which can be caused by a reduced dipole-dipole interaction between the Co layers as the thickness of the Cu layer increased [9].

Figures 5(a)–5(e) show the GMR curves of the nanowire arrays with different lengths of Cu under an applied magnetic field parallel to the nanowires. As presented in Figure 5(f), the CPP-GMR shows oscillation dependence on the thickness of the Cu layer. The GMR oscillates according to the Cu layer thickness, which is consistent with similar systems in different metallic superlattice structures with a spacer layer [13]. The thickness of the nonmagnetic Cu layer influences the interlayer exchange coupling between the ferromagnetic layers which will cause incoherent magnetic reversal rotation, thus leading to oscillations in GMR [19]. With the increasing of the Cu layer, the pinhole density reduces and the layer

thickness uniformity improves, which both lead to weakening of the FM coupling. The reduction in FM coupling enables a more random magnetization orientation of the adjacent layers and thus the GMR effect increases. However, with the Cu layer thickness increasing, there appear inevitable disadvantages in the Cu layer. The thicker the Cu layer, the more the defects, and significant spin flipping of the conduction electrons takes place during the transmission process, which will reduce the spin dependent electron scattering, so the GMR declines partly [20]. So, under the common action of the dual mechanisms, the GMR effect presents an oscillation phenomenon with the increase of the thickness of the Cu layer.

The dependence of magnetic properties on the number of bilayers is displayed in Figure 6 and the coercivity and remanence ratio increase first and then gradually tend to be stable. The possible reason for this phenomenon is that

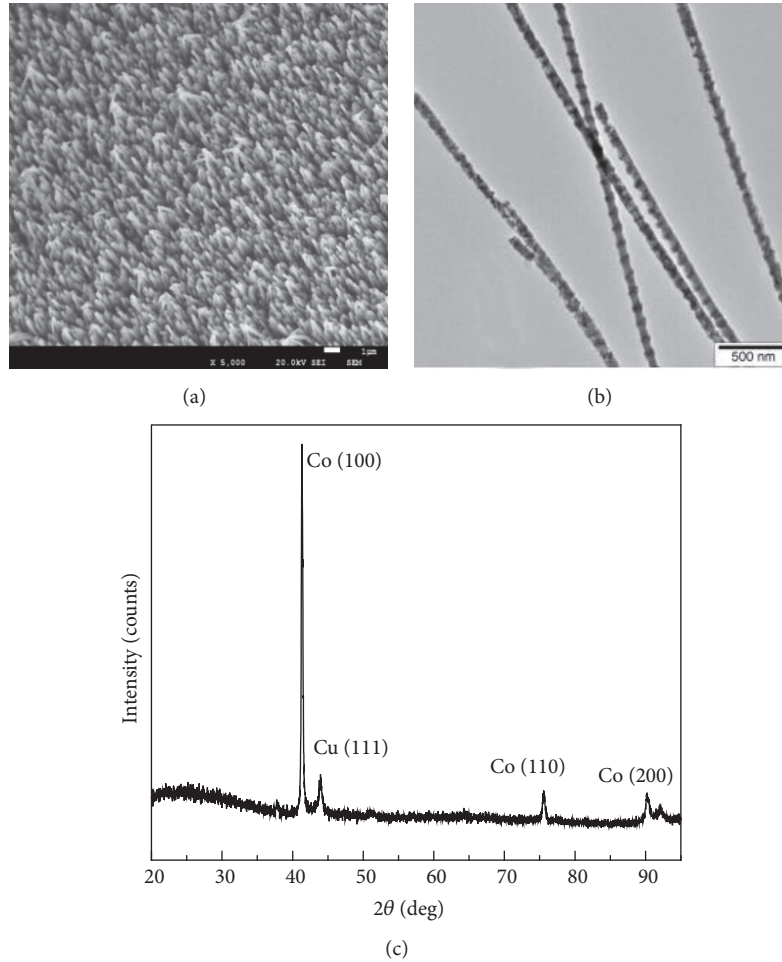


FIGURE 3: SEM (a), TEM profile image (b), and XRD pattern (c) of the Co (50 nm)/Cu (5 nm) nanowires prepared at $t_{\text{Co}} = 21$ s and $t_{\text{Cu}} = 17$ s after removing the PAA template.

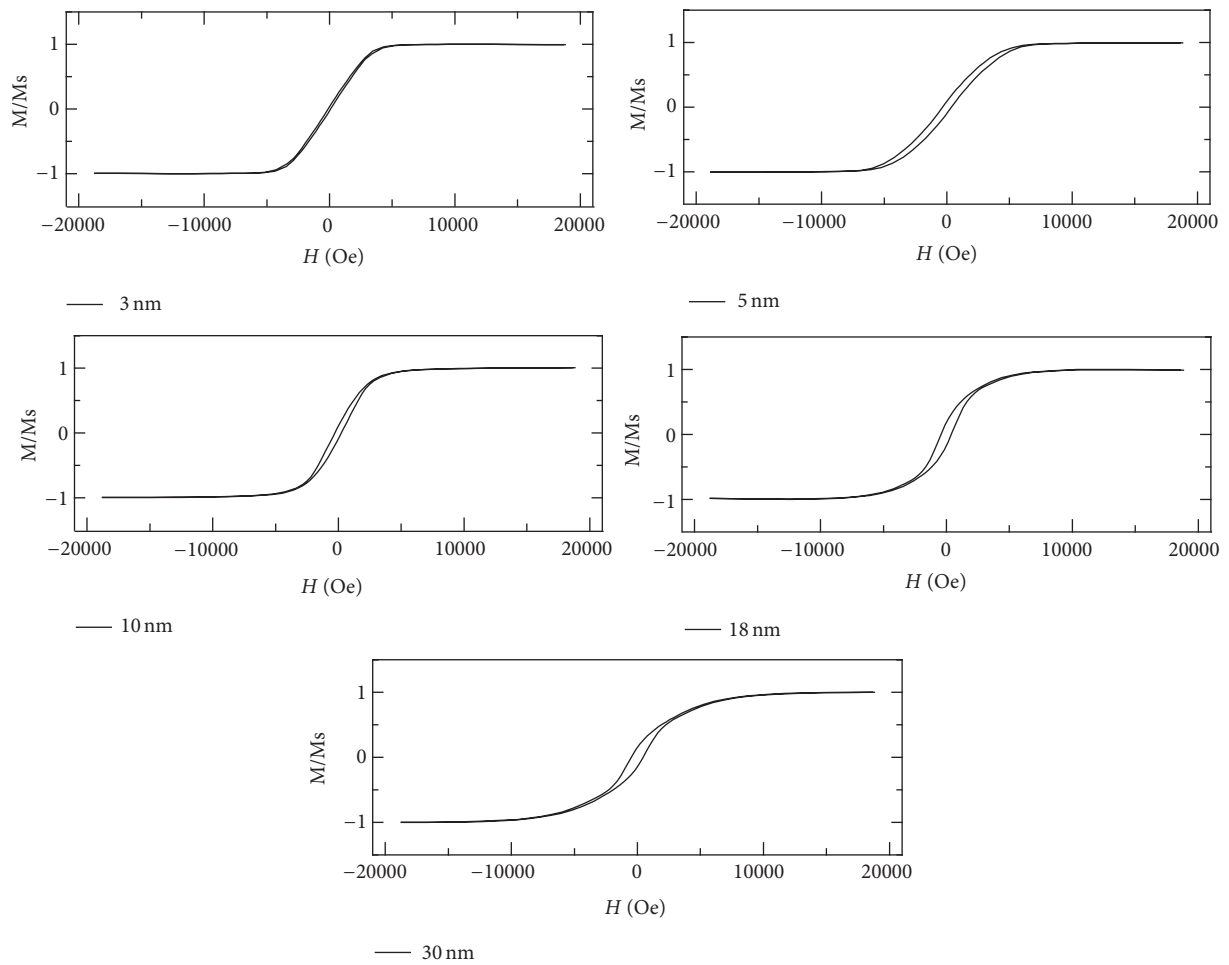
coercivity is mainly caused by domain wall pinning effect [21]; with the increase of the length, the domain walls will produce pinning effect and there will be many defects and impurities resulting in more pinning points which increase the coercivity.

The number of bilayers is an important factor that affects CPP-GMR since it directly relates to the material resistance. Here, the variation of bilayers and its effect on the CPP-GMR properties were studied. Based on the previous measure methods, we measured the CPP-GMR hysteresis of Co/Cu multilayered nanowires with the applied magnetic field parallel to the nanowires. The period number was varied between 50, 100, 150, 200, and 250. Figures 7(a)–7(e) show the CPP-GMR curves of Co/Cu multilayered nanowires with different Co/Cu bilayers (50, 100, 150, 200, and 250 Co/Cu bilayers) electrodeposited into porous anodic alumina. The 200-bilayer nanowire sample shows -13% GMR, while the 50-bilayer nanowire sample shows only 0.6% GMR. Figure 7(f) shows the relationship between CPP-GMR ratio and the number of bilayers of Co/Cu multilayered nanowires. We can see that the CPP-GMR ratio increases first and then decreases with the increase of the repeat period number.

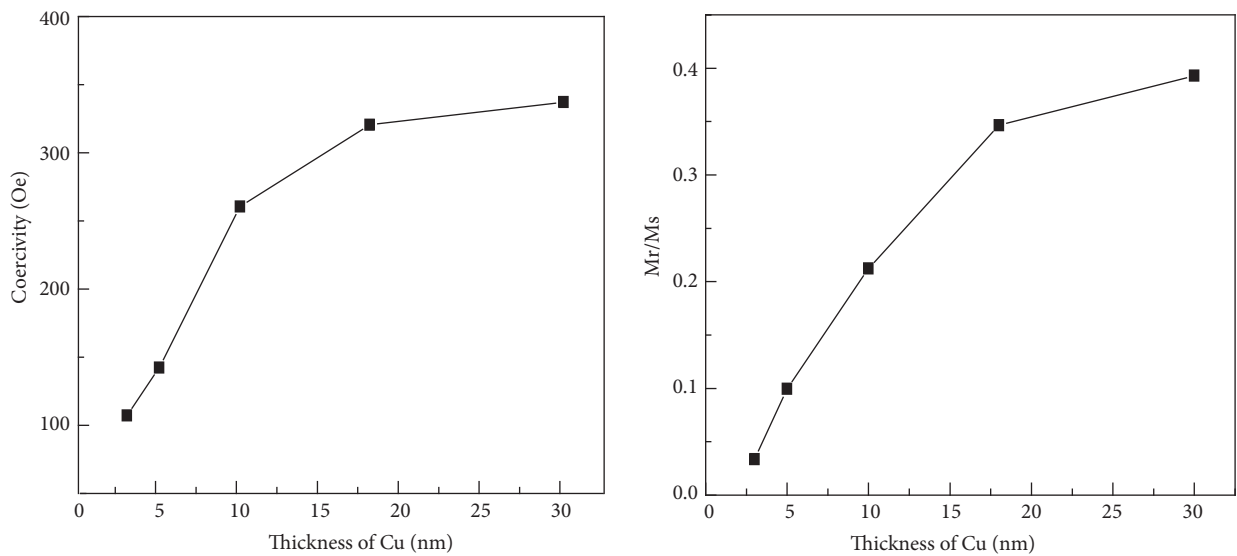
The increase can be explained by the fact that an increase in number of bilayers increases the number of interfaces, leading to more interface electron scattering and decreasing the shunting effect of the metallic conductive layer [10], and thus CPP-GMR increases. The decrease is ascribed to the gradual deterioration of the structure as the deposit grows; the multilayer interfaces are more significant at the beginning of the deposit than later. In other words, the gradual inhomogeneities during the deposition process of the bilayers could be responsible for the later reduction in CPP-GMR. This result confirms the fact that the interfaces play an important role in CPP-GMR.

4. Conclusions

In summary, highly ordered and homogeneously aligned Co/Cu multilayered nanowire arrays were prepared by single-bath electrodeposition method. The effects of repeat period number and copper layer thickness on magnetic and CPP-GMR of Co/Cu nanowire arrays were investigated. We have highlighted the importance of nonmagnetic layer thickness and the number of bilayers upon the magnetic and CPP-GMR



(a)



(b)

FIGURE 4: (a) Magnetic hysteresis loops of the Co/Cu nanowires with Co (50 nm) and Cu varied from 3 nm to 30 nm. (b) Evolution of the coercivity (H_c) and remanence ratio (M_r/M_s) with the change of Cu layer thickness under applied magnetic field parallel to the nanowires.

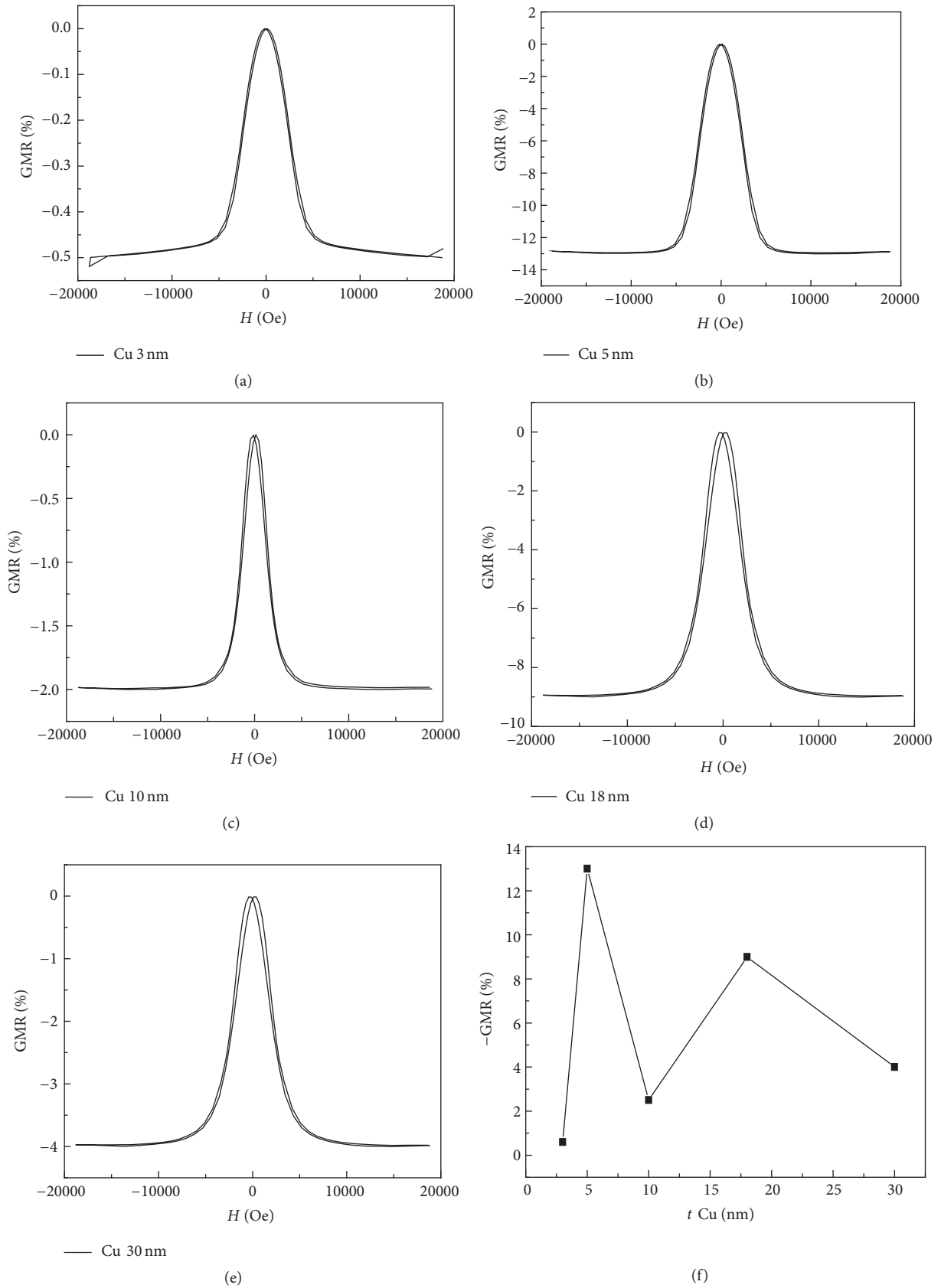
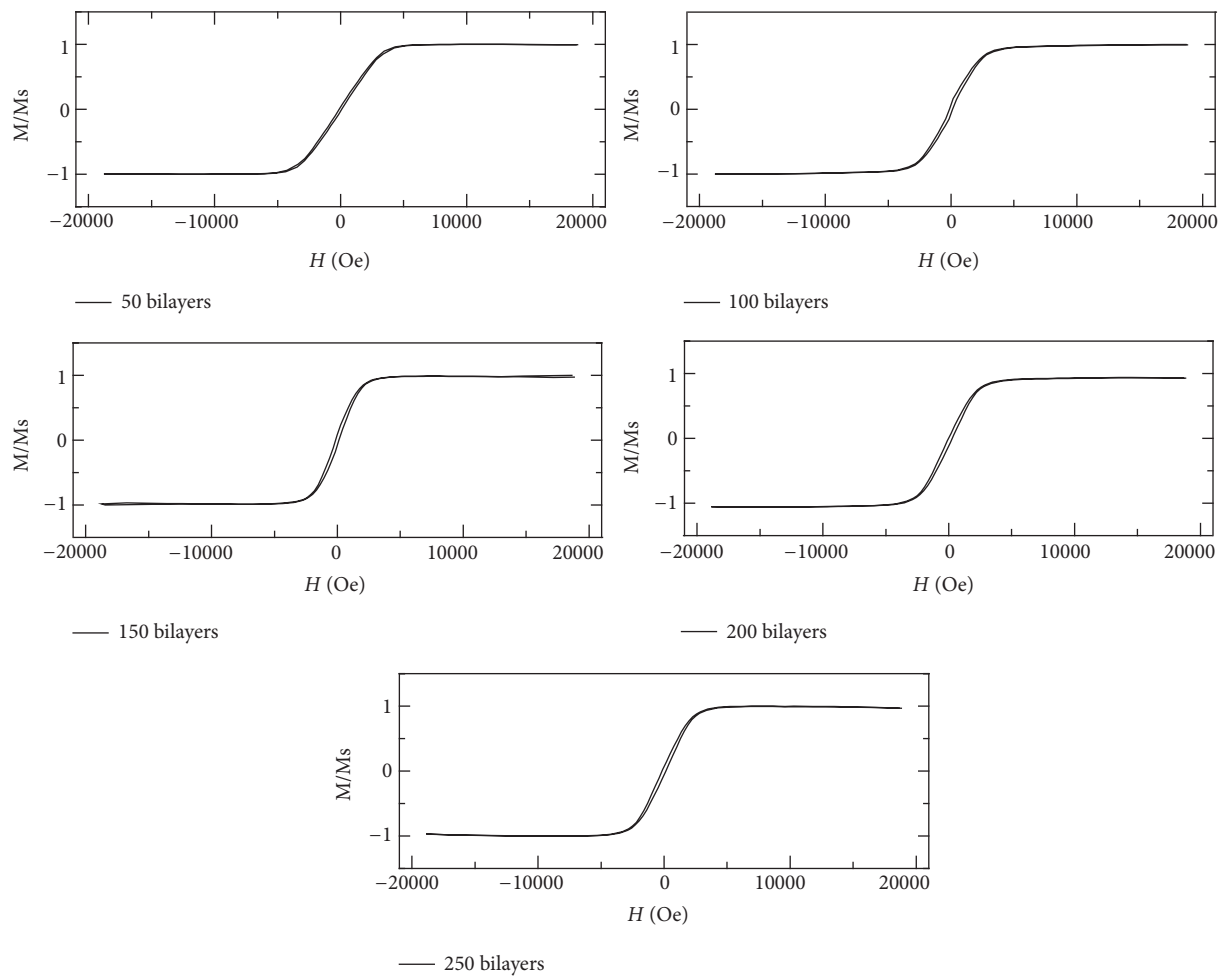
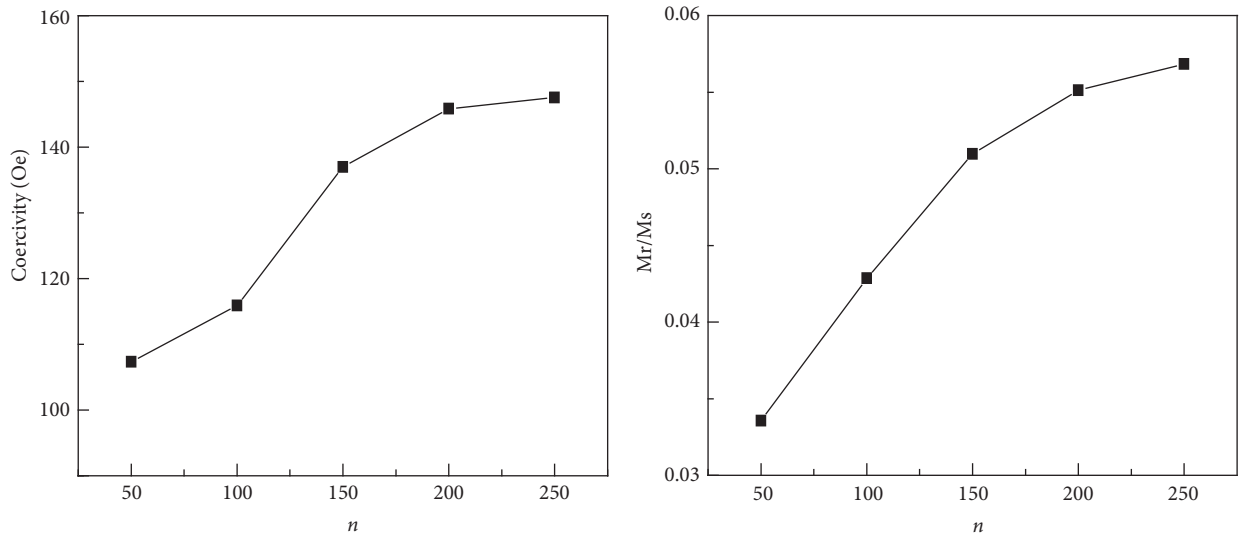


FIGURE 5: (a)–(e) The CPP-GMR curves of Co (50 nm)/Cu (3 nm), Co (50 nm)/Cu (5 nm), Co (50 nm)/Cu (10 nm), Co (50 nm)/Cu (18 nm), and Co (50 nm)/Cu (30 nm) multilayered nanowire arrays under applied magnetic field parallel to the nanowires. (f) The relationship between the CPP-GMR ratio and different thicknesses of the Cu layer of the Co/Cu multilayered nanowire arrays under magnetic field parallel to the nanowires.



(a)



(b)

FIGURE 6: Magnetic hysteresis loops of Co/Cu nanowires with Co (50 nm)/Cu (5 nm) of different period numbers and the evolution of the coercivity (H_c) and remanence ratio (M_r/M_s) with the change of period number under the applied magnetic field parallel to the nanowires.

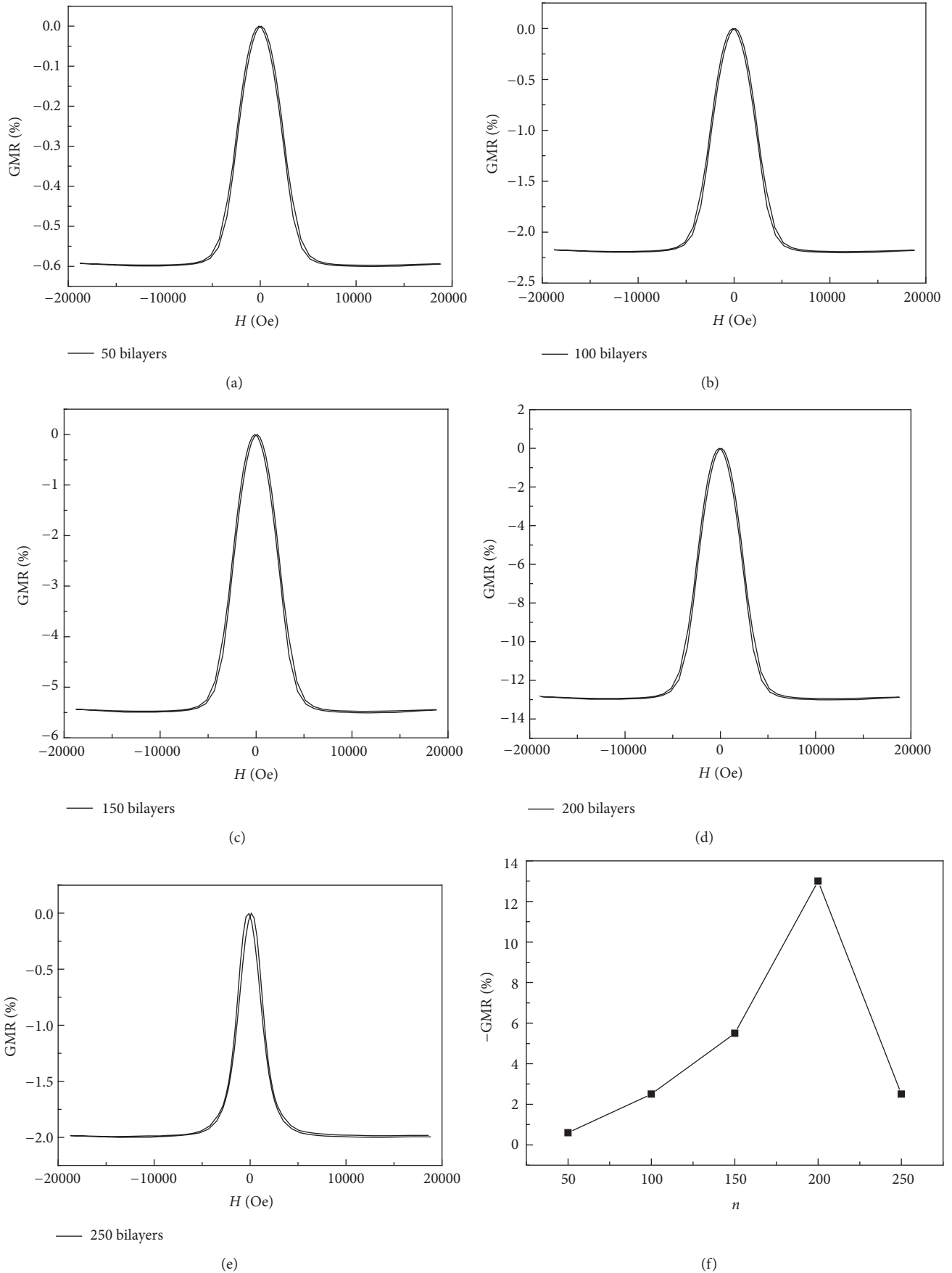


FIGURE 7: (a)–(e) The CPP-GMR curves of Co (50 nm)/Cu (5 nm) with the repeat period number varied from 50 to 250. (f) The relationship between the CPP-GMR ratio and the number of bilayers of the Co/Cu multilayered nanowires electrodeposited into PAA templates.

properties of multilayered nanowire arrays. The coercivity and remanence ratio increase first and then gradually tend to be stable with the increase of the length of the Cu and the period number. The result of CPP-GMR indicates an oscillatory behavior with the varying thickness of Cu layer. The best multilayered nanowire array structure was obtained in Co (50 nm)/Cu (5 nm) ($n = 200$) and the maximum CPP-GMR value can reach -13% at room temperature. This study is of vital importance to the potential applications in the fields of nanodevices and is helpful to provide more in-depth understanding of the magnetic properties of the multilayered nanowire arrays.

Competing Interests

The authors declare that there are no competing interests regarding the publication of this paper.

Acknowledgments

The work is financially supported by the National High Technology Research and Development Program of China (863 Program, no. 2014AA032904), NSFC (nos. 51571136, 61434002), and Shanxi Scholarship Council of China (2015-069).

References

- [1] M. N. Baibich, J. M. Broto, A. Fert et al., "Giant magnetoresistance of (001)Fe/(001)Cr magnetic superlattices," *Physical Review Letters*, vol. 61, no. 21, pp. 2472–2475, 1988.
- [2] G. Binasch, P. Grünberg, F. Saurenbach, and W. Zinn, "Enhanced magnetoresistance in layered magnetic structures with antiferromagnetic interlayer exchange," *Physical Review B*, vol. 39, no. 7, pp. 4828–4830, 1989.
- [3] A. Fert and L. Piraux, "Magnetic nanowires," *Journal of Magnetism and Magnetic Materials*, vol. 200, no. 1, pp. 338–358, 1999.
- [4] I. Bakonyi and L. Péter, "Electrodeposited multilayer films with giant magnetoresistance (GMR): progress and problems," *Progress in Materials Science*, vol. 55, no. 3, pp. 107–245, 2010.
- [5] D. K. Pandya, P. Gupta, S. C. Kashyap, and S. Chaudhary, "Electrodeposition and characterization of Cu/Co multilayers: effect of individual Co and Cu layers on GMR magnitude and behavior," *Journal of Magnetism & Magnetic Materials*, vol. 321, no. 8, pp. 974–978, 2009.
- [6] L. Piraux, J. M. George, J. F. Despres et al., "Giant magnetoresistance in magnetic multilayered nanowires," *Applied Physics Letters*, vol. 65, no. 19, pp. 2484–2486, 1994.
- [7] K. Liu, K. Nagodawithana, P. C. Searson, and C. L. Chien, "Perpendicular giant magnetoresistance of multilayered Co/Cu nanowires," *Physical Review B*, vol. 51, no. 11, pp. 7381–7384, 1995.
- [8] K. Yakushiji, K. Saito, S. Mitani, K. Takanashi, Y. K. Takahashi, and K. Hono, "Current-perpendicular-to-plane magnetoresistance in epitaxial $\text{Co}_2\text{MnSi}/\text{Cr}/\text{Co}_2\text{MnSi}$ trilayers," *Applied Physics Letters*, vol. 88, no. 22, Article ID 222504, pp. 222–504, 2006.
- [9] X.-T. Tang, G.-C. Wang, and M. Shima, "Layer thickness dependence of CPP giant magnetoresistance in individual CoNi/Cu multilayer nanowires grown by electrodeposition," *Physical Review B*, vol. 75, no. 13, Article ID 134404, 2007.
- [10] S. M. S. I. Dulal and E. A. Charles, "Effect of interface number on giant magnetoresistance," *Journal of Physics and Chemistry of Solids*, vol. 71, no. 3, pp. 309–313, 2010.
- [11] T. Ono, Y. Sugita, K. Shigeto, K. Mibu, N. Hosoi, and T. Shinjo, "Magnetoresistance study of Co/Cu/NiFe/Cu multilayers prepared on V-groove substrates," *Physical Review B*, vol. 55, no. 21, pp. 14457–14466, 1997.
- [12] D. Serrate, J. M. De Teresa, P. A. Algarabel, M. R. Ibarra, and J. Galibert, "Intergrain magnetoresistance up to 50 T in the half-metallic $(\text{Ba}_{0.8}\text{Sr}_{0.2})_2\text{FeMoO}_6$ double perovskite: spin-glass behavior of the grain boundary," *Physical Review B*, vol. 71, no. 10, Article ID 104409, 2005.
- [13] A. Paul, T. Damm, D. E. Bürgler, S. Stein, H. Kohlstedt, and P. Grünberg, "Optimizing the giant magnetoresistance of NiFe/Cu/Co pseudo spin-valves prepared by magnetron sputtering," *Applied Physics Letters*, vol. 82, no. 12, pp. 1905–1907, 2003.
- [14] D. Lottis, A. Fert, R. Morel et al., "Magnetoresistance in rf-sputtered (NiFe/Cu/Co/Cu) spin-valve multilayers," *Journal of Applied Physics*, vol. 73, no. 10, pp. 5515–5517, 1993.
- [15] X. Huang, L. Tan, H. Cho, and B. J. H. Stadler, "Magnetoresistance and spin transfer torque in electrodeposited Co/Cu multilayered nanowire arrays with small diameters," *Journal of Applied Physics*, vol. 105, no. 7, Article ID 07D128, 2009.
- [16] S. Hernández, L. Tan, B. J. H. Stadler, and R. H. Victora, "Micromagnetic calculation of spin transfer torque in Co/Cu multilayer nanowires," *Journal of Applied Physics*, vol. 109, no. 7, Article ID 07C916, 2011.
- [17] L. Tan and B. J. H. Stadler, "Fabrication and magnetic behavior of Co/Cu multilayered nanowires," *Journal of Materials Research*, vol. 21, no. 11, pp. 2870–2875, 2006.
- [18] S. Hernández, L. Tan, B. J. H. Stadler, and R. H. Victora, "Micromagnetic calculation of spin transfer torque in Co/Cu multilayer nanowires," *Journal of Applied Physics*, vol. 109, no. 7, Article ID 07C916, 2011.
- [19] S. S. P. Parkin, N. More, and K. P. Roche, "Oscillations in exchange coupling and magnetoresistance in metallic superlattice structures: Co/Ru, Co/Cr, and Fe/Cr," *Physical Review Letters*, vol. 64, no. 19, pp. 2304–2307, 1990.
- [20] Y. Xu, D. Ephron, and M. R. Beasley, "Directed inelastic hopping of electrons through metal-insulator-metal tunnel junctions," *Physical Review B*, vol. 52, no. 4, pp. 2843–2859, 1995.
- [21] S.-S. Yan, J. Du, J. L. Weston, G. Zangari, and J. A. Barnard, "Modulated magnetic properties of hard/soft exchange-coupled SmFe/NiFe multilayers," *Journal of Magnetism and Magnetic Materials*, vol. 231, no. 2-3, pp. 241–245, 2001.

Research Article

Ultrasensitive Anomalous Hall Effect in Ta/CoFe/Oxide/Ta Multilayers

Guang Yang, Yongye Li, Xi Chen, Jingyan Zhang, and Guanghua Yu

Department of Materials Physics and Chemistry, University of Science and Technology Beijing, Beijing 100083, China

Correspondence should be addressed to Guanghua Yu; ghyu@mater.ustb.edu.cn

Received 6 October 2016; Accepted 22 November 2016

Academic Editor: Hao Zeng

Copyright © 2016 Guang Yang et al. This is an open access article distributed under the Creative Commons Attribution License, which permits unrestricted use, distribution, and reproduction in any medium, provided the original work is properly cited.

Ultrahigh anomalous Hall sensitivity has been demonstrated in Ta/CoFe/Oxide/Ta multilayers. By changing oxides (MgO and HfO₂) and annealing temperature, different annealing dependence of sensitivity was found in MgO-sample and HfO₂-sample. For the MgO-sample, the anomalous Hall sensitivity reaches 18792 Ω/T in the as-deposited state and significantly reduces as annealing temperature increases. On the contrary, the sensitivity of the as-deposited HfO₂-sample is only 765 Ω/T, while it remarkably increases with annealing temperature increasing, finally reaching 14741 Ω/T at 240°C. The opposite variation of anomalous sensitivity in two samples originates from the different change of magnetic anisotropy and anomalous Hall resistance during the annealing process. Our study provides a new perspective that both the choice of oxide material and the optimization of annealing treatment are important to the anomalous Hall sensitivity.

1. Introduction

Magnetic sensors are playing an increasing important role in daily life and industrial production, with their wide applications ranging from read heads in the hard disk [1], to the speed and rotation angle detectors in the automotive industry [2], and even to the detection of DNA and proteins [3]. The current design of magnetic sensors is based on the Hall effect in semiconductor materials or magnetoresistive effect including anisotropy magnetoresistance (AMR), giant magnetoresistance (GMR), and tunneling magnetoresistance (TMR) in magnetic materials. However, the sensors based on Hall effect and AMR effect always suffer a lower sensitivity. On the other hand, although high sensitivity can be obtained in GMR- and TMR-based sensors, the complex fabrication process with higher costs is also an obstacle. Recently, the anomalous Hall effect (AHE) of ferromagnets has attracted enormous attention owing to the abundant physics [4, 5] and potential applications [6, 7]. In 2007, Zhu and Cai [8] first demonstrated an anomalous Hall sensitivity as high as 1200 Ω/T in [CoFe/Pt]_n multilayers, which is better than the conventional semiconductor Hall sensitivity (about 1000 Ω/T). Subsequently, the strategy adapted to achieve a higher sensitivity was by using ultrathin ferromagnetic

films/multilayers with enhanced spin-orbit scattering and tailored magnetic anisotropy that enables large anomalous Hall resistance and low saturation field [9–13]. In particular, Lu et al. [11] obtained a sensitivity of 12000 Ω/T in SiO₂/FePt/SiO₂ sandwich structure films with optimized FePt composition and thickness. Zhu et al. [12] demonstrated a sensitivity of 23760 Ω/T in MgO/CoFeB/Ta/MgO multilayers by tuning the thickness of CoFeB and adjacent Ta layer. More excitingly, a very recent study has reported the anomalous Hall sensitivity up to 10⁶ Ω/T, which is two orders higher than the best of semiconductors [13].

Although the achieved ultrahigh sensitivity is remarkable, the compatibility between AHE materials and CMOS technology still needs further consideration. For example, heavy metals such as Pt are always used in AHE materials to enhance the spin-orbit scattering for a large anomalous Hall resistance, while it will cause a terrible shunting effect as well as increased costs. The CoFeB/MgO heterostructure seems a more promising material system, while the commonly used oxides in CMOS technology are high-*k* materials such as SiO₂ and HfO₂. From the application point of view, it is better to introduce the same high-*k* oxides into the AHE materials. Last but not least, AHE materials generally need

additional annealing to exhibit a high sensitivity. Considering the postannealing is also essential to CMOS technology, it is necessary to further optimize the annealing process.

In this work, we demonstrate the ultrasensitive AHE in Ta/CoFe/Oxide/Ta multilayers. By changing oxides (MgO and HfO₂) and annealing temperature (T_a), opposite T_a dependence of sensitivity was found in MgO-sample and HfO₂-sample. For the MgO-sample, the anomalous Hall sensitivity reaches 18792 Ω/T in the as-deposited state and significantly reduces as T_a increases. On the contrary, the sensitivity of the as-deposited HfO₂-sample is only 765 Ω/T , while it remarkably increases with T_a increasing, finally reaching 14741 Ω/T at 240°C. Based on the angular dependent ferromagnetic resonance (FMR) measurements and temperature dependent transport measurements, the different change of sensitivity in two samples comes from the different temperature dependence of the anomalous Hall resistance and the magnetic anisotropy. This study gives new insights that the choice of oxides and the optimization of T_a are both important to obtain an ultrahigh anomalous Hall sensitivity.

2. Experiments

All samples were deposited on Si substrates by magnetron sputtering at room temperature. The sample structure is Ta(0.8)/Co₂₀Fe₈₀(0.8)/Oxide(0.8)/Ta(1.0) (all in nm), where the oxide is MgO or HfO₂. Thermal annealing was carried out in a vacuum furnace (better than 3×10^{-7} Torr) for 15 min without external magnetic fields. Hall bars were patterned by optical lithography combined with Ar⁺ milling for transport measurements in a physical property measurement system. FMR measurements were performed in an electron spin resonance spectrometer (JEOL ESR FA-200) at X-band (9.0 GHz).

3. Results and Discussions

The anomalous Hall sensitivity is defined as $S = dR_{xy}/dH \approx R_{AH}/H_s$ [12, 14], where H_s is the perpendicular saturation field and R_{AH} is the saturated anomalous Hall resistance that can be obtained via a linear extrapolation of R_{xy} at high field to zero field. The inset of Figure 1 exhibits the anomalous Hall loops of sample Ta(0.8)/Co₂₀Fe₈₀(0.8)/MgO(0.8)/Ta(1.0) (in nm) in the as-deposited and different annealed states, from which the corresponding value of S is calculated. As a result, Figure 1 shows the sensitivity S as a function of the annealing temperature T_a . When T_a is 25°C (as-deposited state), S of MgO-sample has reached 18792 Ω/T . Nevertheless, the value of S decreases significantly with the increase of T_a . When T_a reaches 140°C, the value of S is 8145 Ω/T , decreasing 57% with respect to that in the as-deposited state. As T_a further increases to 240°C, the value of S is only 2572 Ω/T .

In contrast, Figure 2 shows S as a function of T_a for sample Ta(0.8)/Co₂₀Fe₈₀(0.8)/HfO₂(0.8)/Ta(1.0) (in nm). Different from the MgO-sample, the value of S in the as-deposited HfO₂ sample is only 765 Ω/T . When T_a increases to 180°C, the value of S appears almost unchanged. However, as T_a is above 200°C, the value of S increases dramatically. When T_a reaches 240°C, the value of S is 14741 Ω/T , which is about 19

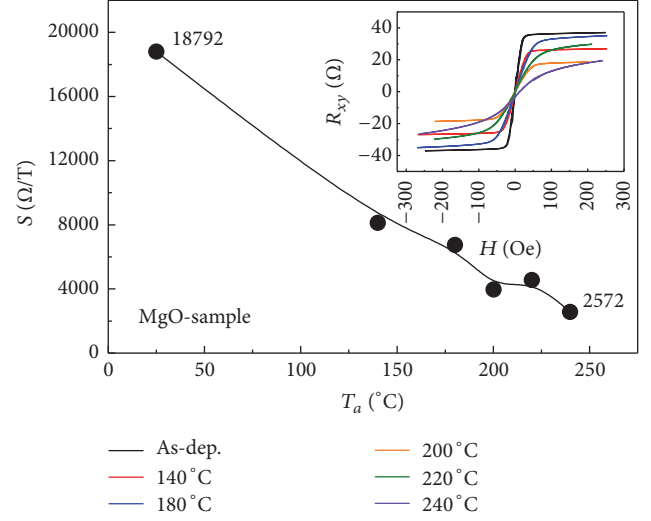


FIGURE 1: Annealing temperature dependence of the anomalous Hall sensitivity for the sample Ta(0.8)/Co₂₀Fe₈₀(0.8)/MgO(0.8)/Ta(1.0) (in nm). Inset: anomalous Hall loops of the sample in the as-deposited and different annealed states.

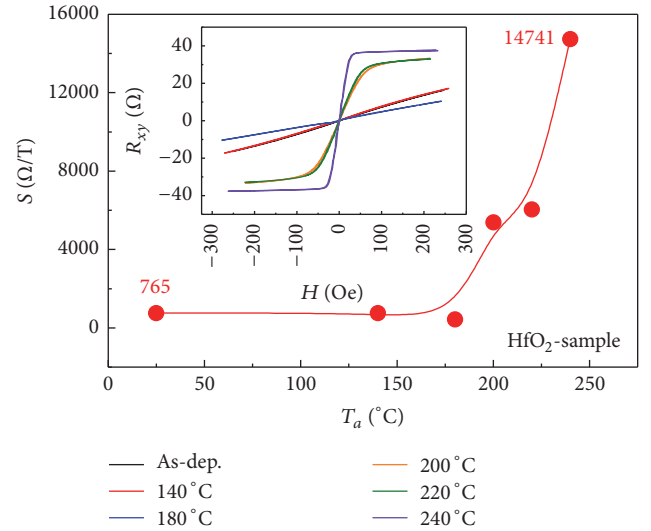


FIGURE 2: Annealing temperature dependence of the anomalous Hall sensitivity for the sample Ta(0.8)/Co₂₀Fe₈₀(0.8)/HfO₂(0.8)/Ta(1.0) (in nm). Inset: anomalous Hall loops of the sample in the as-deposited and different annealed states.

times larger than that in the as-deposited state. It is interesting to find that the variation trend of S with respect to T_a is opposite in the MgO-sample and HfO₂-sample. To further illustrate the difference, four typical samples were chosen as below: as-deposited MgO-sample, 240°C annealed MgO-sample, as-deposited HfO₂-sample, and 240°C annealed HfO₂-sample.

As shown in Figure 3, the detailed R_{xy} - H curves of the above four samples are presented. In Figure 3(a), the curve of the as-deposited MgO-sample (black one) shows an obvious linear response without magnetic hysteresis. The saturated

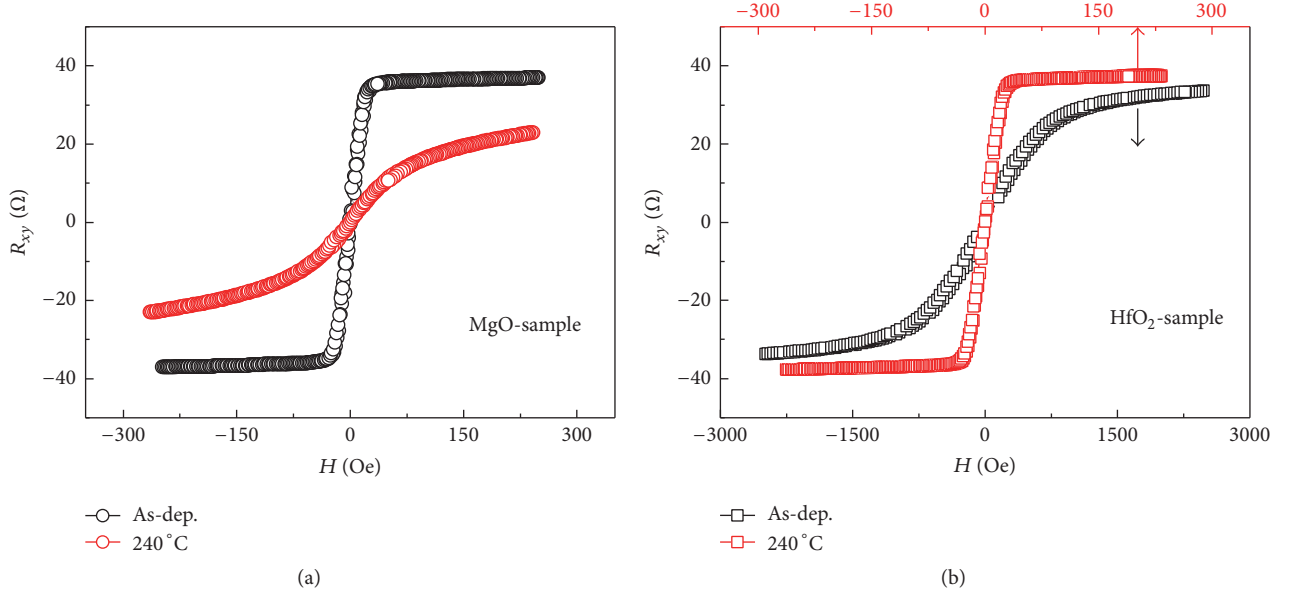


FIGURE 3: (a) R_{xy} - H curves for sample Ta(0.8)/Co₂₀Fe₈₀/MgO(0.8)/Ta(1.0) (in nm) in the as-deposited and 240°C annealed states. (b) R_{xy} - H curves for sample Ta(0.8)/Co₂₀Fe₈₀/HfO₂(0.8)/Ta(1.0) (in nm) in the as-deposited and 240°C annealed states.

anomalous Hall resistance R_{AH} is 35.8 Ω and the perpendicular saturation field H_s is 20 Oe. By annealing at 240°C, the linear shape of the curve began to degrade, with R_{AH} decreasing to 14.2 Ω and H_s increasing to 150 Oe. Both the reduced R_{AH} and the increased H_s are detrimental to the sensitivity, leading to a significant decrease of S from 18792 Ω/T to 2572 Ω/T. Figure 3(b) shows the R_{xy} - H curves of the as-deposited and 240°C annealed HfO₂-samples. The values of R_{AH} and H_s for the as-deposited sample are 28.5 Ω and 1000 Oe. By annealing at 240°C, the value of R_{AH} reaches 36.4 Ω while the value of H_s decreases to 30 Oe. Both the increased R_{AH} and the reduced H_s are beneficial to an ultrahigh sensitivity, leading to a significant increase of S from 765 Ω/T to 14741 Ω/T.

It is well known that the perpendicular saturation field is related to the magnetic anisotropy of the films. During the annealing process, the volume anisotropy as well as the interfacial anisotropy is likely to change [15, 16]. In order to characterize the evolution of magnetic anisotropy in the MgO- and HfO₂-samples, out-of-plane angular dependent FMR measurements were performed. The typical FMR differential absorption spectrum is shown in the inset of Figure 4(a), where the resonance field H_{res} and peak-to-peak linewidth ΔH_{pp} are defined. Figure 4(a) presents the out-of-plane angular dependent H_{res} for the as-deposited MgO-sample. Here, the angle θ_H is defined as the direction of applied magnetic field with respect to the film normal. The value of H_{res} can be fitted by Kittel's formula:

$$f = \frac{\gamma}{2\pi} \sqrt{f_1 f_2} \quad (1)$$

$$= \frac{\gamma}{2\pi} \sqrt{H_{res} \cos(\theta_H - \theta) + H_1 \cos^2 \theta - H_2 \cos^4 \theta} \sqrt{H_{res} \cos(\theta_H - \theta) + H_1 \cos 2\theta + H_2 (3 \cos^2 \theta \sin^2 \theta - \cos^4 \theta)},$$

where $H_1 = 2K_1/M_s + 4K_2/M_s - 4\pi M_s$ and $H_2 = 4K_2/M_s$. K_1 , K_2 , M_s , and θ are the first-order, second-order uniaxial anisotropy constant, the saturation magnetization, and the equilibrium angle of the magnetization vector with respect to film normal, respectively. $f = 9.0$ GHz is the frequency of AC magnetic fields in the machine. γ is the gyromagnetic ratio given as $\gamma = g\mu_B/\hbar$, where g , μ_B , and \hbar are Landé factor, Bohr magneton, and Planck's constant, respectively. As shown in Figure 4(a), the experimental value of H_{res} as a function of θ_H can be well fitted, where above parameters

can be obtained. Consequently, the fitting parameters g , M_s , K_1 , K_2 , the effective magnetic anisotropy constant $K_{eff} = K_1 - 2\pi M_s^2$, and the effective anisotropy field $H_{eff} = 2K_{eff}/M_s$ calculated from Figures 4(a)–4(d) are listed in Table 1.

From Table 1, it is clearly seen that the variation trend of magnetic anisotropy is different in the MgO-sample and HfO₂-sample. For the as-deposited MgO-sample, both values of the effective magnetic anisotropy constant K_{eff} and the second-order uniaxial anisotropy constant K_2 are positive, indicating the sample has perpendicular magnetic anisotropy

TABLE I: Fitting parameters deduced from (1) in the four samples.

	g	M_s ($\times 10^3$ emu/cm 3)	K_1 ($\times 10^6$ erg/cm 3)	K_2 ($\times 10^4$ erg/cm 3)	K_{eff} ($\times 10^5$ erg/cm 3)	H_{eff} (Oe)
MgO as-dep.	2.01	1.13	8.02	8.89	0.53	94.02
MgO 240°C	1.99	1.14	7.76	10.15	-4.09	-716.92
HfO $_2$ as-dep.	2.04	1.14	7.71	2.47	-5.4	-942.60
HfO $_2$ 240°C	2.04	1.12	8.10	1.01	2.07	369.26

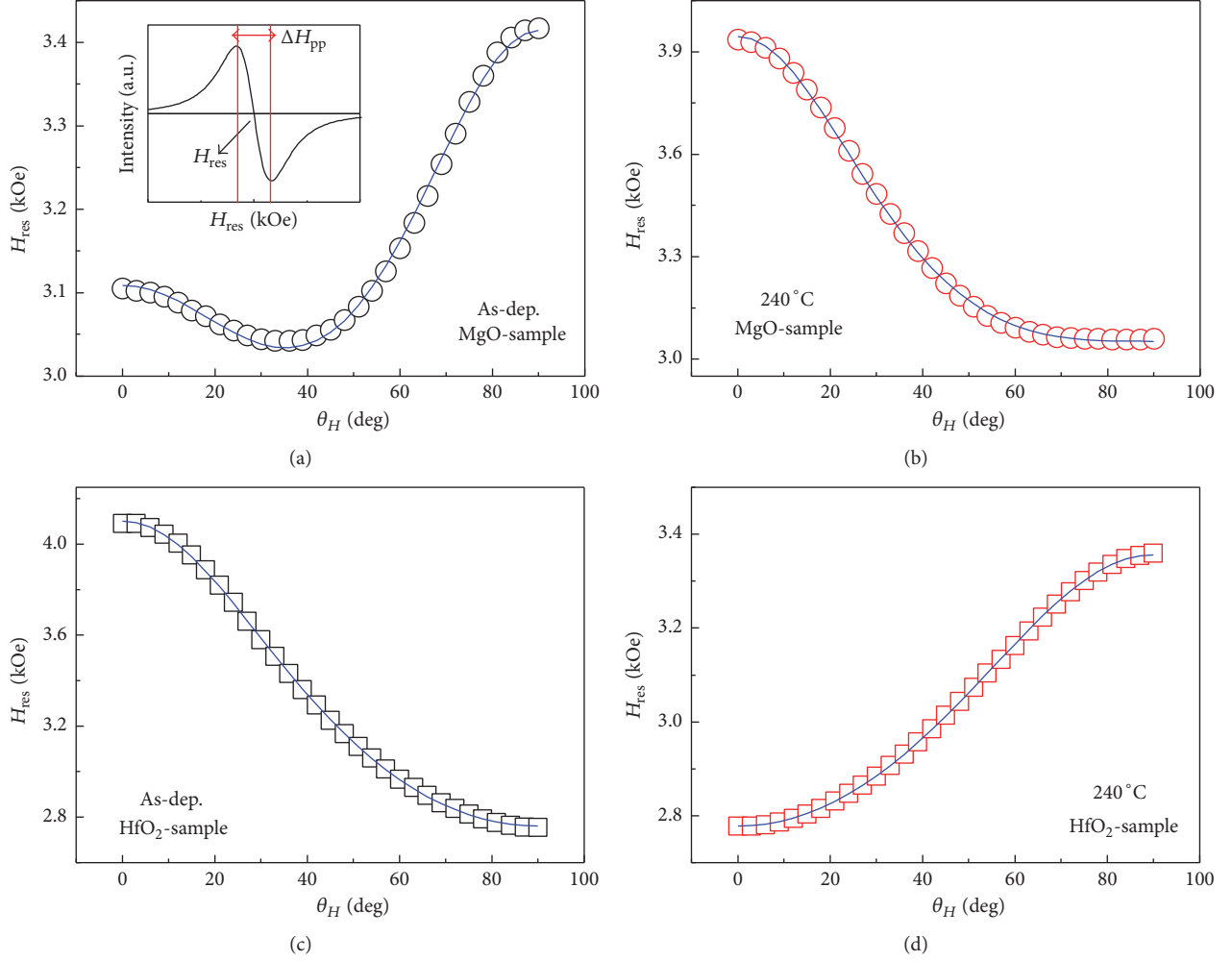


FIGURE 4: (a)-(b) Out-of-plane angular dependent resonance fields H_{res} for sample Ta(0.8)/Co $_{20}$ Fe $_{80}$ (0.8)/MgO(0.8)/Ta(1.0) (in nm) in the as-deposited and 240°C annealed states. Hollow circles and solid lines represent experimental data and theoretical fitting of H_{res} . Inset: typical FMR differential absorption spectra where the resonance field H_{res} and peak-to-peak linewidth ΔH_{pp} are defined. (c)-(d) Out-of-plane angular dependent resonance fields H_{res} for sample Ta(0.8)/Co $_{20}$ Fe $_{80}$ (0.8)/HfO $_2$ (0.8)/Ta(1.0) (in nm) in the as-deposited and 240°C annealed states. Hollow diamonds and solid lines represent experimental data and theoretical fitting of H_{res} .

(PMA) [17]. For the sample with PMA, the perpendicular direction is the easy magnetization axis; thus the perpendicular saturation field H_s is small. It is also important to point out that since the calculated effective anisotropy field H_{eff} is very small (only about 94 Oe), the R_{xy} - H curve will not exhibit the obvious coercivity. For the 240°C annealed MgO-sample, the calculated values of K_{eff} and K_2 are -4.09×10^5 erg/cm 3 and 1.02×10^5 erg/cm 3 , respectively. Considering the value of K_{eff} is negative and $K_2 < -(1/2)K_{\text{eff}}$, the annealed

MgO-sample has in-plane magnetic anisotropy (IMA) [17]. For the sample with IMA, the perpendicular direction is the difficult magnetization axis; thus the value of H_s will be very large. On the other hand, for the as-deposited HfO $_2$ -sample, the value of K_{eff} is negative and $K_2 < -(1/2)K_{\text{eff}}$, representing a typical IMA character. However, by annealing at 240°C, both the values of K_{eff} and K_2 change to positive, indicating the 240°C annealed HfO $_2$ sample has PMA with a small H_s . Therefore, the variation trend of magnetic anisotropy

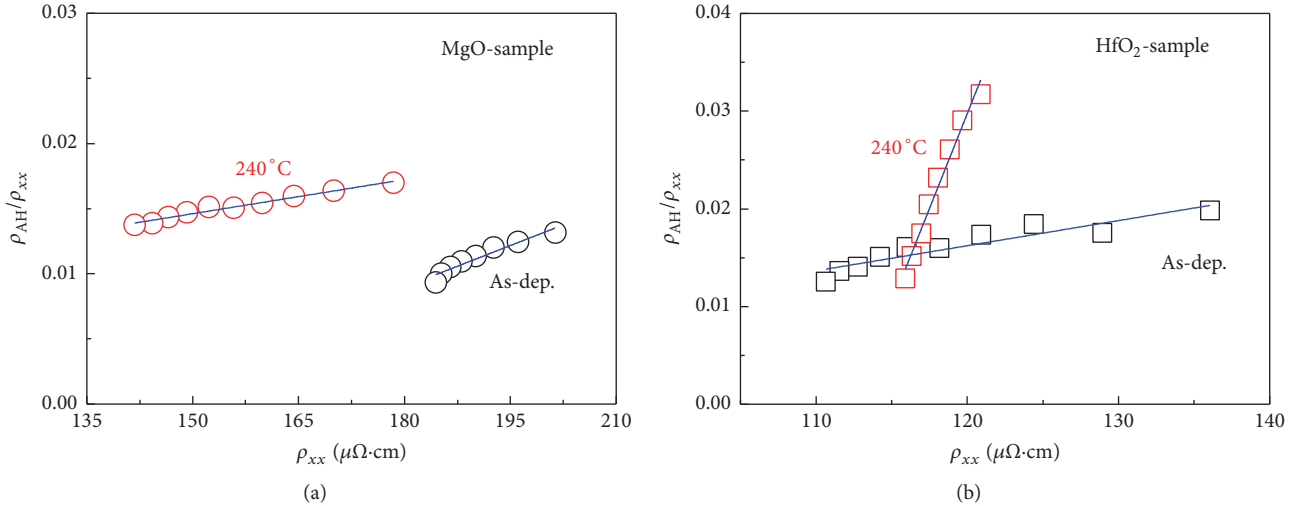


FIGURE 5: (a) ρ_{AH}/ρ_{xx} versus ρ_{xx} for sample Ta(0.8)/Co₂₀Fe₈₀(0.8)/MgO(0.8)/Ta(1.0) (in nm) in the as-deposited and 240 °C annealed states. (b) ρ_{AH}/ρ_{xx} versus ρ_{xx} for sample Ta(0.8)/Co₂₀Fe₈₀(0.8)/HfO₂(0.8)/Ta(1.0) (in nm) in the as-deposited and 240 °C annealed states.

during annealing is opposite in the MgO-sample and HfO₂-sample. For MgO-sample, the magnetic anisotropy changes from PMA to IMA, resulting in a significant increase of H_s , while, for HfO₂-sample, the magnetic anisotropy changes from IMA to PMA, leading to a remarkable decrease of H_s .

For the ferromagnetic metal (FM)/Oxide heterostructures, the interfacial magnetic anisotropy plays a dominated role [16]. In theory, first-principles calculation has been used to study the FM/Oxide interface, showing that the interfacial magnetic anisotropy is strongly affected by the hybridization between FM-3d and O-2p orbitals [18, 19]. In addition, previous researches have reported that the orbital hybridization between FM and oxide is sensitive to the annealing process [20, 21]. By annealing, the activated oxygen atoms could migrate to the interface, producing a bonding between FM atoms and oxygen atoms. It is necessary to point out that the degree of bonding is important to the orbital hybridization, where an optimized bonding is beneficial to PMA, whereas the excessive and insufficient bonding will lead to a degradation of PMA [22]. Here in our samples, the enthalpy of formation (ΔH_f) for MgO is -601.6 kJ/mol, larger than that for HfO₂ (-1144.7 kJ/mol). It means that the combination between Hf and O is more stable than that between Mg and O. Therefore, during the deposition and annealing process, MgO is more likely to deviate the stoichiometric ratio and transfer oxygen atoms to the adjacent CoFe layer, leading to the final difference of the FM-O bonding degree for the two samples. According to our recent work, the oxygen migration direction during annealing process may be inverse at different FM/Oxide interfaces [23]. However, since the oxygen migration could also be affected by the film thickness and annealing temperature and so forth, the specific differences about oxygen migration in the two samples need further investigation.

In addition to H_s , AHE sensitivity is also related to R_{AH} , whose value represents the magnitude of AHE. Previous work has reported that the annealing process will affect the

intrinsic or extrinsic mechanisms, leading to a variation of AHE [24, 25]. To explain the change of R_{AH} in the MgO- and HfO₂-sample as shown in Figure 3, contributions to the AHE by different mechanisms were analyzed. In general, $\rho_{AH} = a\rho_{xx} + b\rho_{xx}^2$, where ρ_{AH} is the saturated anomalous Hall resistivity, ρ_{xx} is the longitudinal resistivity, a represents the skew scattering contribution, and b represents the side jump as well as the intrinsic contribution [26–30]. It is necessary to point out that the thickness change during annealing is eliminated; thus ρ_{AH} is equivalent to R_{AH} . The coefficients a and b can be obtained by plotting ρ_{AH}/ρ_{xx} as a function of ρ_{xx} and linear fitting to the experimental data. Figure 5(a) shows the linear fitting for MgO-sample in the as-deposited and 240 °C annealed states. The values of a and b are -0.029 and $2.12 \times 10^{-4} \mu\Omega^{-1} \text{cm}^{-1}$ in the as-deposited state, respectively. By annealing at 240 °C, the values of a and b change to 0.002 and $8.74 \times 10^{-5} \mu\Omega^{-1} \text{cm}^{-1}$, respectively. Although the sign of a alters from negative to positive, both the values of $|a|$ and $|b|$ decrease by one order of magnitude, finally weakening the AHE. For the HfO₂-sample, the values of a and b are -0.015 and $2.57 \times 10^{-4} \mu\Omega^{-1} \text{cm}^{-1}$ in the as-deposited state, respectively. By annealing at 240 °C, both the values of $|a|$ and $|b|$ increase by one order of magnitude, reaching -0.437 and $3.89 \times 10^{-3} \mu\Omega^{-1} \text{cm}^{-1}$, respectively. The competitive relation between a and b will affect not only the value but also the sign of ρ_{AH} . Considering the large enhancement of $|b|$ as well as the same positive sign between b and ρ_{AH} , it suggests that the influence of b on AHE is improved during annealing process for the HfO₂-sample. Above analysis gives strong evidence that the variation trend of AHE is different during the annealing process in the MgO- and HfO₂-sample. For the MgO-sample, both the intrinsic and extrinsic contributions to AHE are weakened by annealing, resulting in the significant decrease of R_{AH} as shown in Figure 3(a). In contrast, the side jump and the intrinsic contributions are remarkably enhanced, leading to the final increase of R_{AH} as shown in Figure 3(b).

4. Conclusions

In conclusion, the ultrasensitive AHE was demonstrated in Ta/CoFe/Oxide/Ta multilayers. For sample Ta/CoFe/MgO/Ta, AHE sensitivity is as high as $18792 \Omega/T$ in the as-deposited state, while the value decreases significantly as the annealing temperature increases. For sample Ta/CoFe/HfO₂/Ta, the value of sensitivity is small in the as-deposited state but increases to $14741 \Omega/T$ by 240°C annealing. The opposite variation of AHE sensitivity in two samples originates from the different change of magnetic anisotropy and anomalous Hall resistance during the annealing process. This work gives new insights that both the choice of oxide material and the optimization of annealing treatment play an important role in the anomalous Hall sensitivity.

Competing Interests

The authors declare that there is no conflict of interests regarding the publication of this paper.

Acknowledgments

This work was supported by the National Basic Research Program of China (2015CB921502) and the Natural Science Foundation of China (51331002, 51371027, and 11504019).

References

- [1] J. M. Daughton, "GMR and SDT sensor applications," *IEEE Transactions on Magnetics*, vol. 36, no. 5, pp. 2773–2778, 2000.
- [2] C. P. O. Treutler, "Magnetic sensors for automotive applications," *Sensors and Actuators, A: Physical*, vol. 91, no. 1-2, pp. 2–6, 2001.
- [3] S. G. Grancharov, H. Zeng, S. Sun et al., "Bio-functionalization of monodisperse magnetic nanoparticles and their use as biomolecular labels in a magnetic tunnel junction based sensor," *The Journal of Physical Chemistry B*, vol. 109, no. 26, pp. 13030–13035, 2005.
- [4] N. Nagaosa, J. Sinova, S. Onoda, A. H. MacDonald, and N. P. Ong, "Anomalous Hall effect," *Reviews of Modern Physics*, vol. 82, no. 2, pp. 1539–1592, 2010.
- [5] Y. Tian, L. Ye, and X. Jin, "Proper scaling of the anomalous hall effect," *Physical Review Letters*, vol. 103, no. 8, Article ID 087206, 2009.
- [6] J. Moritz, B. Rodmacq, S. Auffret, and B. Dieny, "Extraordinary Hall effect in thin magnetic films and its potential for sensors, memories and magnetic logic applications," *Journal of Physics D: Applied Physics*, vol. 41, no. 13, Article ID 135001, 2008.
- [7] A. Gerber, "Towards Hall effect spintronics," *Journal of Magnetism and Magnetic Materials*, vol. 310, no. 2, pp. 2749–2751, 2007.
- [8] Y. Zhu and J. W. Cai, "Ultrahigh sensitivity Hall effect in magnetic multilayers," *Applied Physics Letters*, vol. 90, no. 1, Article ID 012104, 2007.
- [9] S. L. Zhang, J. Teng, J. Y. Zhang et al., "Large enhancement of the anomalous Hall effect in Co/Pt multilayers sandwiched by MgO layers," *Applied Physics Letters*, vol. 97, no. 22, Article ID 222504, 2010.
- [10] J. Zhang, G. Yang, S. Wang et al., "Ultrahigh anomalous hall sensitivity in Co/Pt multilayers by interfacial modification," *Applied Physics Express*, vol. 6, no. 10, Article ID 103007, 2013.
- [11] Y. M. Lu, J. W. Cai, H. Y. Pan, and L. Sun, "Ultrasensitive anomalous Hall effect in SiO₂/Fe-Pt/SiO₂ sandwich structure films," *Applied Physics Letters*, vol. 100, no. 2, Article ID 022404, 2012.
- [12] T. Zhu, P. Chen, Q. H. Zhang, R. C. Yu, and B. G. Liu, "Giant linear anomalous Hall effect in the perpendicular CoFeB thin films," *Applied Physics Letters*, vol. 104, no. 20, Article ID 202404, 2014.
- [13] G. Kopnov and A. Gerber, "MegaOhm extraordinary Hall effect in oxidized CoFeB," *Applied Physics Letters*, vol. 109, no. 2, Article ID 022404, 2016.
- [14] G. X. Miao and G. Xiao, "Giant Hall resistance in Pt-based ferromagnetic alloys," *Applied Physics Letters*, vol. 85, no. 1, pp. 73–75, 2004.
- [15] T. Maeda, T. Kai, A. Kikitsu, T. Nagase, and J.-I. Akiyama, "Reduction of ordering temperature of an FePt-ordered alloy by addition of Cu," *Applied Physics Letters*, vol. 80, no. 12, pp. 2147–2149, 2002.
- [16] S. Ikeda, K. Miura, H. Yamamoto et al., "A perpendicular-anisotropy CoFeB–MgO magnetic tunnel junction," *Nature Materials*, vol. 9, no. 9, pp. 721–724, 2010.
- [17] E. Y. Vedmedenko, H. P. Oepen, and J. Kirschner, "Microstructure of the spin reorientation transition in second-order approximation of magnetic anisotropy," *Physical Review B*, vol. 66, no. 21, Article ID 214401, 2002.
- [18] H. X. Yang, M. Chshiev, B. Dieny, J. H. Lee, A. Manchon, and K. H. Shin, "First-principles investigation of the very large perpendicular magnetic anisotropy at Fe–MgO and Co–MgO interfaces," *Physical Review B*, vol. 84, no. 5, Article ID 054401, 2011.
- [19] K. H. Khoo, G. Wu, M. H. Jhon et al., "First-principles study of perpendicular magnetic anisotropy in CoFe/MgO and CoFe/Mg₃B₂O₆ interfaces," *Physical Review B*, vol. 87, no. 17, Article ID 174403, 2013.
- [20] X. Chen, C. Feng, Z. Long Wu et al., "Interfacial oxygen migration and its effect on the magnetic anisotropy in Pt/Co/MgO/Pt films," *Applied Physics Letters*, vol. 104, no. 5, Article ID 052413, 2014.
- [21] G. Yang, J.-Y. Zhang, S.-G. Wang et al., "Magnetization reorientation induced by interfacial structures in ultrathin disordered FePt film sandwiched by SiO₂ layers," *Applied Surface Science*, vol. 353, pp. 489–493, 2015.
- [22] A. Manchon, C. Ducruet, L. Lombard et al., "Analysis of oxygen induced anisotropy crossover in Pt/Co/MOx trilayers," *Journal of Applied Physics*, vol. 104, no. 4, Article ID 043914, 2008.
- [23] G. Yang, J.-Y. Zhang, S.-L. Jiang et al., "Effect of oxygen migration on magnetic anisotropy and damping constant in perpendicular Ta/CoFeB/Gd/MgO/Ta multilayers," *Applied Surface Science*, 2016.
- [24] S.-L. Jiang, X. Chen, X.-J. Li et al., "Anomalous Hall effect engineering via interface modification in Co/Pt multilayers," *Applied Physics Letters*, vol. 107, no. 11, Article ID 112404, 2015.
- [25] S.-L. Jiang, G. Yang, J. Teng, Q.-X. Guo, L.-L. Li, and G.-H. Yu, "Interface-engineered spin-dependent transport in perpendicular Co/Pt multilayers," *Applied Surface Science*, vol. 387, pp. 375–378, 2016.
- [26] M.-C. Chang and Q. Niu, "Berry phase, hyperorbits, and the Hofstadter spectrum: semiclassical dynamics in magnetic Bloch bands," *Physical Review B - Condensed Matter and Materials Physics*, vol. 53, no. 11, pp. 7010–7023, 1996.

- [27] D. Hou, Y. Li, D. Wei, D. Tian, L. Wu, and X. Jin, "The anomalous Hall effect in epitaxial face-centered-cubic cobalt films," *Journal of Physics Condensed Matter*, vol. 24, no. 48, Article ID 482001, 2012.
- [28] J. Smit, "The spontaneous hall effect in ferromagnetics II," *Physica*, vol. 24, no. 1-5, pp. 39-51, 1958.
- [29] L. Berger, "Side-jump mechanism for the hall effect of ferromagnets," *Physical Review B*, vol. 2, no. 11, pp. 4559-4566, 1970.
- [30] A. Crépieux and P. Bruno, "Theory of the anomalous hall effect from the Kubo formula and the Dirac equation," *Physical Review B*, vol. 64, no. 1, Article ID 014416, 2001.

Research Article

High Field Linear Magnetoresistance Sensors with Perpendicular Anisotropy $L1_0$ -FePt Reference Layer

X. Liu, Z. L. Song, R. Wang, and Z. Y. Quan

Key Laboratory of Magnetic Molecules and Magnetic Information Materials of Ministry of Education and School of Chemistry and Materials Science, Shanxi Normal University, Linfen 041004, China

Correspondence should be addressed to Z. Y. Quan; quanzy@sxnu.edu.cn

Received 27 August 2016; Accepted 12 October 2016

Academic Editor: Xiangshui Miao

Copyright © 2016 X. Liu et al. This is an open access article distributed under the Creative Commons Attribution License, which permits unrestricted use, distribution, and reproduction in any medium, provided the original work is properly cited.

High field linear magnetoresistance is an important feature for magnetic sensors applied in magnetic levitating train and high field positioning measurements. Here, we investigate linear magnetoresistance in Pt/FePt/ZnO/Fe/Pt multilayer magnetic sensor, where FePt and Fe ferromagnetic layers exhibit out-of-plane and in-plane magnetic anisotropy, respectively. Perpendicular anisotropy $L1_0$ -FePt reference layer with large coercivity and high squareness ratio was obtained by in situ substrate heating. Linear magnetoresistance is observed in this sensor in a large range between +5 kOe and -5 kOe with the current parallel to the film plane. This $L1_0$ -FePt based sensor is significant for the expansion of linear range and the simplification of preparation for future high field magnetic sensors.

1. Introduction

Research on spintronics is fast developing due to its widely practical application [1–4]. Magnetic tunnel junctions and magnetic spin valves as the important contents in spintronics are popularly used as magnetic sensors, such as magnetic read heads for hard-disk drive, position, and speed detectors in low magnetic field measurement [5, 6]. In general, the majority of the linear magnetic sensors are based on Hall effect or anisotropic magnetoresistance (AMR) with some shortcomings of poor thermal stability and limited operation frequency range [7]. Recently, the linear giant magnetoresistance (GMR) and tunneling magnetoresistance (TMR) sensors, in which a linear response can be achieved by applying a bias field [8], using a shape anisotropy of the free layer [9], or introducing a pinned layer [10], were proposed as promising candidates due to their high field sensitivity and good thermal stability [11–13]. Particularly, in some applications such as magnetic levitating train and high field positioning measurements, the high field linear magnetoresistance (MR) sensors are investigated due to high sensing field and fine repeatability [14, 15]. An approach of making a high field linear magnetic field response is to use a sandwich structure with a reference layer having high perpendicular magnetic anisotropy and

an in-plane anisotropy free layer [16–19]. However some problems such as narrow linear range and complicated design are still unresolved.

In this work, we design and fabricate $L1_0$ -FePt/ZnO/Fe multilayer films to shed light on this problem by choosing perpendicular anisotropy $L1_0$ -FePt with a large coercive force (H_c) and a high squareness ratio as the reference layer. The MR curve is nearly linear when the applied field is in the range ± 5 kOe measured at 300 K, which is improved greatly compared to previously reported results [18]. Meanwhile, this design simplifies effectively the structure of linear magnetic sensors through applying $L1_0$ -FePt with a large H_c as reference layer.

2. Experimental

Multilayer films with a structure of Pt(4)/FePt(15)/ZnO(5)/Fe(5)/Pt(3) (thicknesses in nm) were prepared on single crystal MgO (001) substrates by magnetron sputtering system as shown schematically in Figure 1(a). A high field linear MR sensor is designed using a perpendicular anisotropy $L1_0$ -FePt reference layer and in-plane anisotropy Fe free layer separated by a ZnO barrier layer in the magnetic multilayers as shown in Figure 1(b). Here the free and reference layers

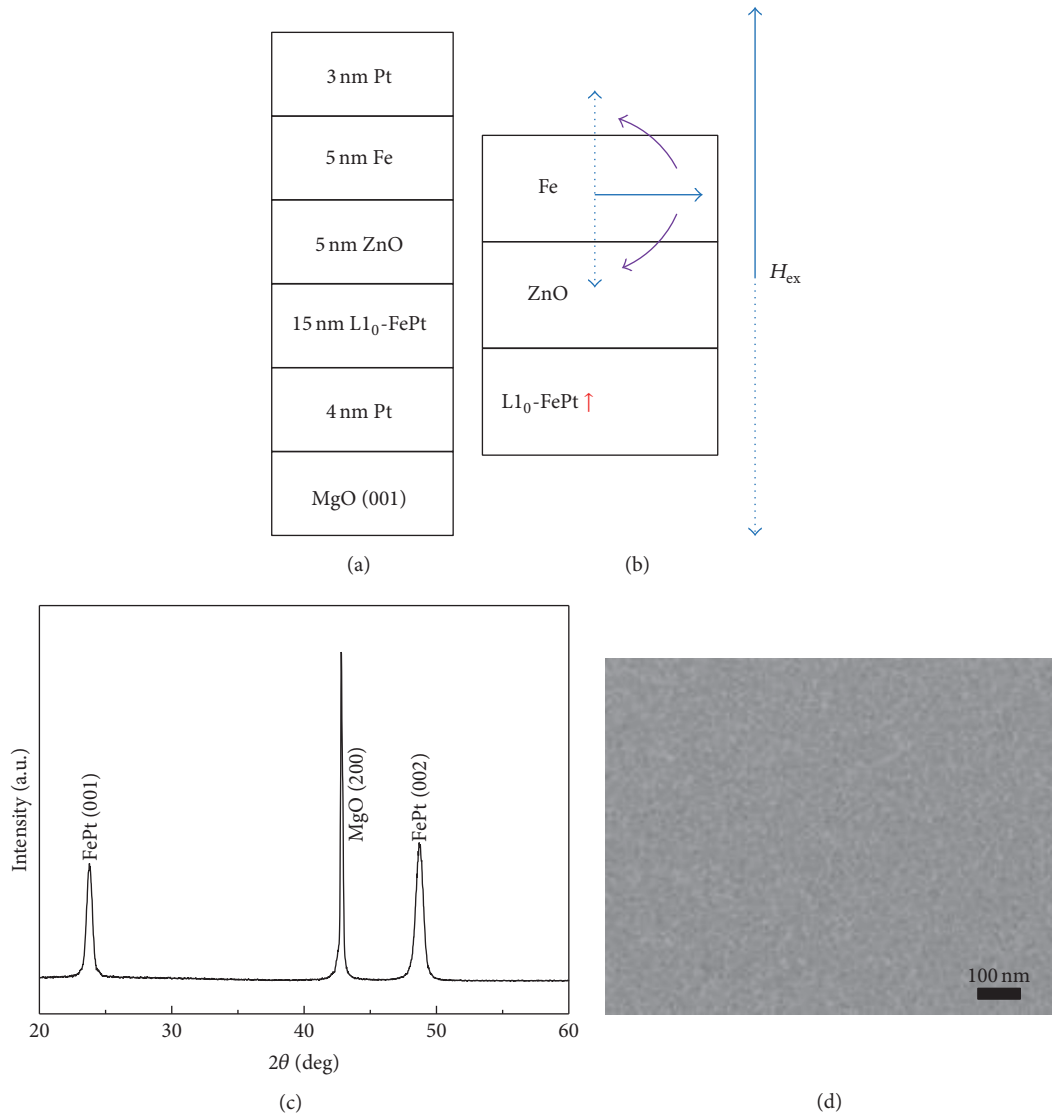


FIGURE 1: (a) Schematics of the Pt(4)/FePt(15)/ZnO(5)/Fe(5)/Pt(3) multilayers on MgO substrate; (b) the core sandwich schematic diagram of L₁₀-FePt/ZnO/Fe. The magnetization directions are marked by arrows, and the applied external magnetic field is perpendicular to the film plane; (c) XRD spectra of the Pt(4)/L₁₀-FePt(15) bilayer films; (d) SEM image of the Pt(4)/L₁₀-FePt(15) bilayer film surface.

are perpendicular to each other. With the increase of external magnetic field (H_{ex}), the free layer's magnetization rotates until becoming perpendicular to the film plane. And a reversible linear MR response in a large range of magnetic field was expected.

The pressure of high-purity argon was 2.0 Pa during sputtering. The Pt and FePt layers were deposited at an in situ temperature of 450°C followed by annealing for 2 h at 450°C. Then the ZnO, Fe, and Pt layers were successively deposited at the room temperature after the deposition of FePt layer. The FePt film was manufactured by cosputtering an Fe target and a Pt target, whose deposition rates were calibrated to achieve Fe₅₅Pt₄₅. The base vacuum was under 8.0×10^{-5} Pa. The crystalline structures and microstructure of multilayer films were characterized by means of X-ray diffraction (XRD) and

transmission electron microscope (TEM). The morphologies of the samples were observed by scanning electron microscopy (SEM). The magnetic properties of films were determined using a superconduction quantum inference device (SQUID) and a vibrating sample magnetometer (VSM). The magnetic field dependence of MR was measured using a four-point method with current-in-plane (CIP) and applied field perpendicular to plane using a Keithley 2400 source meter and Keithley 2182 nanovolt meter in a physical property measurement system (PPMS, Quantum Design Inc.).

3. Results and Discussion

XRD pattern of the thin film with Pt/L₁₀-FePt bilayers is shown in Figure 1(c). The peaks of (001) and (002) were

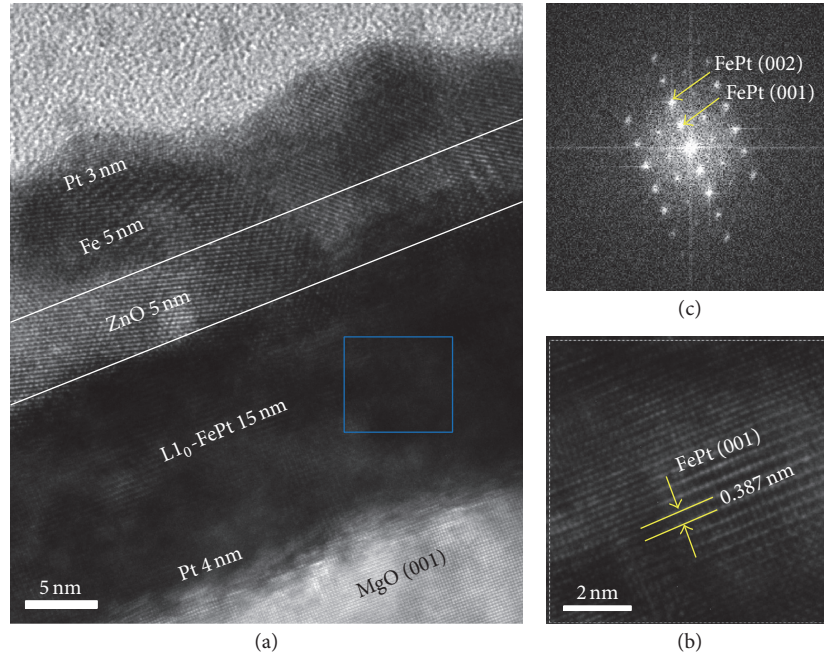


FIGURE 2: TEM analysis of the Pt(4)/FePt(15)/ZnO(5)/Fe(5)/Pt(3) multilayers. (a) The cross section TEM image. (b) The HRTEM image. (c) Its corresponding FFT image.

observed for FePt film, indicating formation of the $L1_0$ ordered phase with easy axis perpendicular to the substrate surface. Thus, the transformation of FePt film from face-centered cubic (fcc) phase to face-centered tetragonal (fct) phase was fulfilled by in situ substrate heating. The SEM image shows that the deposited Pt/ $L1_0$ -FePt bilayer surface is continuous and smooth (see Figure 1(d)). The lattice misfit between FePt (001) and MgO (001) is 8.8% [20]; the FePt film received tensile stress along the in-plane direction, which causes the film tend to form granular film [21]. Whereas the mismatch value is 1.8% between Pt (001) and MgO (001) [22], the Pt buffer layer deposited between MgO substrate and FePt film effectively reduces the stress, causing the forming of a continuous film.

In order to reflect the structure information of the multilayers more accurately, we carried out the cross section TEM image and high-resolution TEM (HRTEM) image of the Pt(4)/FePt(15)/ZnO(5)/Fe(5)/Pt(3) multilayer sensor. The result present that the films are continuous as shown in Figure 2(a). The structure of the multilayer films is consistent with the schematic structure in Figure 1(a). From the HRTEM image shown in Figure 2(b), the lattice fringe spacing is measured to be 0.387 nm, corresponding to the $d_{\text{FePt}(001)}$ (0.384 nm) of $L1_0$ -FePt phase [23]. Also, the FePt (001) and FePt (002) can be found obviously from its fast Fourier transform (FFT) image in Figure 2(c), suggesting that $L1_0$ ordered phase of FePt was obtained in our films.

Figure 3(a) shows the magnetic hysteresis loops of Pt(4)/FePt(15) films deposited in situ substrate heating at 450°C. The coercivity (H_c) of out-of-plane and in-plane films is

7 kOe and 4 kOe, respectively. The remanence (M_r) of out-of-plane and in-plane direction is 610 emu/cm³ and 176 emu/cm³, respectively. The squareness ratios (M_r/M_s) of in-plane and out-of-plane are about 0.5 and 0.9, respectively. These data indicate the preferred alignment of the easy magnetization axis along the out-of-plane direction, which agrees with the result of Figure 1(c). It should be mentioned that the saturation magnetization (M_s) of out-of-plane is larger than that of in-plane as shown in Figure 3(a). This may be due to the fact that M_s of in-plane is not completely saturated under the maximum applied field of 3 Tesla, which has been reported in other publications about $L1_0$ -FePt films [24, 25]. The ZnO barrier layer, Fe free layer, and Pt protective layer were deposited on the Pt/FePt film at room temperature to prepare the $L1_0$ -FePt based sensor. The in-plane and out-of-plane magnetic hysteresis loops of Pt(4)/FePt(15)/ZnO(5)/Fe(5)/Pt(3) multilayers are shown in Figure 3(b). There hardly exists coupling between top Fe free layer and bottom FePt reference layer for arising apparent kinks in it. The magnetization of multilayers reversal process (represented by arrows) can be understood precisely in out-of-plane loop when external magnetic field is applied perpendicular to film plane. The free layer is aligned perpendicular to reference layer when external magnetic field hits zero (point O). When magnetic field reached -7 kOe (or +7 kOe) (point A or B), the bottom FePt would begin to reverse from the up (down) to down (up) perpendicular to the films.

A typical MR curve of a nonpatterned sample is shown in Figure 4, showing regular current-in-plane (CIP) MR effect with an applied magnetic field out of the film plane. The

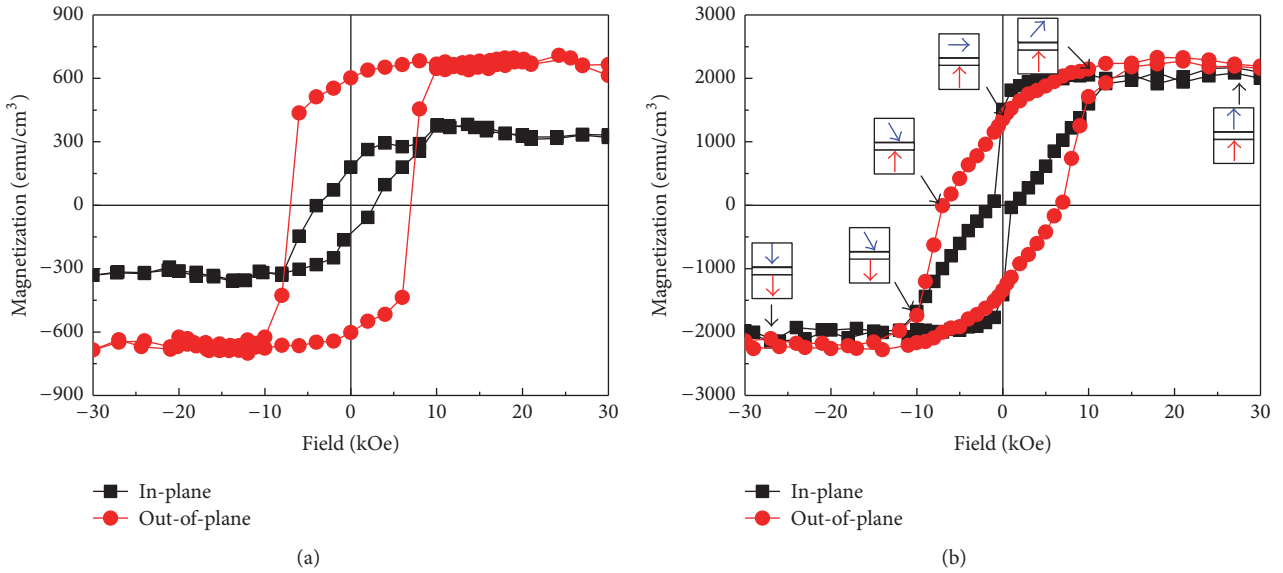


FIGURE 3: In-plane and out-of-plane magnetic hysteresis loops. (a) The Pt(4)/Ll₀-FePt(15) bilayers. (b) The Pt(4)/Ll₀-FePt(15)/ZnO(5)/Fe(5)/Pt(3) multilayers. The arrows show the magnetization reversal process of the Fe free layer (top blue) and FePt reference layer (bottom red) in the out-of-plane loop in (b).

MR values are found to be 0.5% and 1.2% measured at room temperature and 10 K, respectively. A double-peak feature at the coercive fields can be observed in the curves, which is in agreement with the magnetic hysteresis loop in Figure 3. Here, the MR is defined as $MR = [R(H) - R(\max)]/R(\max) \times 100\%$, where $R(H)$ and $R(\max)$ are the resistance at external field H and the maximum resistance, respectively. This value is the typical magnitude of MR in Ll₀-FePt based multilayers [14, 26, 27], because that ZnO cannot be perfectly grown on Ll₀-FePt layer as shown Figure 3(a). Besides, we believe that the MR value of the film may be higher due to the fact that the MR curve is not saturated at 20 kOe, and the MR ratio might obtain a higher value if a higher magnetic field was applied to our sample.

The expected high field linear characteristic and non-hysteretic variation of the MR with highly reversibility is obtained when the magnetic field varies between +5 kOe and -5 kOe at room temperature as shown in Figure 4(c). The sensitivity is 0.2%/T in the MTJ composed of Pt(4)/FePt(15)/ZnO(5)/Fe(5)/Pt(3) multilayers. The magnetic configuration and the resistance evolve with the field as shown in Figure 4(c). When the applied field is +5 kOe, the magnetization direction of the Ll₀-FePt layer points out-of-plane and the one of the Fe layer is not completely parallel to the magnetization of Ll₀-FePt layer (see point A in Figure 4(c)) due to the fact that the magnetic loop and MR are not saturated at 5 kOe shown in Figures 3(b) and 4(a). At this point (point M), the device has a smaller resistance. The value of resistance increases linearly with decreasing magnetic field until the field is reduced to zero at point O, where the magnetization of the Fe layer is rotated to perpendicular to the one of Ll₀-FePt layer. With the magnetic field increases in the reverse

direction, the resistance continues to increase until the magnetic field reaches -5 kOe at point N. It is important to note that the magnetization of Ll₀-FePt layer is always invariant throughout the process, which plays a key role in the MR linear variation with the magnetic field.

4. Conclusion

In summary, linear MR in Pt/FePt/ZnO/Fe/Pt multilayer magnetic sensor was investigated. In this design, perpendicular anisotropy Ll₀-FePt reference layer and in-plane anisotropy Fe free layer separated by ZnO barrier layer are perpendicular to each other. The Ll₀-FePt film with large coercivity and high squareness ratio was obtained by in situ substrate heating. The MR values of 0.5% and 1.2% were obtained at room temperature and 10 K, respectively. Linear MR response is observed in this sensor in a large range between +5 kOe and -5 kOe at room temperature. This Ll₀-FePt based linear MR is significant for high field linear magnetic sensors.

Competing Interests

The authors declare that there is no conflict of interests regarding the publication of this paper.

Acknowledgments

The work is financially supported by the National High Technology Research and Development Program of China (863 Program, no. 2014AA032904), NSFC (nos. 51571136,

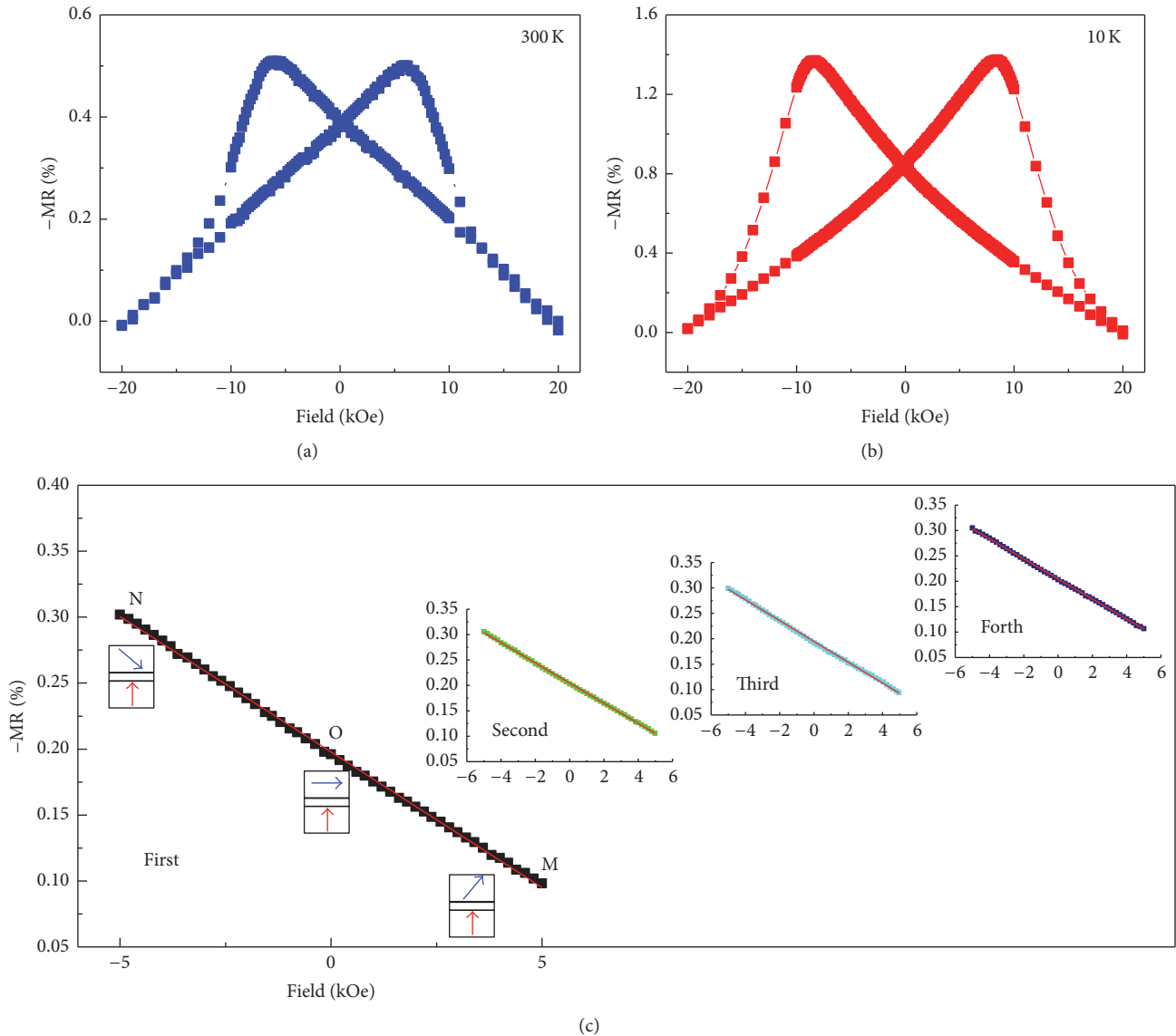


FIGURE 4: The MR of the multilayer films measured at 300 K (a) and 10 K (b); (c) the linear magnetic field response of the multilayer films when the external field varies between +5 kOe and -5 kOe at 300 K. The insets in (c) show the three repeated measures of MR curve of the same sample.

61434002, and 61306109), and Shanxi Scholarship Council of China (2015-069).

References

- [1] I. Žutić, J. Fabian, and S. D. Sarma, "Spintronics: fundamentals and applications," *Reviews of Modern Physics*, vol. 76, no. 2, pp. 323–410, 2004.
- [2] K. Inomata, N. Ikeda, N. Tezuka et al., "Highly spin-polarized materials and devices for spintronics," *Science and Technology of Advanced Materials*, vol. 9, no. 1, Article ID 014101, 19 pages, 2008.
- [3] F. Pan, C. Song, X. J. Liu, Y. C. Yang, and F. Zeng, "Ferromagnetism and possible application in spintronics of transition-metal-doped ZnO films," *Materials Science and Engineering R: Reports*, vol. 62, no. 1, pp. 1–35, 2008.
- [4] D. Boldrin and A. S. Wills, "Anomalous Hall effect in geometrically frustrated magnets," *Advances in Condensed Matter Physics*, vol. 2012, Article ID 615295, 12 pages, 2012.
- [5] H. X. Wei, Q. H. Qin, M. Ma, R. Sharif, and X. F. Han, "80% tunneling magnetoresistance at room temperature for thin Al-O barrier magnetic tunnel junction with CoFeB as free and reference layers," *Journal of Applied Physics*, vol. 101, no. 9, Article ID 09B501, 3 pages, 2007.
- [6] S. S. P. Parkin, C. Kaiser, A. Panchula et al., "Giant tunnelling magnetoresistance at room temperature with MgO (100) tunnel barriers," *Nature Materials*, vol. 3, no. 12, pp. 862–867, 2004.
- [7] T. R. McGuire and R. I. Potter, "Anisotropic magnetoresistance in ferromagnetic 3D alloys," *IEEE Transactions on Magnetics*, vol. 11, no. 4, pp. 1018–1038, 1975.
- [8] X. Liu, C. Ren, and G. Xiao, "Magnetic tunnel junction field sensors with hard-axis bias field," *Journal of Applied Physics*, vol. 92, no. 8, pp. 4722–4725, 2002.

- [9] P. Wiśniowski, J. M. Almeida, S. Cardoso, N. P. Barradas, and P. P. Freitas, "Effect of free layer thickness and shape anisotropy on the transfer curves of MgO magnetic tunnel junctions," *Journal of Applied Physics*, vol. 103, no. 7, Article ID 07A910, 3 pages, 2008.
- [10] J. Y. Chen, J. F. Feng, and J. M. D. Coey, "Tunable linear magnetoresistance in MgO magnetic tunnel junction sensors using two pinned CoFeB electrodes," *Applied Physics Letters*, vol. 100, no. 14, Article ID 142407, 4 pages, 2012.
- [11] H. X. Wei, Q. H. Qin, Z. C. Wen, X. F. Han, and X.-G. Zhang, "Magnetic tunnel junction sensor with Co/Pt perpendicular anisotropy ferromagnetic layer," *Applied Physics Letters*, vol. 94, no. 17, Article ID 172902, 2009.
- [12] S. Ikeda, J. Hayakawa, Y. Ashizawa et al., "Tunnel magnetoresistance of 604% at 300 K by suppression of Ta diffusion in CoFeB/MgO/CoFeB pseudo-spin-valves annealed at high temperature," *Applied Physics Letters*, vol. 93, no. 8, Article ID 082508, 2008.
- [13] S. Yuasa, T. Nagahama, A. Fukushima, Y. Suzuki, and K. Ando, "Giant room-temperature magnetoresistance in single-crystal Fe/MgO/Fe magnetic tunnel junctions," *Nature Materials*, vol. 3, no. 12, pp. 868–871, 2004.
- [14] Q. H. Qin, H. X. Wei, and X. F. Han, "Linear magnetic field response spin valve with perpendicular anisotropy ferromagnet layer," *Journal of Applied Physics*, vol. 103, no. 7, Article ID 07E906, 3 pages, 2008.
- [15] C. Song, Y. Y. Wang, X. J. Li, G. Y. Wang, and F. Pan, "Inter-layer magnetostatic coupling and linear magnetoresistance in [Pd/Co]/MgO/Co junction sensor," *Applied Physics Letters*, vol. 101, no. 6, Article ID 062404, 4 pages, 2012.
- [16] H. Naganuma, G. Kim, Y. Kawada et al., "Electrical detection of millimeter-waves by magnetic tunnel junctions using perpendicular magnetized $L1_0$ -FePd free layer," *Nano Letters*, vol. 15, no. 1, pp. 623–628, 2015.
- [17] M. Yoshikawa, E. Kitagawa, T. Nagase et al., "Tunnel magnetoresistance over 100% in MgO-based magnetic tunnel junction films with perpendicular magnetic $L1_0$ -FePt electrodes," *IEEE Transactions on Magnetics*, vol. 44, no. 11, pp. 2573–2576, 2008.
- [18] T. Shima, K. Takanashi, Y. K. Takahashi, and K. Hono, "Coercivity exceeding 100 kOe in epitaxially grown FePt sputtered films," *Applied Physics Letters*, vol. 85, no. 13, pp. 2571–2573, 2004.
- [19] P. Ho, G. Han, K. He, G. M. Chow, and J. S. Chen, "Ultra-thin $L1_0$ -FePt for perpendicular anisotropy $L1_0$ -FePt/Ag/[Co/Pd]₃₀ pseudo spin valves," *Journal of Applied Physics*, vol. 115, no. 17, Article ID 17C102, 3 pages, 2014.
- [20] B. Laenens, F. M. Almeida, N. Planckaert et al., "Interplay between structural and magnetic properties of $L1_0$ -FePt (001) thin films directly grown on MgO(001)," *Journal of Applied Physics*, vol. 105, no. 7, Article ID 073913, 6 pages, 2009.
- [21] K. F. Dong, H. H. Li, and J. S. Chen, "Lattice mismatch-induced evolution of microstructural properties in FePt films," *Journal of Applied Physics*, vol. 113, no. 23, Article ID 233904, 10 pages, 2013.
- [22] R. F. C. Farrow, D. Weller, R. F. Marks, M. F. Toney, A. Cebollada, and G. R. Harp, "Control of the axis of chemical ordering and magnetic anisotropy in epitaxial FePt films," *Journal of Applied Physics*, vol. 79, no. 8, pp. 5967–5969, 1996.
- [23] J. Kim, C. Rong, Y. Lee, J. P. Liu, and S. Sun, "From core/shell structured FePt/Fe₃O₄/MgO to ferromagnetic FePt nanoparticles," *Chemistry of Materials*, vol. 20, no. 23, pp. 7242–7245, 2008.
- [24] C. Feng, Q. Zhan, B. Li et al., "Magnetic properties and microstructure of FePt/Au multilayers with high perpendicular magnetocrystalline anisotropy," *Applied Physics Letters*, vol. 93, no. 15, Article ID 152513, 2008.
- [25] C. Feng, E. Zhang, C. C. Xu et al., "Magnetic properties and microstructure of $L1_0$ -FePt/AlN perpendicular nanocomposite films," *Journal of Applied Physics*, vol. 110, no. 6, Article ID 063910, 5 pages, 2011.
- [26] P. Ho, G. C. Han, R. F. L. Evans, R. W. Chantrell, G. M. Chow, and J. S. Chen, "Perpendicular anisotropy $L1_0$ -FePt based pseudo spin valve with Ag spacer layer," *Applied Physics Letters*, vol. 98, no. 13, Article ID 132501, 3 pages, 2011.
- [27] S. Van Dijken and J. M. D. Coey, "Magnetoresistance sensor with an out-of-plane magnetized sensing layer," *Applied Physics Letters*, vol. 87, no. 2, Article ID 022504, 3 pages, 2005.

Research Article

Micromagnetic Simulation of Strain-Assisted Current-Induced Magnetization Switching

H. B. Huang, C. P. Zhao, and X. Q. Ma

Department of Physics, University of Science and Technology Beijing, Beijing 100083, China

Correspondence should be addressed to H. B. Huang; houbinghuang@gmail.com

Received 13 June 2016; Revised 30 July 2016; Accepted 2 August 2016

Academic Editor: Jingsheng Chen

Copyright © 2016 H. B. Huang et al. This is an open access article distributed under the Creative Commons Attribution License, which permits unrestricted use, distribution, and reproduction in any medium, provided the original work is properly cited.

We investigated the effect of substrate misfit strain on the current-induced magnetization switching in magnetic tunnel junctions by combining micromagnetic simulation with phase-field microelasticity theory. Our results indicate that the positive substrate misfit strain can decrease the critical current density of magnetization switching by pushing the magnetization from out-of-plane to in-plane directions, while the negative strain pushes the magnetization back to the out-of-plane directions. The magnetic domain evolution is obtained to demonstrate the strain-assisted current-induced magnetization switching.

1. Introduction

Since Sun et al. [1] and Sun et al. [2] proposed the spin transfer torque (STT) effects in the ferromagnetic materials, STT has attracted great attention due to its potential applications of magnetic devices in the past decades [3–8]. In STT effects, angular momentums of the electrons may transfer to the ferromagnetic magnetization. There are three major effects in STT driven magnetization dynamics: (1) current-induced magnetization switching [9–12], (2) current-driven magnetization oscillations [4, 13, 14], and (3) current-driven domain wall motion [15–20]. The current-induced magnetization switching is used in the application of magnetic random access memory (MRAM), which has the advantage of large storage density, high switching speed, low energy consumption, and avoidance of cross writing. The current-induced magnetization switching also eliminates crosstalk between neighboring cells during writing [21]. Furthermore, STT-MRAM has practically unlimited endurance and requires less energy and is faster than conventional magnetic field control MRAM. However, the high critical switching current density J_c of STT-MRAM has to be reduced to achieve the compatibility with the metal-oxide-semiconductor technology.

There are many attempts to reduce J_c for magnetization switching, for example, using CoFeB as the free layer to

reduce the saturation magnetization M_S [22]; using a double spin-filter structure [23] and an antiferromagnetic pinning structure [24] or inserting a Ru spin scattering layer to increase spin scattering [25]; using a composite free layer consisting of two ferromagnetic layers with various coupling types [26–28]; or using Heusler-based spin valve nanopillar [29]. In magnetic thin films, the strain can be effectively utilized to tune the magnetic domain structures [30–33]. For example, the magnetization can be switched between an in-plane and out-of-plane orientation under isotropic biaxial in-plane strains [34, 35] or rotate within the film plane under anisotropic biaxial in-plane strains [36]. Recently, Pertsev and Kohlstedt [37] demonstrated that the critical current density needed for 180° magnetization switching in the free magnetic layer of a spin valve can be reduced drastically by the assistance of substrate misfit strain based on the thermodynamic calculation. Thermodynamic calculation minimizes the total free energy to obtain homogeneous magnetization distribution, but micromagnetic simulations provide the microstructure evolution of magnetization switching. The conventional micromagnetic simulations do not take account of such elastic effect and thus cannot be employed to investigate the assistance of substrate misfit strain in STT induced magnetization switching.

In this paper, we combined the phase-field microelasticity theory with micromagnetic simulations to illustrate misfit

strain which causes the decrease of the critical current density for magnetization switching. In particular, we investigated STT induced 180° magnetization switching in CoFeB magnetic tunnel junctions based on the misfit strain induced 90° magnetization switching [38]. Firstly, we discussed our results by using a hysteresis loop to show the decrease of critical current density. Then, we discussed the effect of substrate strain assistance in STT induced magnetization switching by showing magnetization and magnetic domain evolutions.

2. Model Description

As shown in Figure 1, we investigate the spin valve nanopillars with the structure of CoFeB (2 nm)/MgO (2 nm)/CoFeB (16 nm) of square cross-sectional area ($80 \times 80 \text{ nm}^2$). A Cartesian coordinate system is employed and the current is along the z -axis. A thin MgO layer separates the two CoFeB layers, and the bottom CoFeB layer is the free layer. A spin-polarized current drives the magnetization dynamics of free layer. The top CoFeB layer is the fixed layer with its magnetization vector \mathbf{P} along the positive z -axis. The initial magnetization vector \mathbf{M} of the layer is along the negative or positive z -axis. The lateral length of the free layer of spin valve is fully constrained by a stiff substrate. We generally define the substrate strain ε_{ii} ($i = 1, 2$). The positive current is defined as electrons flowing from the fixed layer to the free layer. In the bottom, a ferroelectric (FE) layer is used to adjust the output strain. In this paper, the positive current will lead to the parallel structure (P, “1”) while the negative current will lead to the antiparallel structure (AP, “0”) according to STT theory.

We use a generalized Landau-Lifshitz-Gilbert-Slonczewski (LLGS) equation to describe the magnetization dynamics [39, 40],

$$\begin{aligned} \frac{d\mathbf{M}}{dt} = & -\gamma' \mathbf{M} \times \mathbf{H}_{\text{eff}} - \frac{\alpha\gamma'}{M_s} \mathbf{M} \times (\mathbf{M} \times \mathbf{H}_{\text{eff}}) \\ & - \frac{2\mu_B J}{(1 + \alpha^2) e d M_s^3} g(\mathbf{M}, \mathbf{P}) \mathbf{M} \times (\mathbf{M} \times \mathbf{P}) \quad (1) \\ & + \frac{2\mu_B \alpha J}{(1 + \alpha^2) e d M_s^2} g(\mathbf{M}, \mathbf{P}) (\mathbf{M} \times \mathbf{P}), \end{aligned}$$

where the first term represents the precession torque and the second term represents the Gilbert damping torque. \mathbf{H}_{eff} is the effective field, $\gamma' = \gamma/(1 + \alpha^2)$, γ is the electron gyromagnetic ratio, and α is the dimensionless damping parameter. The effective field includes the anisotropy field, the demagnetization field, the external field, the elastic field, and the exchange field; namely, $\mathbf{H}_{\text{eff}} = \mathbf{H}_k + \mathbf{H}_d + \mathbf{H}_{\text{ext}} + \mathbf{H}_{\text{elas}} + \mathbf{H}_{\text{ex}}$, given as

$$\mathbf{H}_{\text{eff}} = -\frac{1}{\mu_0} \frac{\delta E}{\delta \mathbf{M}}, \quad (2)$$

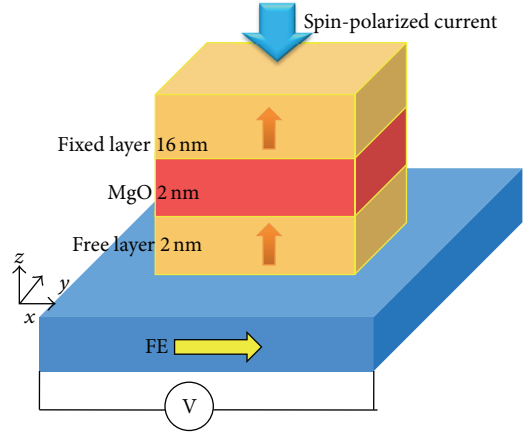


FIGURE 1: Schematic structure of CoFeB (2 nm)/MgO (2 nm)/CoFeB (16 nm) magnetic tunnel junction spin valve.

where E is the total energy, expressed by $E = E_k + E_d + E_{\text{ext}} + E_{\text{elas}} + E_{\text{ex}}$, where E_k , E_d , E_{ext} , E_{elas} , and E_{ex} are anisotropy energy (including magnetocrystalline and shape anisotropies) [41], demagnetization energy, Zeeman energy, elastic energy, and exchange energy, respectively. The details for obtaining E_k , E_d , E_{ext} , E_{elas} , and E_{ex} can be found in our previous papers [41–43]. The last two terms on the right side of (1) describe STT that tends to drag the magnetization away from its initial state to its final state. The scalar function is given by [39, 40], $g(\mathbf{M}, \mathbf{P}) = [-4 + (1 + \eta)^3 (3 + \mathbf{M} \cdot \mathbf{P}/M_s^2)/4\eta^{3/2}]^{-1}$, where η is the spin polarization constant, \mathbf{M} and \mathbf{P} are the magnetization of free and fixed layers in Figure 1, and the angle between \mathbf{M} and \mathbf{P} is θ . $\mathbf{M} \cdot \mathbf{P}/M_s^2 = \cos\theta$. \mathbf{H}_{STT} is the corresponding effective field given by $\mathbf{H}_{\text{STT}} = 2\mu_B J g(\mathbf{M}, \mathbf{P}) \mathbf{M} \times \mathbf{P}/(\gamma e d M_s^3)$, where μ_B , J , d , e , and M_s are the Bohr magneton, current density, thickness of the free layer, electron charge, and saturation magnetization, respectively.

The magnetic parameters employed in the simulations are as follows: saturation magnetization $M_s = 9.549 \times 10^5 \text{ A/m}$ [44, 45], Gilbert damping parameter $\alpha = 0.00439$ [46], spin polarization factor $\eta = 0.5$ [47], magnetic anisotropy constants $K_1 = 1.2 \times 10^4 \text{ J/m}^3$ and $K_2 = 0$ [37], elastic constants $c_{11} = 2.57 \times 10^{11} \text{ Nm}^{-2}$, $c_{12} = 1.62 \times 10^{11} \text{ Nm}^{-2}$, and $c_{44} = 1.05 \times 10^{11} \text{ Nm}^{-2}$ [37], and magnetostrictive constants $\lambda_{100} = 139 \text{ ppm}$ and $\lambda_{111} = 22 \text{ ppm}$ [44, 45]. We investigated the influence of normal substrate strains ε_{11} and ε_{22} on the magnetization state by assuming a zero shear strain. The dynamics of magnetization was investigated by numerically solving the time-dependent LLGS equation using the Gauss-Seidel projection method and the semi-implicit Fourier spectral method [48–53]. The samples were discretized in computational cells of $2 \times 2 \times 2 \text{ nm}^3$.

3. Results and Discussions

Figure 2 shows the hysteresis loops with the substrate misfit strains ($\varepsilon_{11} = \varepsilon_{22} = 0$ and 0.5%). Without the applied

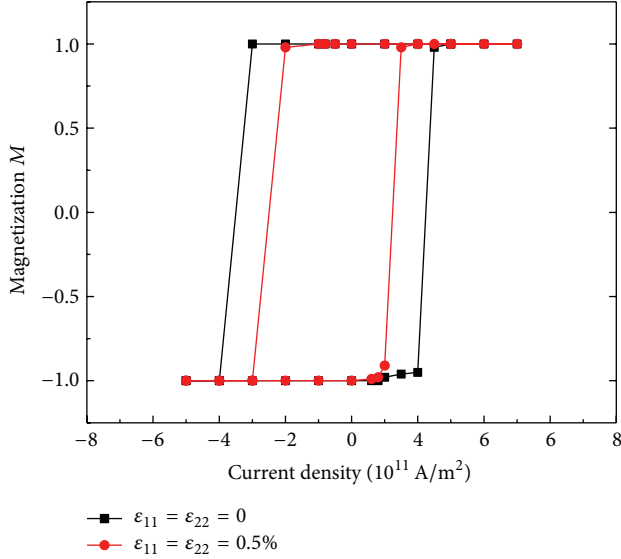


FIGURE 2: Hysteresis loops of magnetization versus current density with strain and without strain.

strain, there is a square hysteresis loop of magnetization versus current density (M - J) curve. The critical current densities are 2.1×10^{11} A/m² from AP to P and -3.7×10^{11} A/m² from P to AP. At the biaxial strain 0.5%, we observe the decrease of critical current densities for magnetization switching (red hysteresis loop). The critical current densities are 1.3×10^{11} A/m² from AP to P and -2.7×10^{11} A/m² from P to AP. The positive substrate misfit strain reduces the critical current densities by pushing the magnetization from the out-of-plane to the in-plane directions. Therefore, the substrate misfit strain can be used effectively in assisting the STT induced magnetization switching.

Figure 3 shows the evolution of magnetization components $\langle m_z \rangle$ with different current densities and substrate misfit strains. For the black line, the magnetization is along the initial $-z$ -axis and keeps the AP structure without the applied current and strain. The red and pink lines represent the magnetization switching from AP to P and P to AP at the current densities of 1.0×10^{12} A/m² and -1.0×10^{12} A/m². Since the applied current densities are large enough to overcome the barrier, the magnetization will switch from AP to P or P to AP at the negative or positive current densities. We take the magnetization switching from AP to P, for example, to show the effect of misfit strain. If the biaxial positive strain $\varepsilon_{11} = \varepsilon_{22} = 0.5\%$ is applied, the magnetization switching (cyan line) is faster than that without strain (red line). However, the biaxial negative strain $\varepsilon_{11} = \varepsilon_{22} = -0.5\%$ will prolong the time of the magnetization switching (blue line). The mechanism of the phenomenon resulted from the fact that the positive strain will drag the magnetization along the in-plane direction, while the negative strain will push the magnetization back to the out-of-plane direction.

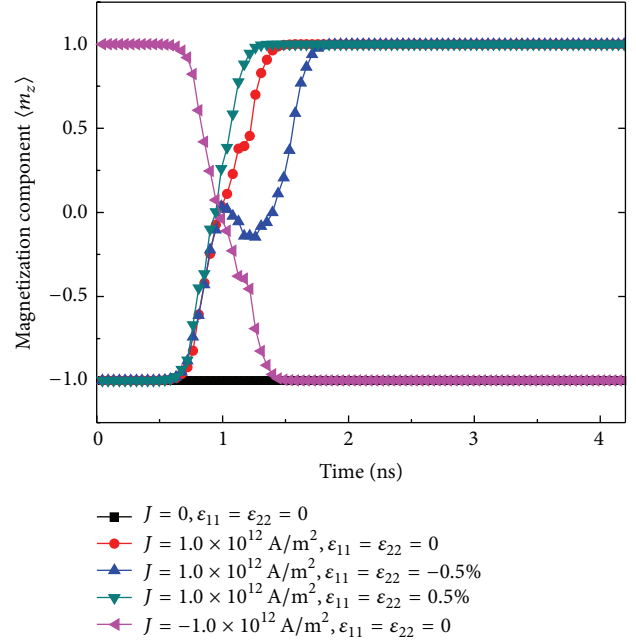


FIGURE 3: Time evolution of magnetization components $\langle m_z \rangle$ with different current densities and substrate misfit strains.

We can use the magnetic domain evolution to elucidate the effect of misfit strain. As shown in Figure 4, we show the corresponding magnetization distributions at the current density 1.0×10^{12} A/m² under different applied strains. Three rows correspond to the magnetization switching of red (zero strain), cyan (0.5%), and blue (-0.5%) lines in Figure 3. The colors represent different domain area: purple is $-z$, red is $+z$, and other colors are domain wall area. We observed that the magnetization was switched from the initial $-z$ -axis to the final $+z$ -axis due to the large current density input. This multidomain evolution process resulted from the large current input energy. In the first row, the initial magnetization was along $-z$ -axis. Without the strain, the magnetization switching process started from the outer to the inner of the free layer. However, the magnetization switching process started from the inner to the outer of the free layer in the negative strain. For the positive strain, we can observe that the nucleation starts from the center and diffuses to the edges.

4. Conclusions

In conclusion, we investigated the strain-assisted STT induced magnetization switching in CoFeB-based magnetic tunnel junctions by combining phase-field method with micromagnetic simulations. We proposed an effective method of using strain-assisted STT induced magnetization switching instead of using an external magnetic field. Since the tensile biaxial substrate misfit strains drag the magnetization into the in-plane directions, the critical current density and switching time are decreased significantly.

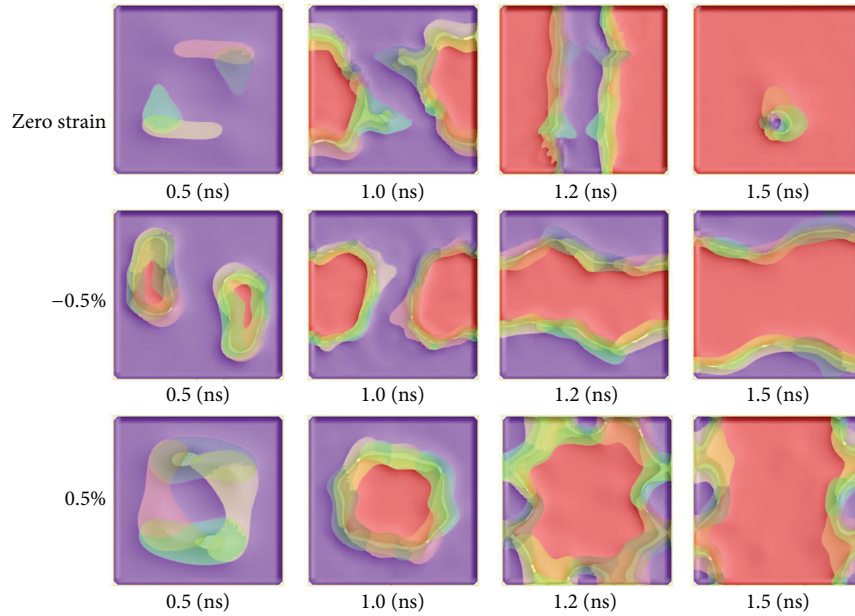


FIGURE 4: Magnetic domain evolutions with different misfit substrate strains during the magnetization switching.

Competing Interests

The authors declare that there are no competing interests regarding the publication of this paper.

Acknowledgments

This work was sponsored by the National Science Foundation of China (11504020).

References

- [1] J. Z. Sun, J. DeBrosse, and P. K. Wang, "Feasibility of an active-read approach for spin-torque switched magnetic tunnel junctions in a random access memory," *Journal of Applied Physics*, vol. 114, no. 9, Article ID 094503, 2013.
- [2] G. Y. Sun, E. Kursun, J. A. Rivers, and Y. Xie, "Exploring the vulnerability of CMPs to soft errors with 3D stacked nonvolatile memory," *ACM Journal on Emerging Technologies in Computing Systems*, vol. 9, no. 3, article 22, 2013.
- [3] J. A. Katine, F. J. Albert, R. A. Buhrman, E. B. Myers, and D. C. Ralph, "Current-driven magnetization reversal and spin-wave excitations in Co/Cu/Co pillars," *Physical Review Letters*, vol. 84, no. 14, pp. 3149–3152, 2000.
- [4] S. Kaka, M. R. Pufall, W. H. Rippard, T. J. Silva, S. E. Russek, and J. A. Katine, "Mutual phase-locking of microwave spin torque nano-oscillators," *Nature*, vol. 437, no. 7057, pp. 389–392, 2005.
- [5] S. I. Klisev, J. C. Sankey, I. N. Krivorotov et al., "Microwave oscillations of a nanomagnet driven by a spin-polarized current," *Nature*, vol. 425, no. 6956, pp. 380–383, 2003.
- [6] I. Lee, Y. Obukhov, G. Xiang et al., "Nanoscale scanning probe ferromagnetic resonance imaging using localized modes," *Nature*, vol. 466, no. 7308, pp. 845–848, 2010.
- [7] M. Tsoi, A. G. M. Jansen, J. Bass, W.-C. Chlang, V. Tsoi, and P. Wyder, "Generation and detection of phase-coherent current-driven magnons in magnetic multilayers," *Nature*, vol. 406, no. 6791, pp. 46–48, 2000.
- [8] D. Ralph and M. Stiles, "Spin transfer torques," *Journal of Magnetism and Magnetic Materials*, vol. 320, no. 7, pp. 1190–1216, 2008.
- [9] E. B. Myers, D. C. Ralph, J. A. Katine, R. N. Louie, and R. A. Buhrman, "Current-induced switching of domains in magnetic multilayer devices," *Science*, vol. 285, no. 5429, pp. 867–870, 1999.
- [10] J. Grollier, P. Boulenc, V. Cros et al., "Switching a spin valve back and forth by current-induced domain wall motion," *Applied Physics Letters*, vol. 83, no. 3, pp. 509–511, 2003.
- [11] Y. Liu, Z. Zhang, P. P. Freitas, and J. L. Martins, "Current-induced magnetization switching in magnetic tunnel junctions," *Applied Physics Letters*, vol. 82, no. 17, pp. 2871–2873, 2003.
- [12] B. Özyilmaz, A. D. Kent, D. Monsma, J. Z. Sun, M. J. Rooks, and R. H. Koch, "Current-induced magnetization reversal in high magnetic fields in Co/Cu/Co nanopillars," *Physical Review Letters*, vol. 91, no. 6, Article ID 067203, 2003.
- [13] D. V. Berkov, "Micromagnetic simulations of the magnetization dynamics in nanostructures with special applications to spin injection," *Journal of Magnetism and Magnetic Materials*, vol. 300, no. 1, pp. 159–163, 2006.
- [14] V. S. Pribiag, I. N. Krivorotov, G. D. Fuchs et al., "Magnetic vortex oscillator driven by d.c. spin-polarized current," *Nature Physics*, vol. 3, no. 7, pp. 498–503, 2007.
- [15] Z. Li and S. Zhang, "Domain-wall dynamics driven by adiabatic spin-transfer torques," *Physical Review B*, vol. 70, no. 2, Article ID 024417, 10 pages, 2004.
- [16] G. Meier, M. Bolte, U. Merkt, B. Krüger, and D. Pfannkuche, "Current-induced domain-wall motion in permalloy semi rings," *Journal of Magnetism and Magnetic Materials*, vol. 316, no. 2, pp. e966–e968, 2007.
- [17] C. Nam, Y. M. Jang, K. S. Lee, S. K. Lee, T. W. Kim, and B. K. Cho, "Current-supported domain wall movement to the target spot with a magnetic field," *Journal of Magnetism and Magnetic Materials*, vol. 310, no. 2, pp. 2023–2025, 2007.

- [18] M. D. Stiles, W. M. Saslow, M. J. Donahue, and A. Zangwill, "Adiabatic domain wall motion and Landau-Lifshitz damping," *Physical Review B*, vol. 75, no. 21, Article ID 214423, 2007.
- [19] G. S. D. Beach, M. Tsoi, and J. L. Erskine, "Current-induced domain wall motion," *Journal of Magnetism and Magnetic Materials*, vol. 320, no. 7, pp. 1272–1281, 2008.
- [20] R. A. Duine, "Spin pumping by a field-driven domain wall," *Physical Review B*, vol. 77, no. 1, Article ID 014409, 2008.
- [21] K. MacHida, N. Funabashi, K.-I. Aoshima et al., "Spin transfer switching of closely arranged multiple pillars with current-perpendicular-to-plane spin valves," *Journal of Applied Physics*, vol. 103, no. 7, Article ID 07A713, 2008.
- [22] K. Yagami, A. A. Tulapurkar, A. Fukushima, and Y. Suzuki, "Low-current spin-transfer switching and its thermal durability in a low-saturation-magnetization nanomagnet," *Applied Physics Letters*, vol. 85, no. 23, pp. 5634–5636, 2004.
- [23] G. D. Fuchs, J. A. Katine, S. I. Kiselev et al., "Spin torque, tunnel-current spin polarization, and magnetoresistance in MgO magnetic tunnel junctions," *Physical Review Letters*, vol. 96, no. 18, Article ID 186603, 2006.
- [24] K. J. Lee, T. H. Y. Nguyen, and K.-H. Shin, "Reduction in critical current density of current-induced magnetization switching," *Journal of Magnetism and Magnetic Materials*, vol. 304, no. 1, pp. 102–105, 2006.
- [25] Y. Jiang, G. H. Yu, Y. B. Wang et al., "Spin transfer in antisymmetric exchange-biased spin-valves," *Applied Physics Letters*, vol. 86, no. 19, Article ID 192515, pp. 1–3, 2005.
- [26] H. Meng, J. Wang, and J.-P. Wang, "Low critical current for spin transfer in magnetic tunnel junctions," *Applied Physics Letters*, vol. 88, no. 8, Article ID 082504, 2006.
- [27] Z. Zhang, Y. Zhang, Y. Liu, B. Ma, and Q. Y. Jin, "Spin-transfer-induced magnetization switching in tunnel junctions with nanocurrent channels," *Applied Physics Letters*, vol. 90, no. 11, Article ID 112504, 2007.
- [28] C.-T. Yen, W.-C. Chen, D.-Y. Wang et al., "Reduction in critical current density for spin torque transfer switching with composite free layer," *Applied Physics Letters*, vol. 93, no. 9, Article ID 092504, 2008.
- [29] K. Aoshima, N. Funabashi, K. Machida, Y. Miyamoto, K. Kuga, and N. Kawamura, "Current induced magnetization reversal in spin valves with Heusler alloys," *Journal of Magnetism and Magnetic Materials*, vol. 310, no. 2, pp. 2018–2019, 2007.
- [30] M. T. Johnson, P. J. H. Bloemen, F. J. A. Den Broeder, and J. J. De Vries, "Magnetic anisotropy in metallic multilayers," *Reports on Progress in Physics*, vol. 59, no. 11, pp. 1409–1458, 1996.
- [31] D. Sander, "The correlation between mechanical stress and magnetic anisotropy in ultrathin films," *Reports on Progress in Physics*, vol. 62, no. 5, pp. 809–858, 1999.
- [32] K. H. Ahn, T. Lookman, and A. R. Bishop, "Strain-induced metal-insulator phase coexistence in perovskite manganites," *Nature*, vol. 428, no. 6981, pp. 401–404, 2004.
- [33] A. Mukherjee, W. S. Cole, P. Woodward, M. Randeria, and N. Trivedi, "Theory of strain-controlled magnetotransport and stabilization of the ferromagnetic insulating phase in manganite thin films," *Physical Review Letters*, vol. 110, no. 15, Article ID 157201, 2013.
- [34] N. A. Pertsev, "Giant magnetoelectric effect via strain-induced spin reorientation transitions in ferromagnetic films," *Physical Review B*, vol. 78, no. 21, Article ID 212102, 2008.
- [35] J. Wang, J.-M. Hu, L.-Q. Chen, and C.-W. Nan, "Strain-domain structure and stability diagrams for single-domain magnetic thin films," *Applied Physics Letters*, vol. 103, Article ID 142413, 2013.
- [36] J.-M. Hu and C. W. Nan, "Electric-field-induced magnetic easy-axis reorientation in ferromagnetic/ferroelectric layered heterostructures," *Physical Review B*, vol. 80, no. 22, Article ID 224416, 2009.
- [37] N. A. Pertsev and H. Kohlstedt, "Magnetoresistive memory with ultralow critical current for magnetization switching," *Advanced Functional Materials*, vol. 22, no. 22, pp. 4696–4703, 2012.
- [38] J.-M. Hu, G. Sheng, J. X. Zhang, C. W. Nan, and L. Q. Chen, "Phase-field simulation of strain-induced domain switching in magnetic thin films," *Applied Physics Letters*, vol. 98, no. 11, Article ID 112505, 2011.
- [39] L. Berger, "Emission of spin waves by a magnetic multilayer traversed by a current," *Physical Review B*, vol. 54, no. 13, pp. 9353–9358, 1996.
- [40] J. C. Slonczewski, "Current-driven excitation of magnetic multilayers," *Journal of Magnetism and Magnetic Materials*, vol. 159, no. 1-2, pp. L1–L7, 1996.
- [41] J.-M. Hu, Z. Li, J. Wang, and C. W. Nan, "Electric-field control of strain-mediated magnetoelectric random access memory," *Journal of Applied Physics*, vol. 107, no. 9, Article ID 093912, 2010.
- [42] H. B. Huang, J. M. Hu, T. N. Yang, X. Q. Ma, and L. Q. Chen, "Strain-assisted current-induced magnetization reversal in magnetic tunnel junctions: a micromagnetic study with phase-field microelasticity," *Applied Physics Letters*, vol. 105, no. 12, Article ID 122407, 2014.
- [43] K. M. D. Hals and A. Brataas, "Phenomenology of current-induced spin-orbit torques," *Physical Review B*, vol. 88, no. 8, Article ID 085423, 2013.
- [44] S. Ikeda, K. Miura, H. Yamamoto et al., "A perpendicular-anisotropy CoFeB–MgO magnetic tunnel junction," *Nature Materials*, vol. 9, no. 9, pp. 721–724, 2010.
- [45] S. Yan, Z. L. Sun, and Y. B. Bazaliy, "Modification of the Stoner-Wohlfarth astroid by a spin-polarized current: an exact solution," *Physical Review B*, vol. 88, no. 5, Article ID 054408, 2013.
- [46] C. A. F. Vaz, J. A. C. Bland, and G. Lauhoff, "Magnetism in ultrathin film structures," *Reports on Progress in Physics*, vol. 71, no. 5, Article ID 056501, 2008.
- [47] J. P. Cascales, D. Herranz, J. L. Sambricio, U. Ebels, J. A. Katine, and F. G. Aliev, "Magnetization reversal in sub-100 nm magnetic tunnel junctions with ultrathin MgO barrier biased along the hard axis," *Applied Physics Letters*, vol. 102, no. 9, Article ID 092404, 2013.
- [48] Y. Kajiwara, K. Uchida, D. Kikuchi, T. An, Y. Fujikawa, and E. Saitoh, "Spin-relaxation modulation and spin-pumping control by transverse spin-wave spin current in $Y_3Fe_5O_{12}$," *Applied Physics Letters*, vol. 103, no. 5, Article ID 052404, 2013.
- [49] H. B. Huang, X. Q. Ma, Z. H. Liu, C. P. Zhao, and L. Q. Chen, "Modelling current-induced magnetization switching in Heusler alloy Co 2FeAl-based spin-valve nanopillar," *Journal of Applied Physics*, vol. 115, no. 13, Article ID 133905, 2014.
- [50] H. B. Huang, X. Q. Ma, Z. H. Liu, C. P. Zhao, S. Q. Shi, and L. Q. Chen, "Simulation of multilevel cell spin transfer switching in a full-Heusler alloy spin-valve nanopillar," *Applied Physics Letters*, vol. 102, no. 4, Article ID 042405, 2013.
- [51] H. B. Huang, X. Q. Ma, Z. H. Liu, and L. Q. Chen, "Modelling high-power spin-torque oscillator with perpendicular magnetization in half-metallic Heusler alloy spin valve nanopillar," *Journal of Alloys and Compounds*, vol. 597, pp. 230–235, 2014.

- [52] H. B. Huang, X. Q. Ma, Z. H. Liu et al., "Micromagnetic simulation of spin-transfer switching in a full-Heusler $\text{Co}_2\text{FeAl}_{0.5}\text{Si}_{0.5}$ alloy spin-valve nanopillar," *Journal of Applied Physics*, vol. 110, no. 3, Article ID 033913, 2011.
- [53] H. B. Huang, X. Q. Ma, C. P. Zhao, Z. H. Liu, and L. Q. Chen, "Micromagnetic study of high-power spin-torque oscillator with perpendicular magnetization in half-metallic Heusler alloy spin valve nanopillar under external magnetic fields," *Journal of Magnetism and Magnetic Materials*, vol. 373, pp. 10–15, 2015.